Minimizing High Spatial Frequency Residual in Active Space Telescope Mirrors

by

Thomas Gray

Submitted to the Department of Aeronautics and Astronautics
in partial fulfillment of the requirements for the degree of

Master of Science in Aeronautics and Astronautics

at the

MASSACHUSETTS INSTITUTE OF TECHNOLOGY

June 2008

Author ....
Department of Aeronautics and Astronautics
June 6, 2008

Certified by ....
David W. Miller
Professor
Thesis Supervisor

Accepted by ....
Prof. David L. Darmofal
Associate Department Head
Chairman, Committee on Graduate Students

Minimizing High Spatial Frequency Residual in Active Space Telescope Mirrors

by

Thomas Gray

Submitted to the Department of Aeronautics and Astronautics
on June 6, 2008, in partial fulfillment of the
requirements for the degree of
Master of Science in Aeronautics and Astronautics

Abstract

The trend in future space telescopes is towards large apertures and lightweight, rib-stiffened, and actively controlled deformable mirrors. These mirror architectures permit the development of segmented and deployed primary mirrors that lead to tremendous advancement in space telescope performance.

Rib-stiffened and discretely actuated deformable mirrors have been shown to effectively mitigate common low order disturbances, but they are inevitably plagued by the "correction limit," or the extent to which the actuators can correct for a given shape disturbance. Improving the correctability of deformable mirrors requires understanding the origins of the correction limit, and optimizing the mirror design accordingly. This thesis details efforts to evaluate the mirror correction limit and the three predominant high spatial frequency mirror surface residual components: actuation-induced dimpling, manufacturing-induced print-through, and disturbance-induced uncorrectable error. The methods for simulating each effect are discussed, and an objective function is developed to quantify the effects of these residual components to gage the performance of each mirror design.

A gradient descent algorithm is combined with the parametric capability of the Modular Optical Space Telescope (MOST) modeling tool to allow rapid trade space navigation and optimization of the mirror design across variations in mirror areal density, f-number, structural mass fractions, and rib aspect ratio. These optimization routines yield more advanced design heuristics that improve upon the simplified design techniques that are typical in industry. By forming the heuristics in terms of minimum machinable rib thickness, these new design relationships produce mirrors that satisfy manufacturing constraints and minimize uncorrectable high spatial frequency error.

Thesis Supervisor: David W. Miller
Title: Professor

Acknowledgments

Thank you to the Department of Defense for supporting this work, and to Dave Pearson and Mark Smith at Xinetics for the helpful collaboration.

To the MOST team members, past and present, who laid the groundwork for MOST and made this research possible: Scott Uebelhart, Deborah Howell, Elizabeth Jordan, Andrzej Stewart, Lucy Cohan, and Joe Bogosian.

To my advisor, Dave Miller, for your patience, guidance, and support. Thank you also to the SSL students and staff for all your help and camaraderie.

Finally, thank you to my family, friends, and to Melissa for your love and support over the years.

> "The soul without imagination is what an observatory would be without a telescope." - Henry Ward Beecher

Contents

List of Figures

List of Tables

Acronyms and Nomenclature

Acronyms

AO active optics

AR aspect ratio (of the primary ribs)

CTE coefficient of thermal expansion

DM deformable mirror

DOF degrees of freedom

FEM finite element model

FFT fast Fourier transform

FS facesheet (mass fraction)

FSM fast-steering mirror

GCR Generalized Conjugate Residual

HST Hubble Space Telescope

IF influence function

JWST James Webb Space Telescope

LOS line-of-site (jitter)

MOST Modular Optical Space Telescope

OTA optical telescope assembly

PMN lead magnesium niobate (electro-strictive actuator material)

P-V peak-to-valley

PZT lead zirconium titanate (piezo-electric actuator material)

RMS root-mean-square

RoC radius of curvature

RSS root-sum-square

RWA reaction wheel assembly

SiC silicon carbide

WFE wavefront error

Nomenclature

$\mathbf{D}$ segment diameter (flat-flat)

$\mathbf{D}_v$ segment diameter (vertex-vertex)

$\mathbf{D}_a$ primary mirror (aperture) diameter (flat-flat)

f primary mirror focal length

$\bar{x}, \bar{y}$ mirror surface nodes cartesian coordinate sets

$\bar{\rho}, \bar{\theta}$ mirror surface nodes polar coordinate sets

$\bar{z}$ set of mirror surface node displacements

$\bar{\zeta}$ set of mirror surface node displacement Zernike coefficients

$A_{r,\theta}$ Zernike polynomial mapping matrix

Σ, Σ_z nodal and Zernike influence function matrices

$\bar{u}$ set of actuator commands

$\bar{r}$ set of shape control mirror surface nodes residuals

$\bar{f}$ set of mirror surface node displacements for a pure focus deformation

$\bar{F}$ generic cost function

$\bar{\chi}$ generic state vector

κ conic constant for mirror prescription

α thermal expansion coefficient

ρ material mass density

P polishing pressure

ΔT uniform (bulk) temperature change relative to ambient temperature

N_t number of finite elements along each rib cell edge

N_{nodes} number of facesheet surface nodes in the finite element mirror model

N_{rings} number of concentric hexagonal rib rings in the mirror backstructure

N_{act} number of embedded shape control actuators

N_{ele} minimum number of required finite elements across mirror segment diameter for cathedral rib implementation

t_{rib} primary rib thickness

t_f facesheet thickness

Chapter 1

Introduction

The trend for future space telescopes is toward larger apertures which will enable higher resolution imaging for both astronomical and ground surveillance applications. This trend drives two key changes in the design of space telescopes. The first is a change toward lower areal densities of the primary mirror. If the areal density of the Hubble Space Telescope (HST) primary mirror is used (180 kg/m^2 [1]), larger apertures simply become prohibitively massive and costly. Technologies that enable high optical performance with low areal density mirrors are thus necessary for the development of larger space apertures.

The second effect of this trend is a transition from the traditional monolithic primary mirror design to a segmented aperture. This thesis focuses on fully populated segmented mirror applications, although the class of segmented aperture space telescopes also includes sparse apertures, such as formation flown, tethered, or structurally connected interferometers. An example of such a segmented mirror, the James Webb Space Telescope (JWST), is shown in Figure 1-1. JWST is NASA's planned successor to HST. The segmentation of its primary mirror will allow JWST to unfold after launch to obtain a primary mirror diameter of 6.5m, compared to the 2.4m diameter of its monolithic predecessor [1].

The need for segmentation of these primary mirrors is attributable to the size limitations of today's launch vehicle fairings. The size of a monolithic primary mirror is constrained by the diameter of the largest launch vehicle fairings. Mirrors that unfold after launch, or that are assembled on orbit, allow for space telescope apertures larger in diameter than the launch vehicles themselves. Such post-launch maneuvers, however, require segmented mirror technology. Control strategies that phase these segments and allow them to function

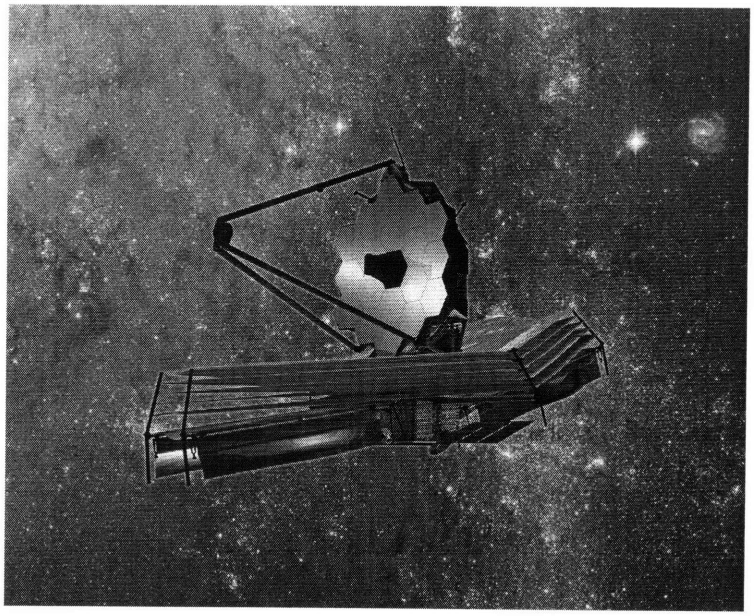

Figure 1-1: Rendition of the James Webb Space Telescope (NASA images)

as a single unit to meet performance requirements are therefore necessary for this second key change in space telescope technology.

These two key trends in space telescope mirror design require both higher performance mirror structures and associated control strategies. This thesis first summarizes the details of mirror shape control for quasi-static disturbances, such as athermalization techniques, and then discusses the strategy for optimizing the geometry of a rib-stiffened hexagonal mirror segment in terms of a comprehensive objective function for minimizing high spatial frequency residual error. The optimization exercise is conducted via a parametric space telescope finite element modeling tool, the Modular Optical Space Telescope (MOST), that enables rapid assessment of the mirror design trade space. Performance metrics quantifying the uncorrectable actuation-induced error and manufacturing-induced print-through are defined, and the results of the trade space optimization are presented relative to these performance metrics.

1.1 Motivation

The trend toward larger, lighter, and actively controlled space telescope mirrors places demands on the structural design of these mirrors and the strategies that control them. For a given set of mirror structural parameters, such as diameter, areal density, and f-number (ratio of focal length to diameter), the structural design of an actively controlled mirror segment must target three simultaneous objectives:

1. Mitigate the adverse effects of quasi-static and dynamic on-orbit disturbances on the mirror figure (i.e. thermal and vibrational disturbances)
2. Avoid manufacturing-induced high spatial frequency errors (i.e. print-through)
3. Allow for the most effective use of the mirror shape control system via actuator-structure coupling (defined later in this section)

These objectives, in some cases, are in conflict. Optimizing the mirror's structure for one objective may lead to a suboptimal design in regards to the other objective. The demands of the manufacturing process, for instance, lead toward a thick mirror facesheet to avoid print-through effects whereas the demands on the control system lead toward a more flexible and controllable facesheet. This thesis considers the latter two design objectives: optimizing the mirror structure to make the best use of the control system's actuators while avoiding manufacturing-induced errors.

The "most effective use" of the actuators can be defined in a number of ways. In terms of actuator stroke, for instance, one would be concerned with maximizing the control authority of the embedded actuators for any given input. The "stroke" of an actuator, defined as the peak-to-valley (P-V) surface normal displacements for a maximum voltage input, would be the driving metric in this case. A mirror design that maximizes actuator stroke is thus capable of mitigating the maximum *amplitude* disturbances. Such a flexible mirror design provides high actuation authority, but it increases the susceptibility of the mirror to actuation-induced and disturbance-induced errors.

A more prudent approach for maximizing actuator effectiveness is to optimize the control system with regards to actuation-induced error. The nature of the actuator layout on any discretely controlled structure gives way to actuator-induced residual, or undesirable short spatial wavelength error that appears when a long spatial wavelength shape is commanded (defined more clearly in Section 4.1.1). This approach focuses on avoiding this induced error so that the net actuation of the actuators commanded in concert produces the most desirable mirror figure.

This thesis focuses on the latter approach of optimizing in terms of actuation-induced error. The problem is to identify the combination of mirror structural properties that allows for the most effective, balanced use of the system's actuators when inducing a global shape command and for avoiding manufacturing related high spatial frequency errors. The parametric structural design capability of the MOST project (see Section 1.3) enables the exploration of a vast continuum of design parameters. The continuous mirror design trade spaces explored in this thesis cover a comprehensive set of designs and show how industry point designs can be improved.

1.2 Approach

The objective of this thesis is to identify the combination of deformable mirror structural parameters that minimize the combination of actuation-induced and manufacturing-induced surface errors on a rib-stiffened, hexagonal, powered mirror segment. The following enumerated approach will be taken in Chapters 3 - 5 toward this goal:

1. Define the nominal mirror test specimen by its structural parameters and the associated control system (Chapter 3)
2. Identify the mirror structural design trade space and cost function (Chapter 4)
3. Identify an appropriate trade space exploration technique to most efficiently and reliably find the global design optimum (Chapter 5)
4. Implement univariate searches to help narrow the trade space focus and to study select supplementary trades (Chapter 5)
5. Compute a full-factorial search over selected design variables to shed light on key trade space behavior (Appendix A)

The following section provides an overview of the MOST model to better understand the tools available for implementing this approach.

1.3 MOST Overview

The MOST project is a research effort focused on exploiting the benefits of parametric modeling of actively controlled next generation space telescopes. MOST is a fully parametric finite element modeling tool created to model the most critical design elements of a space telescope: bus and telescope structure, quasi-static and dynamic disturbances, and the active control system. The primary purpose for creating a fully parametric modeling tool is to obtain the capability of tweaking any design parameter and to rapidly assess the effect of that change on the optical performance metrics of the system. This rapid assessment capability allows for efficient trade space exploration, where large families of competing architectures can be quickly evaluated from a cost-to-performance tradeoff perspective.

This thesis contributes to only a subset of the objectives of the MOST project: mirror design and quasi-static mirror shape control. The details described in this chapter are included to provide the context in which this work was conducted and to highlight the goals and capabilities of the cumulative MOST effort.

1.3.1 Motivation for MOST

The motivation for developing the parametric modeling capability on MOST is primarily two-fold. The first motivation is to aid the traditional space systems design process. The traditional approach for developing highly complex space systems is to spend a small fraction of resources on a conceptual design study. This study seeks to identify, at most, a small number of competing architectures, or point designs, to evaluate in more detail. The level of complexity of these space telescope projects clearly limits the breadth of designs that can be considered, so the set of point designs is itself very limited.

One or more of these conceptual designs is eventually chosen based upon risk and performance merits to enter the preliminary design phase, during which more detailed analyses are conducted to produce more accurate assessments of system cost and performance. Should these assessments not meet mission performance requirements, a costly redesign effort of starting with an alternate architecture is then necessary. The emergence of new systems in industry demands a capability of assessing in detail a more complete set of competing architectures early in the design phase to avoid unnecessary redesign efforts late in the project life cycle.

The parametric modeling capability of MOST seeks to answer this demand. MOST offers a parametric design capability that allows vast trade spaces of competing space telescope architectures to be explored with relative computational ease. This investment in parametric modeling provides a more sound approach to the conceptual design phase of complex systems. An optimal design architecture can be rapidly generated and selected rather than a suboptimal point design chosen based on a limited investment of resources in the conceptual design phase. A conceptual design phase utilizing an analytical tool that exhaustively explores the design trade space will produce more robust designs for subsequent design stages.

The second motivation for the parametric modeling capabilities of the MOST project is to enable the advancement of less-proven technologies aboard space telescopes. The lack of flight heritage of certain space telescope technologies limits the advancement of the state of the art of these complex and costly systems. Designers typically opt for the less advanced, yet flight proven, design options since these telescopes are costly undertakings. In other words, the perceived risk of new technologies outweighs the proposed performance payoff they offer, and the technological development of space telescopes is hence decelerated.

In light of this skepticism towards advanced technologies, the parametric capability of MOST allows the design process to conduct a more in-depth analysis of such technologies. MOST offers the ability to rapidly assess the effect of various design changes on telescope performance metrics. The software backbone is available to introduce novel design changes to a particular space telescope architecture without a massive undertaking in simulation or prototyping.

1.3.2 MOST model

Given a set of user-defined design parameters, the MOST model automatically generates the structural design of the space telescope, models of representative dynamic disturbances, and the control systems used to mitigate such disturbances. Several resources exist ([10], [23]) for more detailed discussions of the design and implementation of such systems. An abbreviated summary of the MOST implementation is described herein.

There are three main computational stages of the MOST model: MATLAB for finite element model generation, Nastran as a finite element solver ([3], [25]), and the DOCS (Disturbance, Optics, Controls, Structures) MATLAB toolbox [8] for MATLAB-Nastran interfacing and various post-processing capabilities. FEMAP is also used for post-processing and model visualization. These stages and the associated computational platforms are pictured in Figure 1-2.

The computational sequence begins with the user-defined input parameters. All variable design parameters are defined simultaneously in a single input module, allowing greater accessibility to the user. These input parameters are then accepted by various MATLAB modules which generate the structural design of the telescope model. These modules auto-

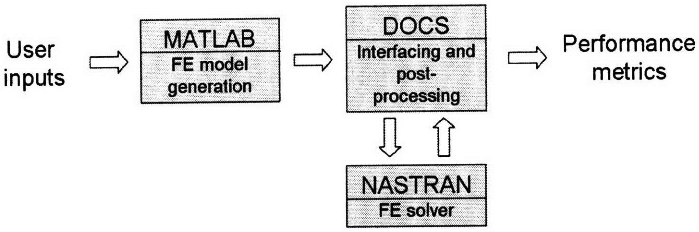

Figure 1-2: MOST model summary

matically generate the *bulkdata* structures, which house the grid pattern and finite element information for the physical structures.

The physical structure of the MOST model is defined in two main systems: the spacecraft bus and the optical telescope assembly (OTA). The bus model contains contributions from all major spacecraft subsystems, including solar arrays. A tetrahedral frame houses the subsystem components which are modeled as representative point masses using historical data as benchmarks [26].

The second system in the structural design of the MOST model is the OTA which includes all observation related equipment: primary mirror, secondary mirror, fast steering (or, tertiary) mirror (FSM), optics bench, and the secondary support tower. Each of these elements is generated separately for increased design modularity, and these individual modules are then integrated into a complete finite element model. A sample realization of the MOST model showing a hexagonal segmented primary mirror and pyramidal secondary support tower is shown in Figure 1-3.

Aside from the structural generation of this first computational stage, the MATLAB modules also model the dynamic disturbances imparted on the spacecraft and the control systems used to mitigate these disturbances. The disturbances are prescribed as power spectra density curves due to the vibrations of imbalanced reaction wheels [27]. These reaction wheels are themselves sized for the overall size of the spacecraft to permit identical slew rates, so the disturbances increase as the spacecraft becomes more massive.

The control systems to mitigate the effects of these disturbances are then modeled. The MOST model features passive isolators on two key structural interfaces: between the reaction wheel assembly (RWA) and the spacecraft bus and between the spacecraft bus and OTA. These isolators are modeled as low pass filters with variable corner frequencies. Additionally, there are up to four methods of active control aboard the MOST model,

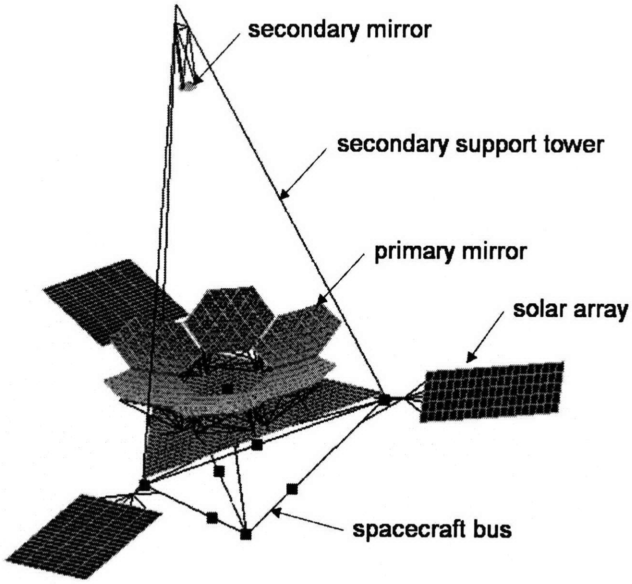

Figure 1-3: Sample MOST realization

depending on the type of primary mirror chosen by the user.

- **ACS** the attitude control system, modeled with torque inputs to each RWA
- **FSM** the fast steering mirror, featuring tip and tilt degrees-of-freedom (DOF)
- **Embedded actuators** embedded electrostrictive actuators in the primary mirror rib structure for mirror shape control
- **Petal control** rigid body tilting of hexagonal mirror petals for segmented mirror designs

With the finite element definitions of these structural components complete, and with the control authority defined for the various control systems, the data structures are then written to input files for Nastran via the DOCS MATLAB toolbox. Nastran conducts a normal modes analysis and outputs the mode shapes, frequencies, and total system mass.

Several performance metrics are calculated using the outputs from Nastran. First is the line-of-sight (LOS) jitter of the telescope model, or the error caused by both rigid body and flexible motion of the OTA in terms of its pointing steadiness. A second performance metric is the wavefront error (WFE) associated with figure error in the optical surfaces. This term is conventionally calculated using a set of Zernike coefficients of the primary mirror surface nodes as:

$$WFE = \sqrt{\sum \omega_i^2 \zeta_i^2} \tag{1.1}$$

where ζ_i are the Zernike coefficients and ω_i are the RMS weight factors, explained in more detail in Appendix B. Section 3.5.1 details an alternate method for quantifying the wavefront error since the Zernike polynomials do not necessarily contain the spatial bandwidth required to capture all mirror surface deformations.

Other performance metrics include slew and settle time of the telescope assembly for a given repointing operation. These metrics require the formulation of a state space system for the temporal simulation of these telescope maneuvers, which are also facilitated by the DOCS toolbox. A cost metric is also calculated using historical data to capture the effect of system parameters (e.g. mass, aperture diameter) on system cost. This number is presented as a relative metric to assess the differences in cost between competing designs.

1.3.3 Contribution to MOST

This thesis contributes to only a subset of the objectives of the MOST project. MOST offers the capability to explore trade spaces governing the entire telescope assembly, however, this thesis focuses on the optimization efforts specifically targeting the primary mirror. Furthermore, whereas many of the performance metrics of the telescope assembly deal with dynamic disturbances and time series maneuvers, the analysis presented herein focuses only on quasi-static disturbances and shape control.

The primary mirror model, or a hexagonal segment thereof, is separated from the rest of the telescope assembly for the purpose of analysis. The interface of the primary mirror to the telescope assembly is modeled with bipod mounts. Of the four control systems available for the entire telescope assembly, the system of embedded electrostrictive actuators is the only one investigated in this thesis. The interfacing bipods are assumed to perfectly control piston, tip, and tilt modes, as described in Chapter 3.

1.4 Thesis Roadmap

This thesis presents a study of the optimization of lightweight mirror segment design in terms of high spatial frequency surface error. Chapter 2 briefly reviews techniques for lightweight mirror control and design optimization from previous works and how the efforts of this thesis differ from these earlier endeavors.

Chapter 3 provides details of the mirror segment used throughout this thesis. The chapter provides details of the mirror model structural design, control system design, and of the methods used for shape control.

Chapter 4 discusses the concept of high spatial frequency surface error and the predominant causes of the three major sources thereof. The methods for simulating and quantifying each error source are included.

Chapter 5 discusses how the mirror and control system in Chapter 3 and the processes to simulate high spatial frequency residual in Chapter 4 are used to optimize the structural design of a hexagonal mirror segment. The chapter covers trade space exploration methods used for rapid optimizations and the specific objective function used to balance the effects of the various components of high spatial frequency residual. The results of multiple single axis trades are presented to depict the sensitivity of the structural parameters. Also, a sample trade space is presented as an example of the full factorial results included in Appendix A.

Lastly, Chapter 6 summarizes the key conclusions of this thesis. It includes a brief summary of Chapters 3 - 5, a list of the specific contributions of this thesis, and a discussion of the recommended areas of related future work.

Chapter 2

Literature Review

This chapter presents a brief summary of the recent progress made in the fields of mirror shape control and mirror design. Two competing methods for shape control algorithms are presented, as well as a variety of both conventional and unconventional mirror design techniques.

2.1 Mirror Shape Control

Methods used for mirror shape control generally differ only by the type of influence functions used. The influence function, discussed in Section 3.5, is the measured effect that one actuator has on the displacement of the mirror surface when the actuator is given a unit command. There exist multiple options for characterizing the effect on the mirror surface.

One type of influence function is the nodal influence function, which considers the out-of-plane displacements of each surface node in a mirror model. This method uses the set of calculated nodal influence functions and the set of nodal displacements in a given disturbance to solve for the necessary actuator commands to correct the mirror surface. For instance, Kapania [24] seeks to minimize the root-mean-square (RMS) figure error by solving for the necessary commanded displacements, u_i, of each mirror surface node using the equation for the RMS mirror surface error, E, directly:

$$E = \sqrt{\frac{1}{m}\sum_{i=1}^{m}(\psi_i + u_i)^2} \tag{2.1}$$

where m is the number of surface nodes in the mirror model and ψ_i is the initial disturbance displacement of the i^{th} surface node. Rewriting each commanded displacement, u_i, as the sum of the effects of each applied actuator force, f_j, via the influence functions (from actuator j to node i), α_{ij}, yields:

$$u_i = \sum_{j=1}^{n} \alpha_{ij} f_j \tag{2.2}$$

where n is the number of actuators. Solving for the minimum RMS surface error, where $\partial E/\partial f_k = 0$, yields the equation of the form $[A]\{f\} = \{b\}$,

$$\sum_{i=1}^{m} \left(\psi_i + \sum_{j=1}^{n} \alpha_{ij} f_j \right) \alpha_{jk} = 0 \qquad \forall\, k = 1, ..., n \tag{2.3}$$

where, assuming linear elastic behavior,

$$A_{kj} = \sum_{i=1}^{m} \alpha_{ij}\alpha_{jk} \tag{2.4a}$$

$$b_k = -\sum_{i=1}^{m} \psi_i \alpha_{ik} \tag{2.4b}$$

The approach in this example is similar to the one used throughout this thesis. It presents a number of control advantages over the Zernike influence function approach described next, and quantitative results for the accuracy of each approach are presented in Section 3.5.1. The notation for the shape control equation in both this example and that used in this thesis are compared in Equations 2.5.

$$[A]\{f\} = \{b\} \tag{2.5a}$$

$$\Sigma \bar{u} + \bar{z} = \bar{0} \tag{2.5b}$$

where, for the notation in this thesis, Σ represents the influence function matrix, $\bar{u}$ represents the set of actuator commands, and $\bar{z}$ represents the set of initial surface node displacements.

An alternative shape control approach is offered by Shepherd [31]. Here, a static gain matrix, K, is formed using the 42-term Zernike decomposition (see Appendix B) of the influence function of each actuator (when normalized for a one-volt command). In other words, instead of the influence functions representing the nodal displacements resulting from a particular actuator command, as in the previous example, the influence functions in this case represent the Zernike decomposition of each deformed shape. The process of gathering the influence functions therefore requires an additional transformation for each actuator. The influence functions become the columns of a system matrix, A. For a control system with seven actuators, the shape control equation to be solved is:

$$[A]_{42\times 7}\{v\}_{7\times 1} = \{z\}_{42\times 1} \tag{2.6}$$

where v represents the set of piezo-electric actuator voltage commands and z represents the 42-term Zernike decomposition of the desired shape command. Obtaining the desired shape command, z, therefore also requires an additional transformation via Zernikes. The required voltage inputs are given by,

$$\{v\} = [K]\{z\} \tag{2.7}$$

where

$$[K] = \left([A]^T[A]\right)^{-1}[A]^T \tag{2.8}$$

Since the number of actuators (seven) is less than the number of Zernike terms used in the influence function (42), the system in this example is *under-defined* (as discussed in Section 3.5), and solving Equation 2.7 yields the solution with the lowest residual, rather than canceling the residual altogether. Using a transformation of the influence functions into Zernike decompositions is a form of *modal* shape control, which controls particular modal shapes within the initial disturbance. A number of drawbacks to this approach are discussed in Section 3.5.1.

2.2 Mirror Design Optimization

2.2.1 Conventional Design Heuristics

Conventional techniques are used to size the mirror facesheet thickness using limits on maximum allowable surface error and material stress. Ealey [13] provides an example of how to use simplified design relationships to determine a suitable range of facesheet thickness. This approach uses a combination of maximum allowable print-through (detailed in Section 4.2, maximum allowable material stress, and a required actuator coupling factor.

The maximum allowable print-through determines a lower bound to the mirror facesheet thickness since the thin facesheet must provide adequate resistance to the polishing element to avoid severe print-through deformations. On the other hand, the maximum allowable material stress provides an upper bound on the facesheet thickness. For a given shape change (i.e. change in mirror curvature), a thicker facesheet results in greater peak stress on the outer edge of the material. The yield stress of the mirror material therefore determines the limit to how thick the facesheet can be.

Another example of facesheet thickness sizing is the following relationship for the peak-to-valley print-through deflection, δ, within a rib cell during the polishing process by Yong [37].

$$\delta = \frac{12\psi P B^4 \left(1 + \nu^2\right)}{E\, t_f^3} \tag{2.9}$$

where ψ is 0.00151 for a triangular cell pattern, P is the polishing pressure, B is the diameter of the largest inscribed circle within each rib cell, and t_f is the facesheet thickness. This relationship sizes t_f for a given set of mirror parameters. It is calibrated for various rib geometries using Nastran models, but it limits the user to a specific primary rib geometry and omits more effective, yet more complicated, rib structures (e.g. cathedralled).

These conventional design methods produce useful heuristics and sound initial design points, but have limited applicability due to their assumptions on rib geometry, constraints, and loading conditions.

2.2.2 Non-conventional Design Techniques

Optimization with genetic algorithms

Zhang provides one example of a non-conventional approach to mirror optimization with the use of genetic algorithms [33]. This family of algorithms follows from evolution theory by first randomly generating a set of initial design vectors representing a population of individuals. The individuals are evaluated using the chosen objective function and the "strongest" individuals recombine and mutate randomly to form the subsequent generation.

The individuals in the offspring generation therefore feature the best characteristics from the parent generation with stochastic perturbations of their chromosomes.

The algorithm runs until a maximum number of generations is reached or until a satisfactory performance is obtained from the candidate individuals. In the case of mirror design, Zhang defines the individuals as unique mirror architectures. Each is an octagonal, powered mirror segment with a hexagonal honeycomb rib structure featuring variability in rib cell size, facesheet thickness, rib thickness, and rib height. The standard form of the mirror optimization is as follows:

$$\begin{aligned} \text{Find}\, \bar{X} &= [x_1, x_2, ..., x_n] \\ \min M &= f(\bar{X}) \\ \text{s.t.}\, g_j(\bar{X}) &< 0 \;\; j = 1, 2, ..., J \end{aligned}$$

where X represents the design vector, M is the chosen objective function, and $g(\bar{X})$ is the set of constraints. Zhang offers example constraints such as mirror stiffness (measured by the fundamental frequency), mirror strength (measured by mirror stress), and total mirror mass. The objective function to be minimized is the RMS mirror surface residual caused by a given disturbance.

The algorithm is conducted via the optimization module of ANSYS and results are presented for a sample optimization using a series of 30 generations. This application of genetic algorithms shows that efficient trade space exploration methods are possible for complex mirror design. The results, however, are constrained to a very specific mirror geometry and objective function, and the optimality of the final design is not guaranteed.

Topology optimization

Another example of a non-conventional approach to mirror design is Park's topology optimization process [30]. Topology optimization offers an alternative approach to shape optimization for structural design. *Shape optimization* requires the optimal solution to take the form of allowable geometric shapes (such as a triangular or hexagonal mirror rib structure), whereas *topology optimization* overcomes the shape limitations by searching the continuum of geometric possibilities.

The authors apply the theory of topology optimization to lightweight mirror design by formulating a two-dimensional indicator function X representing the material density at all discretized points on the mirror backstructure. The term *backstructure* herein refers to the lightweight array of ribs that supports the mirror facesheet (i.e. *rib backstructure*, similar to *backplane* as used by How [20]), rather than to a massive and comparatively rigid support structure. The 64cm diameter, monolithic annular mirror model is constructed of Zerodur and has a 20cm diameter centered hole. It is constrained by three clamped locations on the outer mirror wall spaced at 120°.

The problem takes the mathematical form as follows:

$$\begin{aligned} \min M &= f(\bar{X}) \\ \text{s.t. } h_i(\bar{X}) &\leq 0,\ 1 \leq i \leq M \\ g_j(\bar{X}) &= 0,\ 1 \leq j \leq N \end{aligned}$$

where $\bar{X}$ represents the design vector, $f(\bar{X})$ represents the objective function, and $h(\bar{X})$ and $g(\bar{X})$ represent the constraints. Here the design vector $\bar{X}$ represents the density function of the mirror, or the local mass density at all discretized locations on the mirror backstructure. The resulting optimal solution, $\bar{X}^*$, is the two-dimensional density function for the mirror mass distribution that minimizes the objective function and satisfies all constraints. The mirror is assumed to have at least a thin facesheet at all locations, so the density function represents the backstructure density.

The authors provide a mirror optimization example where $f(\bar{X})$ quantifies the surface RMS error and the system Strehl ratio for a mirror under both self-weight and polishing pressure. A uniform polishing pressure of 207Pa is used, similar to the 225Pa pressure used in the print-through simulation example in Chapter 4.

The optimization example is constrained such that the feasible space satisfies a 22% mass ratio, which is the ratio of the mass of the final design relative to a solid mirror of 65mm thickness. Prescribing a particular mass ratio is analogous to prescribing an areal density, as is done in this thesis. The optimal design for this exercise is found via the topology optimization process in roughly 40 iterations. It reduces the RMS mirror surface deflection to 39.4nm, from the 90nm initial condition ($\bar{X} = \bar{0}$, zero backstructure density). The optimal backstructure features six predominant rib spokes supporting the facesheet emanating from the three rigid support locations. This solution is also verified for manufacturing constraints such as a minimum rib thickness.

The result from this topology optimization exercise is compared to a lightweight mirror with a hexagonal cell pattern and of the same total mass. The optimized mirror deflects under self-weight and polishing pressure to an RMS of 134.4nm compared to 156.6nm for that of the hexagonal cell mirror. A vertical gravity sag test was also conducted, but the optimized mirror showed negligible change over the hexagonal cell mirror.

Park's work shows an excellent extension to non-conventional structural design techniques. The results for mirror mass distribution are interesting and clearly useful as the optimized mirror shows improvement over a popular hexagonal honeycomb rib structure. The variable density rib structure that results, however, is poorly receptive to embedded actuation. Park shows how the straight-edged rib patterns, popular in lightweight mirrors today, are suboptimal for particular objective functions, but the shaped cell patterns do allow for mirror shape control via embedded actuators. In addition to modeling actuators, the optimization approach in this thesis seeks to quantify the effectiveness of the shape control system. Control system optimization is a topic that Park's work does not cover, although an extension of the optimization routines for such topics would be useful.

2.3 Summary

This chapter presented several examples from published literature in work related to the topics covered in this thesis. This chapter showed that a number of methods are available for mirror shape control, including different forms of influence functions. Both nodal and Zernike influence function forms are evaluated in this thesis (Section 3.5.1), and the tradeoffs for each form are discussed.

This chapter also showed that a broad range of mirror design techniques are available. Conventional techniques take a simplified heuristic approach to mirror design by using simple beam and shell theory. These methods produce relationships across selected design variables and point designs that satisfy design constraints. The results, however, do not capture the complexities of a lightweight, rib-stiffened mirror structure and the coupling relationships of the numerous structural parameters.

Chapter 3

Mirror Design and Shape Control

Lower areal density mirrors are susceptible to thermal, manufacturing, and dynamic distortion, and these effects have led to the field of active (and adaptive) optics. In short, active optics encompasses the design of an optical system to correct for distortion in the captured wavefront. Figure 3-1 summarizes the correction process of a typical active optics system.

As an aside, *active optics* must not be confused with *adaptive optics*. When the distortion in the wavefront is dynamic and corrections are made at frequencies above 1Hz, the appropriate term is *adaptive optics* [18]. Adaptive optics typically refers to systems controlling for external errors (e.g. atmospheric distortion). Otherwise, for quasi-static disturbances or when the time constant of the disturbance is large, the term *active optics* is appropriate. These quasi-static disturbances typically arise from internal error sources.

The distortion in the wavefront can be attributed to one of two error sources. The first is the medium through which the system observes its target object. Any changes in the refractive properties of the medium in the time the wavefront traverses it causes a distortion in the wavefront. Two portions of the same wavefront that traverse mediums of different refractive indices travel at different speeds, and the wavefront becomes distorted. An everyday example of this is the perceived twinkle of stars seen through a turbulent atmosphere by the naked eye. Light from the same source reaches the eye at different times, so without wavefront correction, the stars appear to twinkle. The same atmospheric turbulence plagues all ground-based telescopes, so they require active correction of the incoming wavefront to produce high resolution images. This example of distortion is the one pictured in Figure 3-1.

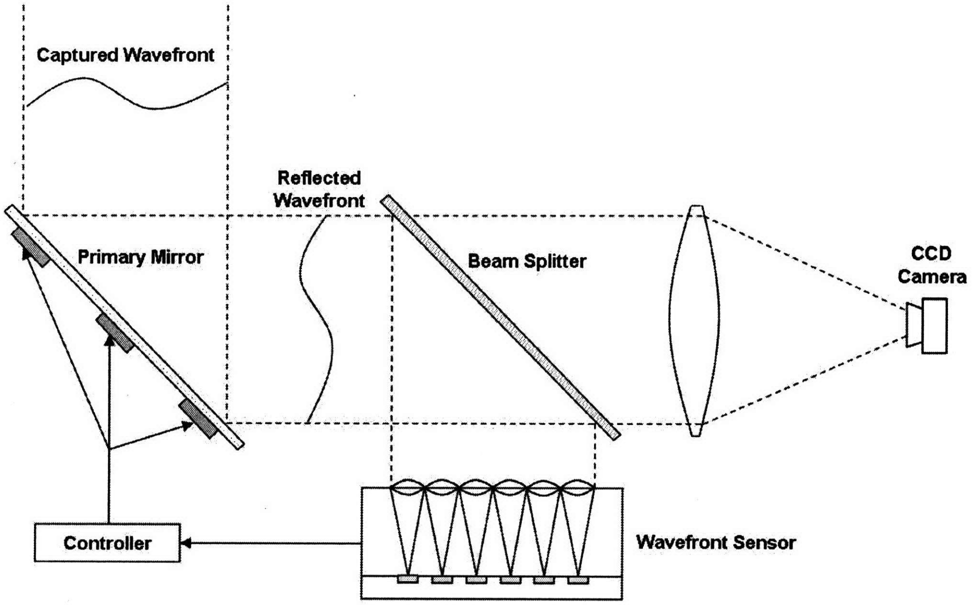

Figure 3-1: Diagram of typical active (or adaptive) optics systems for a distorted incoming wavefront [32]

The second source of distortion for an active optics system is the optical system itself: the series of lenses and mirrors. Should any element in the optical path deviate from its prescription, the transmitted or reflected wavefront becomes distorted. This wavefront error is influenced by each imperfect optical surface, and these distortions can add constructively or destructively. A common example of this type of distortion is an out of focus camera. The lens system of the camera produces an image of the target object at the system's focal plane. If the focal plane does not align with the image detector, the image appears out of focus. The ability to focus a camera by altering the relative location of its lenses, specifically by moving them laterally along the optical axis to redirect the focal plane onto the image detector, is a common example of an active optics system.

This thesis considers only quasi-static distortions (i.e. quasi-static mirror corrections). In other words, the rate of change of the distortion is assumed to be well within the high bandwidth of the sensing and control system. This thesis also considers only distortions in the wavefront due to imperfections in the telescope's primary mirror. The approach of concentrating on primary mirror distortions is common for active space telescopes since their target objects are viewed through the vacuum of space, so the observed wavefront is

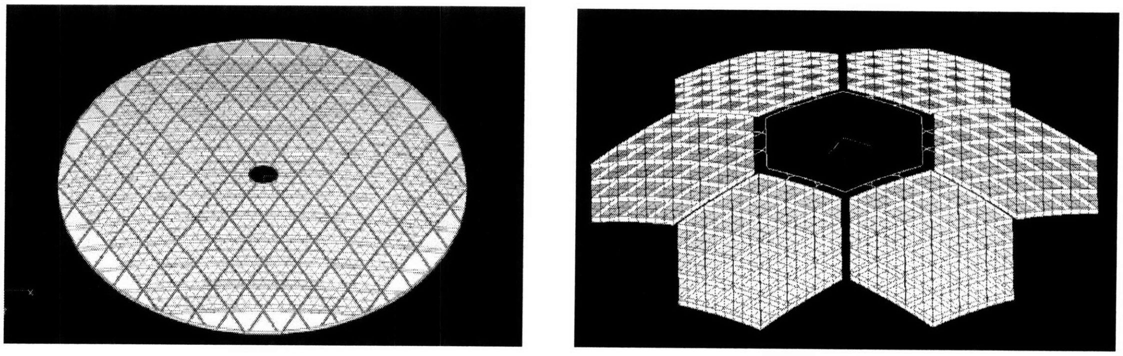
(a) (b)

Figure 3-2: Example primary mirror realizations by MOST for (a) a monolithic circular mirror and (b) a hexagonal segmented mirror. View is of the backstructure.

not distorted by a turbulent atmosphere. Furthermore, the trend towards larger and lighter mirrors leads to more flexible structures, so errors in the mirror figure are increasingly more common aboard next generation space telescopes.

3.1 Mirror Structural Model Overview

The MOST project has the capability to automatically generate a finite element model for a space telescope, including models of the primary, secondary, and fast-steering (tertiary) mirrors, given a number of user-defined parameters. The annular primary mirror is modeled as either a monolith or as an assembly of hexagonal segments. Of the two main choices for a segment mirror geometry [5], hexagonal segments provide fair coverage of the desired annular aperture while using segments that are nearly identical in shape (in contrast to rings of radial petals). The prescription for the off-axis hexagonal segments is a function only of the radial distance from and orientation to the aperture center. This symmetric shape allows for more convenient auto-generation of the finite element models as well as more cost-effective manufacturing. Example MOST realizations of both a monolith and a segmented annular mirror are shown in Figure 3-2.

The telescopes modeled by MOST are designed to be the state-of-the-art of space telescopes. The mirror designs feature lightweighting techniques including a thin mirror facesheet supported by an array of stiffening ribs that comprise the backstructure. The term *backstructure* herein refers to the array of ribs that supports the mirror facesheet, rather than to a massive and comparatively rigid support structure. The rib structure pat-

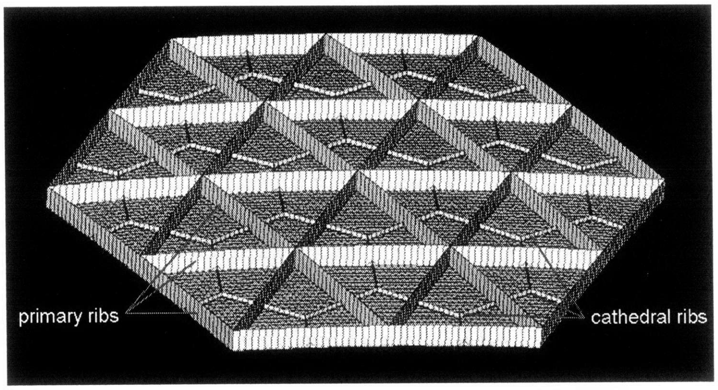

Figure 3-3: Rib structure pattern of a hexagonal mirror segment including cathedral ribs as generated by MOST

tern for both mirror geometries mimics those seen in industry [15]. This thesis, however, focuses only on hexagonal mirror segments. The rib structure for one of these segments is pictured in Figure 3-3. This structure features a layout of the primary ribs in a pattern of equilateral triangles. The user defines this layout using the number of concentric, hexagonal rib rings desired. The rib structure in Figure 3-3, for instance, has two concentric "rib rings."

In addition to the "primary ribs" which appear in a triangular pattern, the MOST model has the capability to generate "cathedral ribs," which form a secondary rib structure of smaller ribs within the triangular cells of the primary ribs. These smaller cathedral ribs are designed to support the mirror facesheet at its weakest points, with little added mass, to reduce uneven polishing when a surface pressure is applied. More detail on the design and implementation of these cathedral ribs can be found in Section 3.2.

The mirror segments are modeled with a homogeneous material since these segments are often cast or milled from a solid blank of material [5]. A thin reflecting surface is typically added to the structural material, but this thin coating provides a negligible change in the structural or thermal properties and is thus neglected in the MOST model.

The following sections describe the design parameters of the mirror segments and the properties of the assembled primary mirror. These definitions lay the foundation for the shape control methods described later in this chapter.

Table 3.1: User-specified mirror segment design parameters

Specified Parameter	Baseline Value
Diameter (flat-flat)	1m
Radius of curvature (on axis)	6m
Areal density	15 kg/m^2
N_{rings}	2
Facesheet mass fraction	50%
Cathedral rib mass fraction	5%
Primary rib aspect ratio	50
Cathedral rib aspect ratio	4

Table 3.2: Silicon carbide material property summary

Material Property	Value
Elastic modulus, E	375 GPa
Shear modulus, G	26 GPa
Poisson's ratio, ν	0.17
Mass density, ρ	3200 kg/m^2
Thermal expansion coefficient, CTE	4.5×10^{-6} m/°C

3.1.1 Mirror segment parameters

The user has authority over several design variables governing the structure of the primary mirror segments. For consistency, however, a fixed mirror design is used throughout this thesis unless noted otherwise. The parameters for this design are meant to be consistent with what is seen in industry for fairly large segmented and lightweight mirrors [18]. The parameters shown in Table 3.1 specify the mirror design for any baseline examples given in this thesis. Also for reference, Table 3.2 summarizes the silicon carbide (SiC) properties used for the homogeneous mirror material.

The areal density listed includes the added mass of the actuators, but not of any additional mounting hardware or electronics. Refer to Section 3.3 for a review of the electrostrictive actuator model properties. Also note that the user has the freedom to vary the mirror facesheet and the cathedral rib mass fractions. Each mass fraction is the ratio of allocated mass for that component to the total mirror structural mass. The mass fractions determine how mirror structural mass is distributed between the facesheet, primary ribs, and cathedral ribs for a given areal density. The value for N_{rings} is the number of hexagonal rib rings in the rib backstructure. Lastly, the rib aspect ratios equal the height of each rib divided by the cross-sectional thickness.

Table 3.3: Derived mirror parameters

Derived Parameter	Baseline Value
Segment mass	13kg
No. of actuators	42
Actuator mass	10g (each)
Primary rib height	32.7mm
Cathedral rib height	6.6mm

In addition to the user-specified mirror parameters, a number of derived parameters are worthy of note. These parameters are not directly chosen by the user, but rather are determined indirectly from the prescribed parameters. An abbreviated list of key derived parameters is shown in Table 3.3.

Note that the height of the cathedral ribs is required to be no greater than that of the primary ribs. The cathedral rib structure is intended to be a secondary backstructure for providing support within each of the primary rib triangular cells. For this reason, mass allocations that demand taller cathedral ribs than primary ribs are avoided altogether. With regards to the finite element implementation, the thicknesses of the mirror facesheet and ribs are prescribed as thickness values of the planar elements used to generate the finite element model of the mirror. Visualizations of the mirror thus do not depict these thicknesses.

3.1.2 Segmented primary mirror parameters

The mirror segment parameters described in the previous section describe a single segment in a multi-segment primary mirror. From a MOST modeling perspective, the only difference between mirror segments is the prescribed mirror figure, which depends only on the radial distance from the primary mirror center. The structural parameters are hence modeled identically across each of these off-axis segments.

The hexagonal mirror segments modeled in this thesis are designed to populate a 3m diameter parabolic primary mirror. This primary mirror requires six of the hexagonal segments described in the previous section: one ring of six identical off-axis segments. Figure 3-4 shows the segmented mirror and the individual segments necessary.

Each segment is supported identically using a set of three bipod mounts that attach to particular points on the backstructure (see Section 3.4). In addition to the shape control

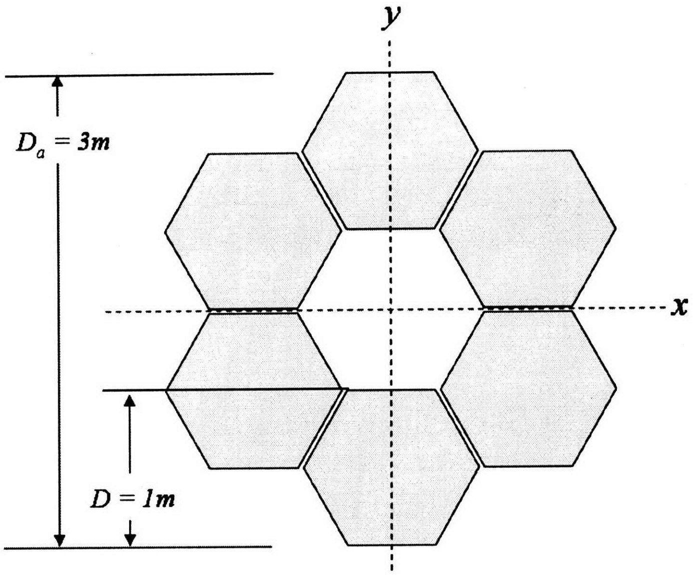

Figure 3-4: Primary mirror and its hexagonal segments

made possible by the embedded actuators (see Section 3.3), each of the six off-axis mirror segments can be actuated in piston, tip, and tilt directions with these bipods, although the independent rigid body control of the off-axis segments is not considered in this thesis. For simplicity, this thesis considers only the shape control of a symmetric mirror segment as if it were centered on the x, y, and z axes, which are shown in Figure 3-4 and 3-5. This avoids complexities of an asymmetric off-axis prescription and an asymmetric shape control system. It also permits computational savings as described in Section 5.2.2 which utilize the 60° rotational symmetry of the mirror structure.

The overall primary mirror is modeled as a 3m diameter aperture with a focal length of 3m as shown in Figure 3-4. This results in an f-number of one and a radius of curvature (RoC) of 6m by the following definitions:

$$f/\# = \frac{f}{D_a} \qquad RoC = 2f \tag{3.1}$$

where f is the mirror focal length and D_a is the aperture diameter. For this reason, the model for the on-axis segment also has an f-number of one and a 6m RoC for its 1m diameter (flat-flat).

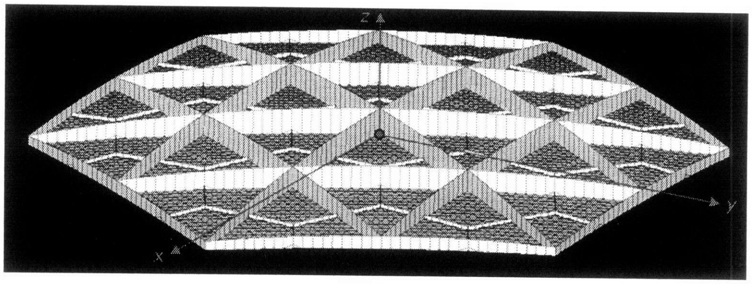

Figure 3-5: Sample MOST realization of hexagonal rib-stiffened mirror segment. View shows mirror backstructure.

3.2 Cathedral Rib Structure Design

This section presents several aspects about the design of cathedral ribs as an improvement to the backstructure of a rib-stiffened, lightweight, deformable mirror. The motivation for introducing a secondary rib structure, or ribs smaller in height and length compared to their primary rib counterparts, is first presented. The design options for the cathedral rib pattern are then introduced and the merits for choosing the appropriate pattern are discussed. Finally, the details of the finite element implementation are discussed, covering how these cathedral ribs are introduced to the existing parametric modeling process and the auto-meshing capabilities it possesses.

This section covers only the design and implementation of the cathedral rib structure. Refer to Chapter 5 for results on the optimization of the cathedral rib design parameters.

3.2.1 Motivation for cathedral rib structure

A rib-stiffened, lightweight, deformable mirror typically features a thin facesheet with a backstructure pattern of high aspect ratio primary ribs. This rib-stiffened design increases the structural rigidity in the transverse ($\pm z$ in Figure 3-5) mirror bending direction using limited structural mass. By concentrating the mirror mass in strategically sized and located ribs, the mirror facesheet can be made very thin to help produce low areal density mirrors. An example realization of a rib-stiffened deformable mirror similar to that seen in industry is shown in Figure 3-5.

Two back structure patterns are evident in Figure 3-5: one *primary rib* pattern (whose geometry creates triangular cells between the ribs) to support the entire mirror, and a secondary *cathedral rib* pattern designed to provide support within the triangular rib cells.

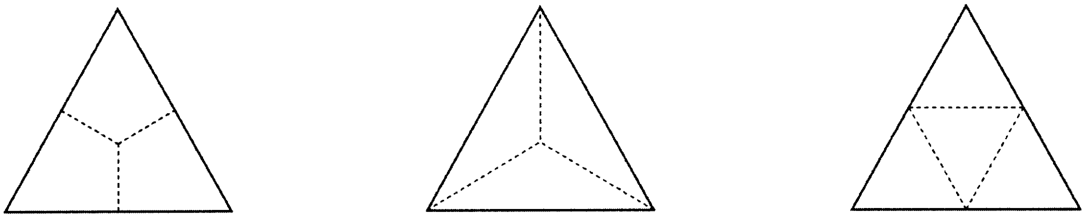
(a) midpoint (b) endpoint (c) triangular

Figure 3-6: Cathedral rib pattern options within a representative primary rib cell

These cathedral ribs are included to strengthen the weakest areas of the deformable mirror, where the mirror facesheet is otherwise unsupported by the primary rib backstructure.

The large gaps (triangular cells) in the primary rib structure are problematic primarily due to manufacturing concerns and the effect of print-through, or quilting. Print-through originates from the polishing process when the mirror facesheet deflects non-uniformly under the polishing pressure and is explained in more detail in Section 4.2. The mirror facesheet thickness is hence driven not only by the structural requirements from operations, but also by the mirror's structural rigidity during manufacturing [5].

The two competing demands on the mirror backstructure - to carry structural loads across the diameter of the mirror and to provide rigidity in a homogeneous fashion to avoid print-through effects - suggest that the optimal mirror backstructure features a multi-tiered structural design. For this reason, the MOST model generates cathedral ribs whose structural parameters are optimized in Chapter 5. The following sections discuss the design and implementation of cathedral ribs in the MOST mirror model.

3.2.2 Options for cathedral structure

Several options exist for the cathedral rib pattern within each of the primary rib triangular cells. Three possible options are shown in Figure 3-6 for a representative primary rib triangular cell and include a *midpoint*, *endpoint*, and *triangular* layout.

These competing cathedral rib patterns are judged on three design merits: ease of finite element implementation, structural mass efficiency, and the pattern's ability to support the centermost points of the mirror facesheet within each representative rib cell. The first design merit considers the ease with which the pattern can be implemented into the existing mirror autogeneration module. This merit is a function of how the proposed cathedral elements

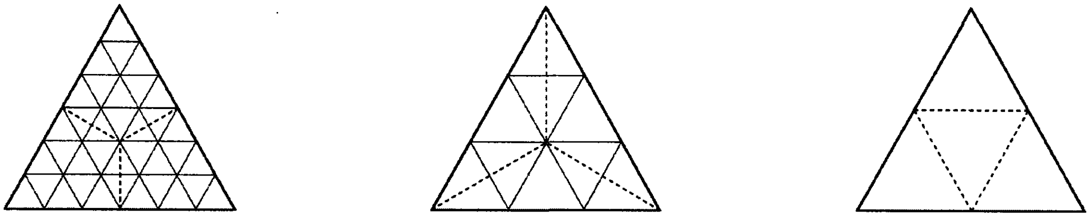
(a) midpoint (b) endpoint (c) triangular

Figure 3-7: Minimum fidelity surface mesh for cathedral rib pattern options

blend with the existing mirror surface and primary rib elements. The goal is to avoid finite element misalignments or asymmetries within the primary rib triangular section and to create a robust auto-meshing algorithm for any combination of mirror structural parameters.

The height of the quadrilateral cathedral rib elements is allowed to vary, but the heights of the ribs are always oriented in the z-direction (along the mirror optical axis and not along the surface-normal direction). The ability of the cathedral rib elements to blend with the existing elements therefore depends on the layout of the underlying mirror surface triangular elements (shown in Figure 3-7), and whether they can be easily re-meshed while preserving the symmetry within each rib cell.

The *triangular* pattern requires a node only at the midpoint of the surrounding primary ribs, so the pattern blends with any surface mesh for N_t even, where N_t is the number of elements across any edge of the triangular primary rib cell. Similarly, the *endpoint* pattern blends with the underlying mesh when N_t is any integer multiple of three. The *midpoint* pattern blends with any mesh fidelity when N_t is an integer multiple of six. Whereas all three cathedral rib patterns work with particular mesh fidelities, the choice of pattern clearly restricts the model fidelity to particular values of the number of finite elements per meter.

The second merit is the structural mass efficiency. This merit can be interpreted as evaluating the patterns based on the total length of ribs required. The pattern with the least total rib length produces the largest ribs for a given cathedral mass. For a unit length primary rib cell, the candidate patterns result in total rib length per rib cell as summarized in Table 3.4. The *midpoint* cathedral pattern clearly offers a mass-efficient layout, and is nearly twice as efficient as the next most effective candidate design.

The final merit for the choice of the cathedral rib pattern is whether the cathedral ribs extend to the centermost location of the rib cell, where the otherwise unsupported facesheet

Table 3.4: Total cathedral rib length for unit length rib cell

Cathedral Pattern	Total Length
Triangular	1.50
Endpoint	1.73
Midpoint	0.87

is most vulnerable to print-through error. The *endpoint* and *midpoint* patterns accomplish this, whereas the *triangular* pattern does not.

The *midpoint* method is selected on the basis of substantial mass efficiency and the ability to provide structural support to the centermost facesheet location within each rib cell. The mesh fidelity limitation of the *midpoint* pattern is a tradeoff for the mass savings it offers. All cathedral rib implementations in this thesis feature ribs in such a layout.

3.2.3 Finite element implementation

Aside from the mesh fidelity limitations of the midpoint cathedral pattern detailed in the previous section, there exist additional concerns for the finite element implementation of the quadrilateral cathedral rib elements. This section first details the re-mesh logic used to blend the cathedral ribs into the existing underlying triangular element mesh (see [23]) and then discusses the test used to ensure asymptotic convergence to show model accuracy.

Re-mesh logic

A number of re-meshes are necessary to ensure continuity of the cathedral rib elements with adjacent finite elements. The goal of the re-mesh logic is to avoid FEM discontinuities while using as few additional nodes and elements as possible.

The re-mesh algorithm is designed to overcome the two FEM discontinuities shown in Figure 3-8(a). The first occurs between the quadrilateral cathedral rib and the underlying triangular facesheet mesh. Figure 3-7(a) shows that for $N_t = 6n \, (n \in N)$ each cathedral rib spans a multiple of two facesheet triangle elements. For each cathedral rib and each pair of underlying adjacent surface triangles, one new quadrilateral cathedral rib element and two new triangular facesheet surface elements are added (Figure 3-8(b)).

The second FEM discontinuity occurs at the intersection of the cathedral ribs and the existing primary ribs. The height of the cathedral ribs is smaller than that of the primary ribs, so the outer edge of each cathedral rib does not coincide with any existing primary rib

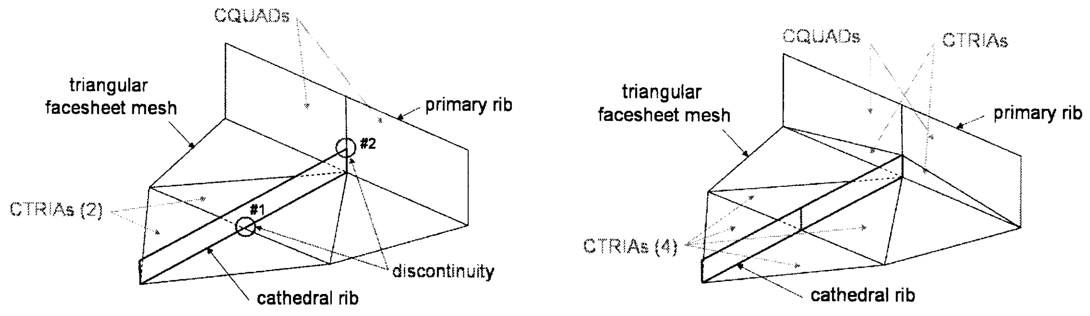

(a) (b)

Figure 3-8: Cathedral rib discontinuities (a) before re-mesh, and (b) after re-mesh

nodes, as shown in Figure 3-8(a). The re-mesh logic that minimizes the number of additional elements adds two triangular elements to each rib intersection as shown in Figure 3-8(b).

Model convergence

To test the accuracy of the updated model containing cathedral ribs, the model fidelity (number of nodes per meter) is increased and the convergence behavior of a model metric is recorded. The model is said to converge if this metric asymptotes to some value as model fidelity is increased. The point at which the metric sufficiently asymptotes dictates the required level of model fidelity to produce consistent and accurate results.

The addition of triangular elements (in the process of modeling cathedral ribs) motivates a test for convergence of the mirror model. These triangular elements are necessary to maintain continuity between neighboring elements when the cathedral ribs are added, but are believed to be generally more error prone than quadrilateral elements in finite element models. Selected modal frequencies are used as the metric to test for model convergence.

As explained in Section 3.2.2, the number of finite elements along each edge of the primary rib triangular sections, N_t, must be an integer multiple of six to allow the *midpoint* cathedral rib pattern to blend with the existing element mesh of the mirror surface. The varying spatial fidelity thus depends on the number of triangular sections across the mirror diameter, which in turn depends on the number of hexagonal rib rings of the mirror backstructure. Refer to Section 3.1 for a more detailed discussion on the layout of the mirror backstructure. The minimum required number of facesheet elements across the diameter (vertex-to-vertex) is given by:

$$N_{ele} = 12 \times N_{rings} \tag{3.2}$$

where N_{rings} is the number of concentric, hexagonal, primary rib rings in the mirror backstructure (e.g. $N_{rings} = 2$ in Figure 3-5). In general, dividing the number of elements by the length spanned by those elements gives the spatial model fidelity. For a given vertex-to-vertex mirror diameter, D_v, the spatial fidelity of the FEM must therefore be a multiple of:

$$\text{\# elements/m} = \left\lceil \frac{N_{ele}}{D_v} \right\rceil \tag{3.3}$$

where the $\lceil \cdot \rceil$ indicates the integer ceiling operation. A 1m flat-flat diameter mirror gives $D_v = 1m \cdot \sec(30°) = 1.155\text{m}$ vertex-to-vertex diameter and the minimum required spatial fidelity levels listed in Table 3.5.

Table 3.5: Minimum spatial fidelity levels

N_{rings}	$\lceil N_{ele}/D_v \rceil$
2	21
3	32
4	42

The two-rib ring mirror requires fidelity levels in integer multiples of 21 elements per meter (# elements/m $= 21n$). The first five multiples ($n = 1, 2, 3, 4, 5$) are used to test modal frequency convergence on the two-rib ring mirror. The convergence results for the 7th, 10th, and 20th modal frequencies are shown in Figure 3-9. Note that the 7th modal frequency is that of the first flexible mode after the six rigid body modes. The convergence behavior shows that the selected modal frequencies sufficiently converge over the range of fidelity levels chosen. The change in each of the frequencies shown between the two highest fidelity levels ($n = 4, 5$), 84 and 105 elements/m, is less than 1Hz.

The modal convergence test evaluates the accuracy of the model alone. However, a number of metrics also involving actuation are used in the optimization routines in Chapter 5. Verifying the accuracy of calculating actuation-induced deformation is thus also important. The mirror dimpling metric (defined in Section 4.1) is used on the two-rib mirror for this metric convergence test. The fidelity levels vary from 20 to 105 elements per meter at increments of roughly 4 elements per meter. The results for the dimpling RMS residual

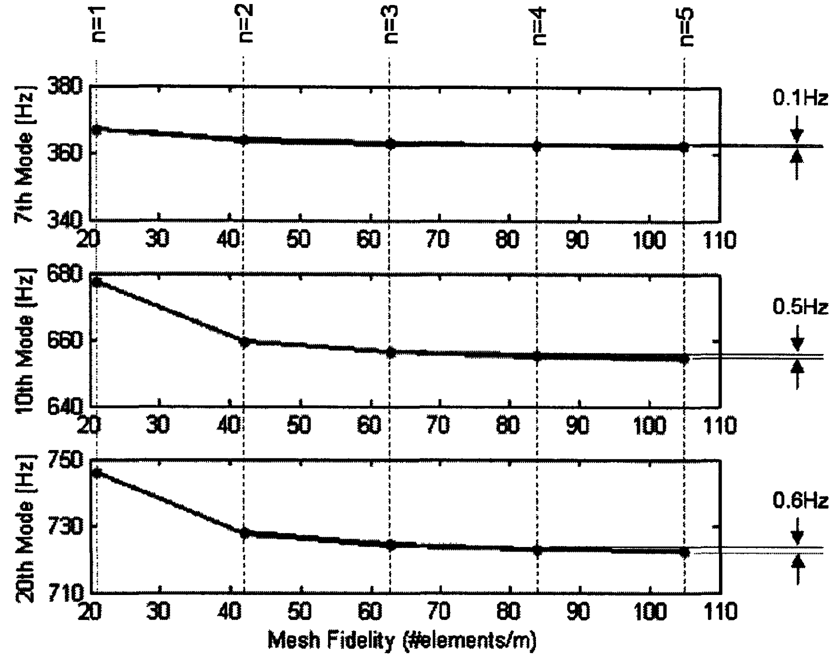

Figure 3-9: Modal frequency convergence behavior

across this range of model fidelity are shown in Figure 3-10.

The convergence behavior in Figure 3-10 shows that the dimpling metric sufficiently converges to within a ±5% interval at fidelity levels greater than 42 elements per meter ($n = 2$). The convergence behaviors of the modal frequencies and the dimpling metric imply that a fidelity level of at least 42 elements per meter ($n = 2$) is required to achieve accurate and reliable simulation results. A fidelity level of 63 elements per meter ($n = 3$), corresponding to roughly 4000 mirror model surface nodes, is used throughout this thesis to ensure accurate and reliable model data.

3.2.4 Effect of cathedral ribs

The purpose of including cathedral ribs in the design of a deformable mirror is to produce a more homogeneous structural design that mitigates short spatial wavelength deformations. These deformations can appear in the control of the mirror or in the manufacturing process as "print-through," as described in Section 4.2.

To give a preview of the motivation for the optimization in Chapter 5, consider the following. The overall effect of cathedral ribs at mitigating print-through is measured by

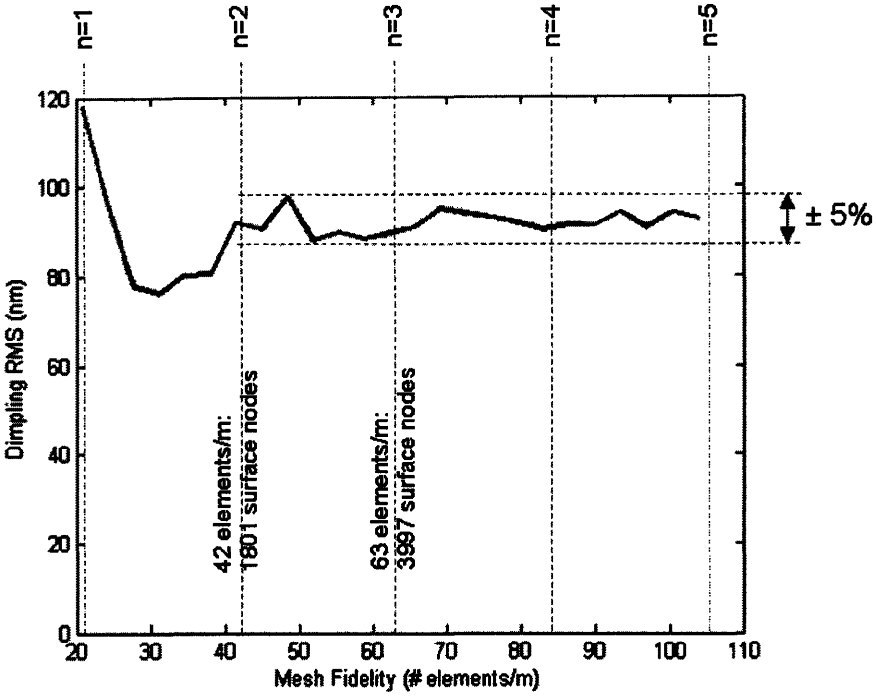

Figure 3-10: Mirror dimpling metric convergence behavior

increasing the cathedral mass fraction and recording the print-through RMS on the baseline mirror design. As the cathedral rib mass fraction is increased, the facesheet and primary rib mass allocations are decreased equally to maintain constant areal density. The results for print-through RMS as a function of cathedral mass fraction are shown by the solid line in Figure 3-11.

Increasing the cathedral rib mass fraction monotonically decreases the print-through residual, but it has an adverse effect on the dimpling RMS, shown by the dashed line in Figure 3-11. This trade between print-through and dimpling residual presents the opportunity for structural optimization against these high spatial frequency error sources. The process for quantifying these residuals, and the routines for optimizing the mirror structural parameters accordingly, are described in Chapters 4 and 5.

3.3 Actuator Modeling and Layout

The actuators modeled for mirror shape control in this thesis are embedded surface-parallel electrostrictive actuators. The forces applied by the actuators produce a local surface

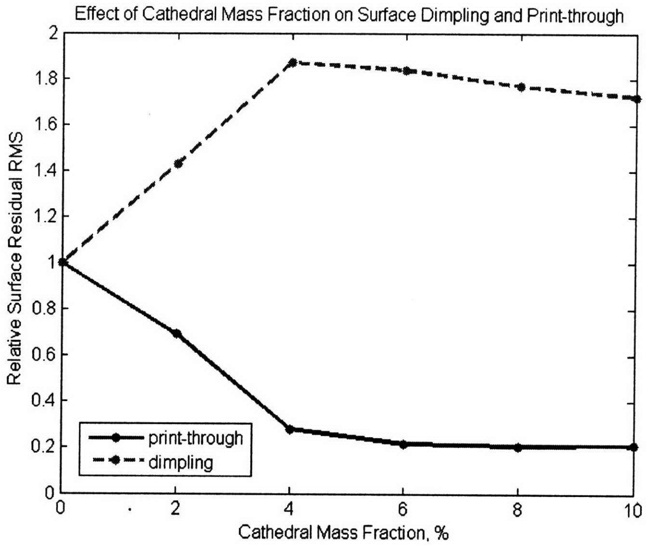

Figure 3-11: Effect of cathedral rib mass fraction on relative print-through and dimpling residuals

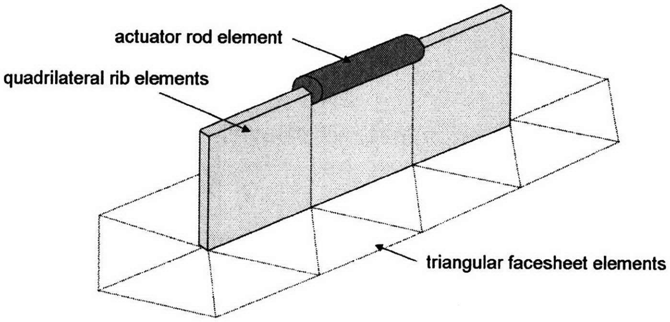

Figure 3-12: Geometry of surface parallel actuator model

bending moment without requiring a massive support structure to provide a reaction force. Each actuator is mounted on the outside edge of a primary rib (farthest from the facesheet) and is modeled as a cylindrical rod element in Nastran [23]. These rod elements span an integer number of quadrilateral elements depending on the desired length specified by the user. Figure 3-12 depicts the geometry of the surface-parallel cylindrical electrostrictive actuators relative to the underlying quadrilateral rib elements.

The actuator d_{33} term is also specified by the user. The d_{33} term determines the longitudinal strain of the actuator under free-free boundary conditions given a unit applied voltage [18] as:

Table 3.6: Number of actuators as a function of rib rings

N_{rings}	No. of Actuators
2	42
3	90
4	156
5	240

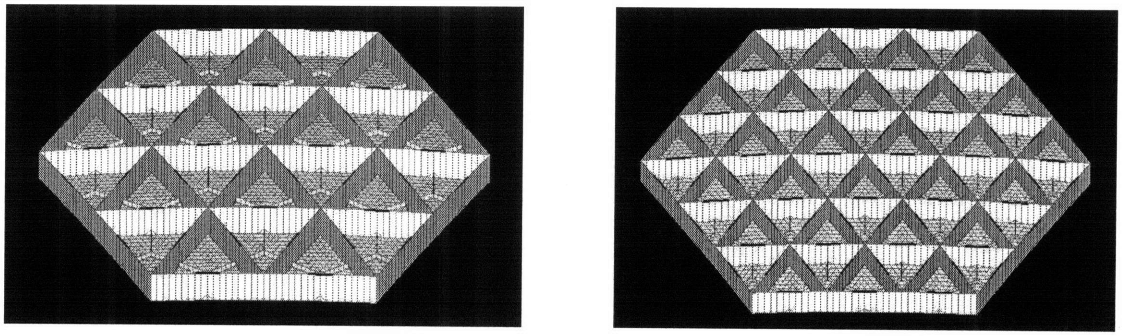
(a) (b)

Figure 3-13: Embedded actuator layout for (a) 2 rib ring mirror, and (b) 3 rib ring mirror

$$d_{33} = \frac{\Delta L}{V} \tag{3.4}$$

where ΔL is the longitudinal expansion of the actuator and V is the applied voltage. The d_{33} term plays a role in the modeling of the actuators, which are controlled by varying the actuator element temperatures as explained in Section 3.5.1.

The layout and number of actuators is solely a function of the rib geometry. An actuator is centered on all edges of each rib cell, so the number of actuators depends only on the number of hexagonal, concentric primary rib rings, N_{rings}, as listed in Table 3.6. Sample actuator layouts for mirrors with two and three rib rings are shown in Figure 3-13.

The actuator models are controlled via applied temperatures which cause the elements to expand/contract (depending on the stiffness of the structure in which they are embedded) to produce the desired endpoint displacements. An alternate control approach is to apply equal and opposite forces at either end of the actuators [10]. The choice of control approach depends on a number of factors, but predominantly rests on how the electrostrictive is believed to behave. As *relative force actuators*, the actuators impart a particular level of force on the attached rib structure (given a chosen level of applied voltage), regardless of the displacement of the surrounding structural material. This model of actuator behavior

Table 3.7: Summary of actuator model properties

Actuator Property	Value
α, CTE	3.6×10^{-10} m/°C
d_{33}	3.6×10^{-4} m/V
ρ, density	7650 kg/m^3
E, elastic modulus	93 GPa
G, shear modulus	10 GPa
ν, Poisson ratio	0.3
r, radius	3mm
L, length	2.5cm

exists in the limit when the surrounding rib material is significantly stiff in comparison to the actuator itself [20], so the desired level of applied force is produced independent of actuator displacement.

As *relative displacement actuators*, however, the actuators undergo a particular longitudinal displacement (given a chosen level of applied voltage), regardless of the surrounding stiffness. This actuator behavior model exists in the limit when the surrounding rib material is very weak compared to the stiffness of the actuator [20], so the actuator is free to expand/contract to a prescribed amount independent of the reaction force of the surrounding material.

In reality, the embedded actuators are hybrids of these two models. The actuators perform neither exactly as theoretical force actuators nor as displacement actuators, but rather somewhere in between. To mimic this behavior, a chosen level of temperature change, ΔT, is applied and the actuator element expands/contracts longitudinally (under free-free conditions) as:

$$\frac{\Delta L}{L} = \epsilon = \alpha \, \Delta T \tag{3.5}$$

where L is the original actuator length, ϵ is the element strain, and α is the coefficient of thermal expansion (CTE). The elongation of the actuator and the stiffness of the surrounding structure provide a balance between the relative displacement and relative force actuator models. In other words, the commanded temperature in the embedded actuator model causes the actuator to strain until the stress in the actuator (due to its inability to achieve free-free strain) balances the stress in the structure (due to deformation). A summary of the actuator model properties is shown in Table 3.7.

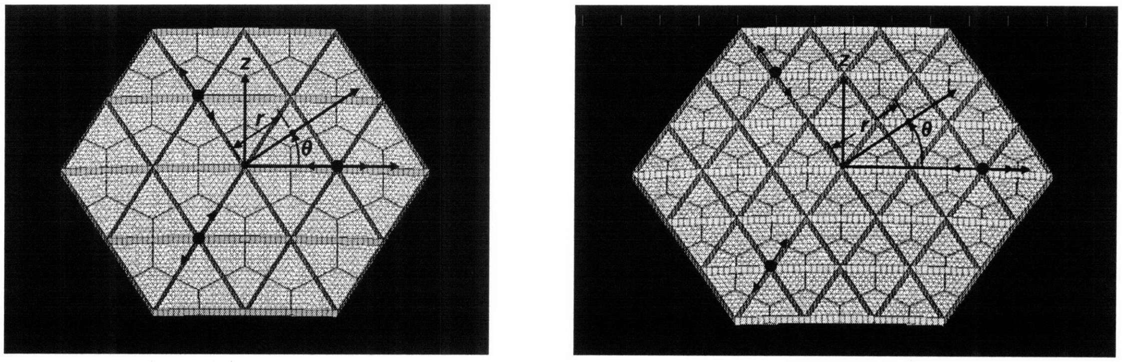

(a) (b)

Figure 3-14: Point constraint geometry showing degrees of freedom for (a) 2 rib ring mirror and (b) 3 rib ring mirror

3.4 Constraints

The primary mirror must be appropriately constrained for two reasons. The first is to prevent rigid body motion of the mirror that could occur because of applied disturbances. The second is to mimic the support of the adjoining telescope in order to more accurately model the mirror mounting.

In order to prevent rigid body motion of the primary mirror, the mirror must be constrained in six degrees of freedom (DOF): three translational and three rotational. This is accomplished by constraining three different points on the mirror backstructure in two degrees of freedom each. Each constrained point is at the intersection of primary ribs at the point farthest from the facesheet. These three points match the attachment points of bipod mounts that would be used to connect the mirror to the telescope. In this way, the rigid body modes of the mirror are constrained while mimicking the support nature of the telescope assembly.

The three points chosen for constraints vary depending on the chosen mirror backstructure geometry. All three points lie on the same hexagonal rib ring and are spaced at 120° intervals about the mirror center. The rib ring of point constraints is the centermost ring along any radial vector ($N_{rings}/2$), or one ring outside the half radius if N_{rings} is odd. The three point constraints are identified for mirrors with two and three rib rings in Figure 3-14.

Each of the point constraints is constrained in the same two degrees of freedom: the circumferential θ (relative to mirror x, y plane) and z-direction (along optical axis). Each constrained point is allowed to slide in the radial direction (along the arrows in Figure

3-14) and rotate about any axis, mimicking the behavior of kinematic bipod mounts. The combination of these six constraints fully constrains the rigid body modes of the mirror.

3.5 Method of Shape Control

This thesis takes a conventional approach to shape control (as seen in [23], [35]) by solving the system of equations in Equation 3.6.

$$\Sigma\bar{u} + \bar{z} = \bar{0} \tag{3.6}$$

where $\bar{z}$ represents the known mirror surface node (initial) z-displacements (displacements along the optical axis), Σ represents the matrix of actuator influence functions, and $\bar{u}$ represents the set of actuator commands. The influence functions represent the influence of the actuators on the z-displacements of each facesheet surface node in the finite element mirror model and are explained in the following section. The matrix Σ has a number of rows equal to the number of mirror surface nodes and a number of columns equal to the number of embedded actuators used for shape control. This means Σ is generally not square (typically taller than wide) so several numerical solving methods, discussed in Section 3.5.3, are possible for finding the actuator commands, $\bar{u}$.

In general, solving for the required actuator commands yields:

$$\begin{aligned} \Sigma\bar{u} + \bar{z} &= \bar{0} && (3.7\text{a}) \\ \bar{u} &= -\left(\Sigma^T\Sigma\right)^{-1}\Sigma^T\bar{z} && (3.7\text{b}) \end{aligned}$$

which requires premultiplying by Σ^T to obtain a square system. This system is inherently difficult to solve due to poor conditioning of the influence function matrix, which is exacerbated by pre-multiplying by its transpose. This poor conditioning also introduces problems associated with the numerical solving technique, further discussed in Section 3.5.3.

As a summary, Figure 3-15 shows the theoretical mirror shape control process when the influence functions are known. The surface node z-displacements of the mirror surface are first gathered. Equation 3.6 is next solved for $\bar{u}$ using the z-displacements and the recorded influence function matrix Σ. Once the actuator commands are applied, the *surface residual* can be found by differencing the corrected shape from the desired shape.

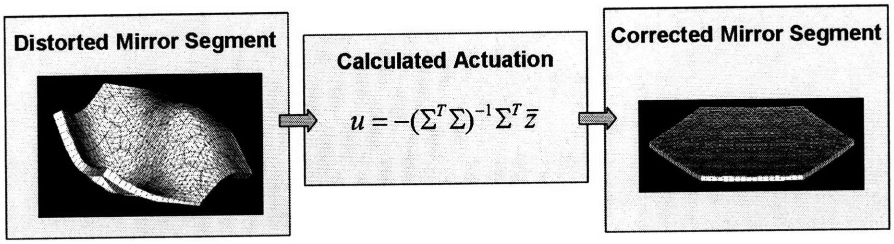

Figure 3-15: Theoretical mirror shape control summary

Additionally, all shape control commands in this thesis consider only a 95% clear aperture of the hexagonal mirror segment. The clear aperture is defined as the set of points on the mirror surface that lie within a circle 95% the size (by radius) of the largest possible inscribed circle within the hexagonal segment. Only mirror surface nodes within the clear aperture are used in the set of displacements $\bar{z}$ and in the influence functions in the matrix Σ. All surface residual metrics, therefore, pertain only to points in the clear aperture. However, all actuators for the commands in $\bar{u}$ are used for shape control even though some actuators lie outside the clear aperture.

Use of a clear aperture calculation avoids peculiarities associated with edge control. Moment actuators (e.g. the surface-parallel actuators used herein), or those that impart nearly a pure bending moment in the mirror structure, struggle to smoothly control the surface curvature near the edges of the mirror segment. These control difficulties are avoided altogether through use of a clear aperture for the purpose of the shape command simulations. Note, however, that the resulting large surface residual near the edges of the segment adversely affects the wavefront error and the system's imaging capability.

3.5.1 Influence functions

The influence function of an actuator is the resulting mirror surface shape when that actuator is given a unit command. The matrix Σ contains the complete set of influence functions and is required to solve Equation 3.6. The theoretical influence functions used in this thesis are obtained by applying a unit actuation command to each actuator in series and recording the Nastran output for the z-displacements of each surface node in the finite element mirror model. Sample influence functions for various actuators are shown in Figure 3-16 using the Nastran result for the deformed mirror.

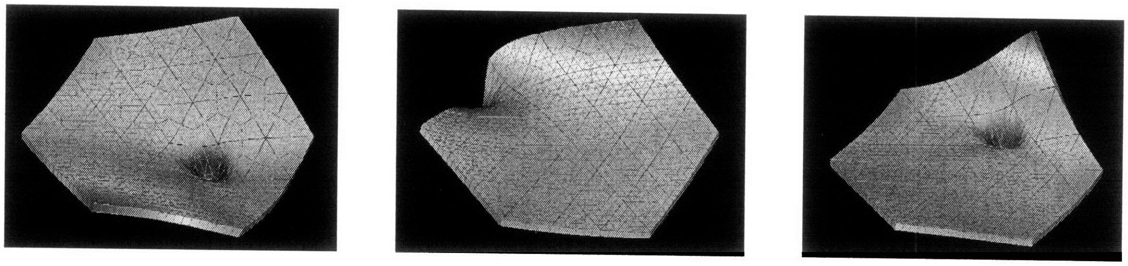

(a) Actuator #6 (b) Actuator #25 (c) Actuator #44

Figure 3-16: Sample influence functions

The format of these influence functions is also of interest. As mentioned, this thesis implements *nodal influence functions* which record the displacement of each facesheet surface node. *Zernike influence funcetions* offer an alternative approach to shape control.

Zernike influence functions

Zernike influence functions decompose the deformed mirror surface into a particular number of Zernike coefficients and use this set of coefficients as the influence function (as in [23], [31]). Similar to Equation 3.6, Equation 3.8 is the governing control equation when Zernike influence functions are used.

$$\Sigma_z \bar{u} + \bar{\zeta} = \bar{0} \tag{3.8}$$

where Σ_z is the Zernike influence function matrix and $\bar{\zeta}$ is the set of Zernike coefficients of the initial mirror figure to be controlled. As with nodal influence functions, the required actuation is calculated such that the set of Zernike coefficients of the controlled mirror surface is minimized (in absolute value). This Zernike influence function approach results in a compact and elegant method for controlling the mirror figure. The Zernike terms also add an element of convenience since basic optical aberrations correspond to Zernike shapes such as focus, astigmatism, and coma [18].

This Zernike approach also has a number of drawbacks. Primarily, this method has a spatial bandwidth limitation; that is, it entirely neglects shapes (i.e. Zernike polynomials) of order higher than the bandwidth used for Zernike decomposition. This is because the Zernike polynomials are an orthogonal series, so shapes above the chosen spatial bandwidth are rendered unobservable. Consider a shape control case that uses the first 48 Zernikes for the control bandwidth. Any portion of the shape disturbance that lies above this bandwidth

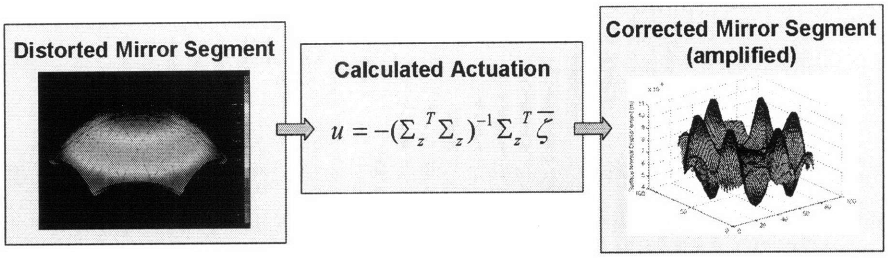

Figure 3-17: Example of Zernike control bandwidth limitation

is unobservable and uncontrollable, regardless of the number of actuators used. This bandwidth limitation is depicted in Figure 3-17. Very high spatial frequency errors or defects (i.e. "microroughness" [5]) lie above a reasonable Zernike influence function bandwidth, where a *reasonable* Zernike bandwidth is defined as one which permits a shape decomposition in less than three seconds (e.g. a ~4000 node facesheet surface shape can be decomposed into 156 Zernike shapes in ~1.5 seconds). It is thus very difficult to control for high spatial frequency shapes using Zernike influence functions.

A second drawback of the Zernike control approach is the following ambiguity of spatial bandwidth that it introduces. A given set of z-displacements can be decomposed into any number of Zernike coefficients since the series of Zernike polynomials is infinite. As long as the Zernike influence function matrix Σ_z has full column rank, which it is observed to have, then any number of Zernike terms equal to or less than the number of actuators are controllable. That is, if the number of actuators used is greater than the number of Zernikes controlled (Σ_z is wider than it is tall), the system is said to be *over-defined* and solving Equation 3.8 yields a non-unique solution.

If the number of Zernike terms controlled is instead greater than the number of actuators (Σ_z is taller than it is wide), the system is said to be *under-defined.* Solving Equation 3.8 yields a solution that minimizes the system residual, typically in a least squares sense, instead of solving for the exact solution. A Zernike decomposition using a large number of terms is also computationally expensive because it requires a Zernike transformation in addition to the matrix solution to Equation 3.8. The additional time necessary for this transformation is significant and is reflected in Table 3.8 for multiple cases.

Furthermore, high-order Zernike polynomials feature high spatial frequency radial terms which have many oscillations concentrated near the edges of the unit circle. Sampling these shapes sufficiently on the mirror surface requires at least two surface nodes per cycle (i.e. Nyquist sampling [29]), which requires a higher fidelity mirror model and even greater computational expense.

The spatial bandwidth of the controller presents a tradeoff. A smaller bandwidth neglects higher order terms and a larger bandwidth requires a least squares minimization of the residual and a large Zernike transformation. This tradeoff is complicated by the multitude of different mirror designs studied by MOST and by the variety of disturbances to which the mirrors are subjected. A particular choice of controller Zernike bandwidth may be optimal for one choice of mirror and disturbance, but sub-optimal for another combination. This bandwidth ambiguity is the second drawback of the Zernike control approach.

Nodal influence functions

The control approach in this thesis uses nodal influence functions, which avoid the aforementioned drawbacks of the Zernike control approach. Since the number of nodes on the finite element mirror surface exceeds the number of actuators, Equation 3.6 is *under-defined*, and the numerical method chosen minimizes the residual of the system since it cannot be corrected completely.

This nodal approach avoids the bandwidth issues of the Zernike approach altogether. As a result, the nodal influence functions generally produce controlled mirror surfaces with a lower root-mean-square (RMS) displacements compared to using Zernike influence functions. Table 3.8 compares the surface RMS residual for these mirrors following a bulk $1°\Delta T$ [C] athermalization (i.e. correcting for thermal deformation) using the nodal and Zernike control approaches. The Zernike approaches listed use 156 terms, even though the two and three-rib mirrors have only 42 and 90 actuators, respectively. Table 3.8 shows that the nodal influence functions produce on average 10% less residual in the controlled mirror surface. This higher accuracy is another reason that nodal influence functions are the control method of choice for this thesis.

In summary, nodal influence functions are chosen over Zernike influence functions because of their accuracy and minimal computational requirements. A fair comparison between the two methods would feature Zernike influence functions with the same number of terms as there are surface nodes in the mirror model. This would result in the matrices Σ and Σ_z being the same size. For mirror models with thousands of nodes, however, the

Table 3.8: Controlled surface residual results for nodal and 156-term Zernike influence functions (IF) for 1°ΔT bulk athermalization

No. Actuators	Surface Residual (nm)		Computation Time (s, per 1000 nodes)	
	Nodal IF	Zernike IF	Nodal IF	Zernike IF
42	4.96	5.88	0.001	15.4
90	2.35	2.42	0.01	32.5
156	1.20	1.34	0.05	56.2

necessary Zernike transformations would be prohibitively expensive in computation time.

3.5.2 Fictitious actuators

In addition to the embedded electrostrictive actuators included in the finite element mirror model, three "fictitious" actuators are included in the influence function matrix to control for piston, tip, and tilt. Columns associated with these actuators are appended to Σ and Equation 3.6 is solved with the modified matrix.

Including these actuators mimics perfect piston, tip, and tilt actuation from the telescope assembly. Although these modes are typically controlled using bipod-mounted actuators, the assumption of perfect control is ambitious. This assumption is necessary, however, to avoid numerical issues with the embedded actuators trying to control the rigid body modes. For instance, Figure 3-18 shows the controlled mirror surfaces with and without the use of fictitious actuators when correcting for a bulk temperature disturbance. Note both the shape and vertical scale in these images. The relative ability of the control system to athermalize the surface is apparent when piston, tip, and tilt correction is used. The corrected surface is more homogeneously controlled to a lower RMS residual.

Furthermore, the command profiles with and without the use of fictitious actuators is shown in Figure 3-19. These command profiles are shown as color maps where each color represents the level of command voltage and the locations of the plotted points represent the actuator locations on the mirror. The effect of the fictitious actuators is again apparent in these command profiles, as the embedded actuators control the surface with less numerical difficulty when the fictitious actuators are included, resulting in a radially smooth pattern with significantly lower RMS voltage. Note the magnitudes of the color scales in these images. Due to the control advantages, three fictitious actuators are used for all shape control simulations in this thesis.

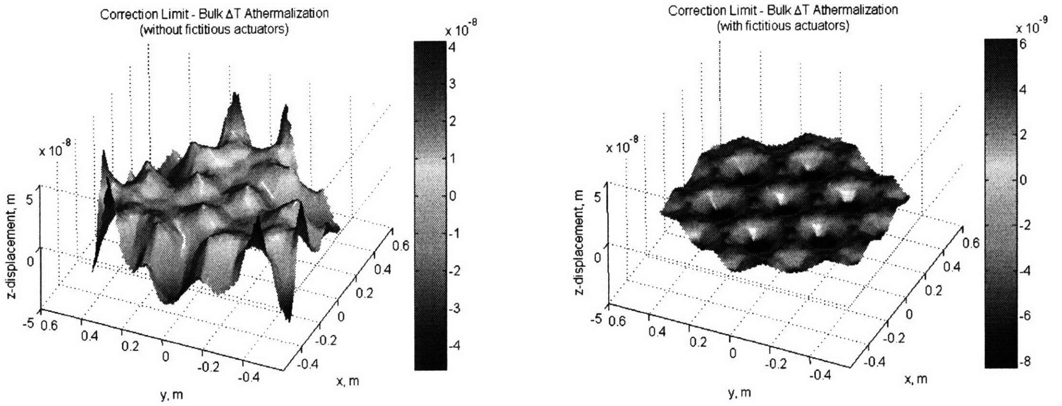

(a) (b)

Figure 3-18: Controlled mirror surface (a) without fictitious actuators, and (b) with fictitious actuators (note vertical scale)

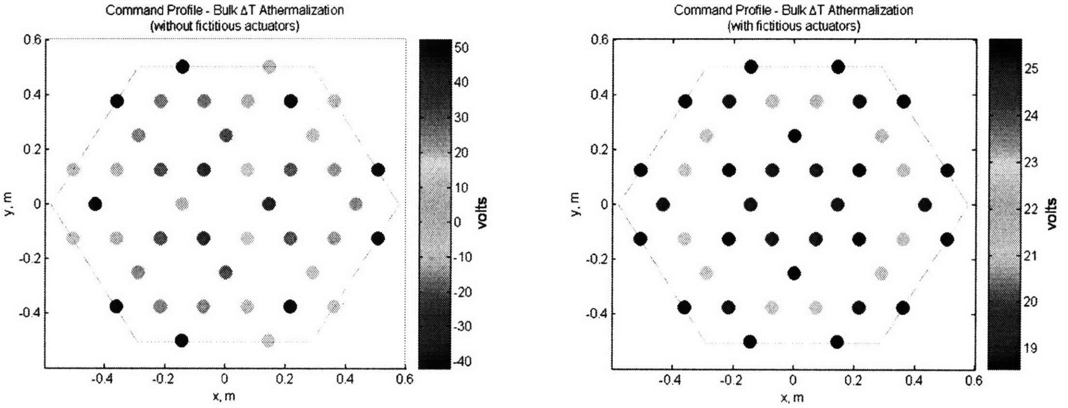

(a) (b)

Figure 3-19: Bulk ΔT athermalization command profiles (a) without fictitious actuators, and (b) with fictitious actuators

Table 3.9: Summary of numerical methods to solve $Ax = b$

`lsqr`	Finds the least squares solution x while minimizing the residual $Ax - b$
`inv`	Finds the complete inverse; $x = A^{-1}b$
`mldivide`	Matrix left divide; $x = A\backslash b$
`pinv`	Uses the Moore-Penrose pseudo-inverse; finds the solution with the smallest 2-norm
`tgcr`	Truncated generalized conjugate residual (GCR) [12].

Table 3.10: Numerical methods performance

Method	Tolerance	Accuracy (nm)	Computation Time (s)
`lsqr`	1×10^{-16}	1.879	0.0312
`inv`	N/A	1.555	0.0528
`mldivide`	N/A	1.555	0.1001
`pinv`	1×10^{-16}	1.555	0.0645
`tgcr`	1×10^{-16}	1.555	0.0248

3.5.3 Numerical methods

Solving Equation 3.6 for the required actuation levels, $\bar{u}$, is not necessarily trivial. This is because the influence function matrix is poorly conditioned and the proper choice of numerical solving method is critical for optimizing the performance in terms of both accuracy and computation time. MATLAB has many built-in numerical solvers and each is designed for a slightly different purpose. Table 3.9 summarizes several numerical solvers, the first four of which are MATLAB functions. Each is used to solve the equation $Ax = b$ for the vector x.

The tradeoff for the numerical methods is between computation time, accuracy, and sensitivity to tolerance level. Some methods operate very quickly, whereas other methods produce solutions for x with much lower residuals $(Ax - b)$. A survey of the methods for both the computation time and the accuracy sheds light on the most efficient solver: that which provides an accurate answer in reasonable computation time. Table 3.10 summarizes the review of the methods under consideration, with the chosen tolerance level listed when applicable. The mirror corrected is the baseline 2-rib mirror (defined in Tables 3.1 - 3.3) under a $1^\circ \Delta T$ bulk temperature disturbance.

Also worthy of note is the sensitivity of each method to the chosen tolerance level.

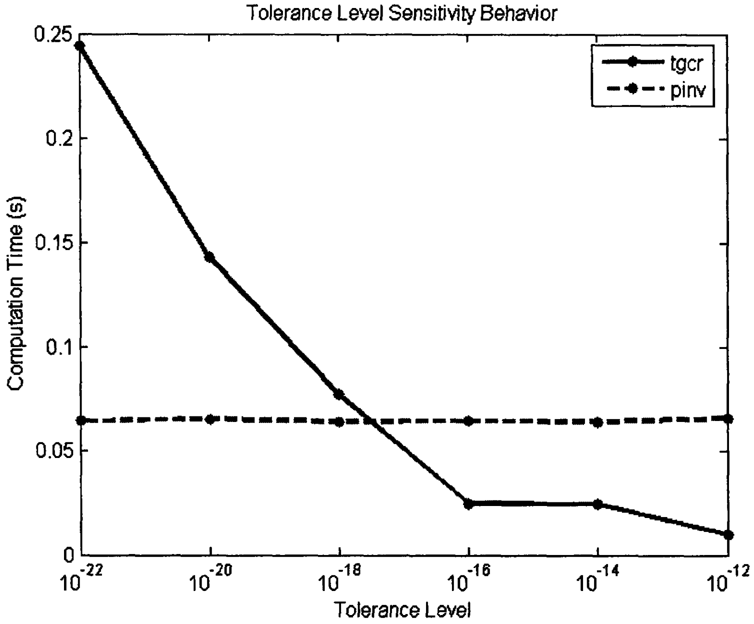

Figure 3-20: Tolerance level sensitivity of `tgcr` and `pinv`

Many of these methods run until the chosen tolerance level for the residual is reached, so decreasing the tolerance level generally produces more accurate results with the cost of increased computation time. In addition to providing accurate results in reasonable time, a method which is fairly insensitive to the chosen tolerance level is also desirable. Truncated GCR (`tgcr`), for instance, is highly sensitive to tolerance level for such ill-conditioned calculations. Figure 3-20 shows this tolerance level sensitivity by plotting the computation time of both `tgcr` and `pinv` for a range of tolerance levels. The accuracy (i.e. controlled surface RMS residual) for all tolerance levels is 1.555nm. This plot implies that small changes in the tolerance level for `tgcr` may result in very large changes in the computation time for negligible improvements in accuracy.

As Figure 3-20 also shows, the pseudo-inverse function (`pinv`) is insensitive to tolerance level for this example. Changing the tolerance level results in no severe change in computation time. The accuracy of `pinv` for all tolerance levels is also 1.555nm. This lower sensitivity is desirable, especially in Chapter 5 when many mirror models are generated and evaluated automatically. Robust and insensitive functions are valuable in such an automated process. For these reasons, the pseudo-inverse is used for all equation computation. It is chosen over the inverse function since `inv` is known to grow exponentially in computation time relative to the size of the system solved.

3.6 Summary

This chapter presented details of the design and control of a deformable mirror segment model. The mirror segment evaluated in this thesis is a lightweight, silicon carbide, hexagonal segment featuring a thin facesheet and a combination of primary and cathedral ribs as a stiffening backstructure. The mirror segment is defined using a number of user-specified structural parameters, and a series of baseline parameters define a mirror that is used as a baseline design throughout this thesis.

The embedded actuators are modeled as rod elements on the outside edge of each rib section, and they push and pull on the primary ribs, parallel to the mirror surface, to create surface displacement patterns (i.e. influence functions) used for shape control. The mirror shape control approach employs nodal influence functions and three fictitious actuators to smoothly and accurately control for a given quasi-static mirror shape disturbance.

Chapter 4

High Spatial Frequency Mirror Surface Residual

The lightweight design of next generation space telescope mirrors introduces many performance errors not present in the high areal density, monolithic predecessors. Mirror shape control systems are designed to attenuate such figure errors, and the embedded control systems used today have been shown to effectively mitigate many global shape disturbances [23].

However, the rib-stiffened design and discrete nature of most control systems (i.e. compact actuators distributed across the mirror backstructure at discrete locations) introduces the concept of uncontrollable, high spatial frequency surface error. Mathematically, any figure error that lies outside the control space (spanned by the shapes of the actuators' influence functions), results in uncontrollable residual. Generally speaking, these residual shapes are uncontrollable because their spatial frequencies lie above the frequency of the actuator spacing on the mirror backstructure. The actuators have no control authority over these high order shapes [5].

High spatial frequency surface errors originate from a variety of sources and can be classified as either actuation-induced, manufacturing-induced, or disturbance-induced error. This thesis considers only quasi-static, thermal disturbances for disturbance-induced error due to the prevalence of such disturbances in space telescopes. A given mirror, based on its structural design, manufacturing process, and operational environment can be plagued by any combination of these three error sources, as shown in Figure 4-1.

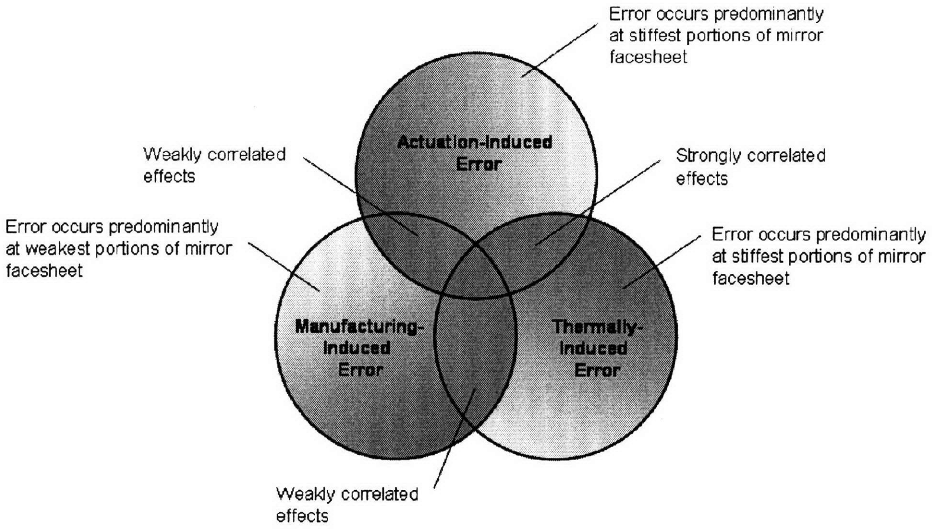

Figure 4-1: Coupling relationship of three high spatial frequency error sources

This chapter explores in detail the three major sources of high spatial frequency mirror surface error and quantifies the relative prevalence of each for a typical deformable mirror. The results of this study are applied in Chapter 5, which discusses how these different error sources are treated in the optimization objective function and the subsequent optimization of the mirror geometry to best mitigate the combination of these effects.

4.1 Actuation-Induced Residual: Dimpling

A short spatial wavelength error inevitably appears when a discretely actuated deformable mirror is corrected for a long spatial wavelength, or "global," error. This high frequency residual is termed *dimpling* since the error resembles a pattern of repeated circular dimples across the mirror surface. The dimpling effect appears on theoretical mirror models, so the modeling capability of MOST can be utilized to better understand the cause of mirror dimpling.

Dimpling is attributed to the spatially discrete nature of the mirror shape control system. Discrete actuators control the mirror curvature in a very localized region surrounding the actuator itself. Mathematically, the control law patches these localized corrections together to form the best fit global solution for the desired overall curvature. The mirror surface locations farthest from actuators are the most difficult to control and tend to exhibit the

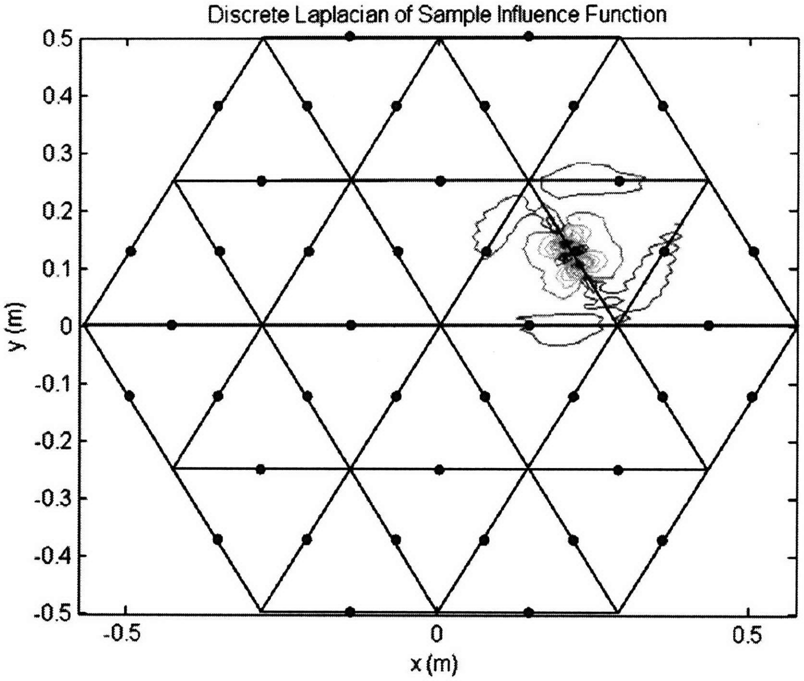

Figure 4-2: Contour plot of mirror curvature induced by one actuator

most actuation-induced error.

The shape of the actuator influence functions is also attributed to the discrete nature of the control system. Although the actuators produce z-displacements across the entire mirror surface, the surface curvature they produce is very localized. Figure 4-2 shows the mirror curvature associated with one influence function (using contours that show locations of constant surface curvature), computed via the Laplacian of the mirror surface nodes. Also shown are the locations of all ribs (lines) and actuators (dots) for reference. The concentration of the contours indicates that the induced curvature from a single actuator is very localized. Since the control law patches these influence functions together to command any desired shape, a smooth curvature command is difficult to achieve given the localized shapes of the influence functions. Dimpling results because the curvature of the mirror cannot be corrected smoothly across the entire surface.

The combination of mirror structural parameters determines the shape of the individual influence functions. A stiffer structure generally results in more global influence functions for the actuators. In other words, the induced curvature from any actuator will be smoother across a larger region of influence for stiffer mirrors, rather than being very localized on flexible mirrors. The relationship between structural design and mirror dimpling, however, is complex and involves the coupled interactions of numerous design parameters. The optimization routines discussed in Chapter 5 are applied to minimize this dimpling after a standard metric is formulated. The following section focuses on developing a more precise understanding of actuation-induced dimpling and defining such a metric to accurately quantify the dimpling residual.

4.1.1 Simulating mirror dimpling

A standard metric is required to quantify and compare mirror dimpling across a family of mirrors with different sizes and rib geometries, as is done in the trade space optimizations in Chapter 5. This section describes both how to induce the dimpling shape in a deformable mirror and also how to quantify the dimpling residual.

Induced-focus residual

Dimpling specifically refers to the high order shape that is periodic with the spacing of the embedded actuators. Actuation-induced residual, and hence dimpling, may be induced by any type of low-order shape command. A standard metric requires using a consistent command in all cases. This command ideally is independent of the mirror size, shape, and rib geometry since comparisons must be made across changes in such parameters. One command that qualifies, and is a typical command in practice, is an induced-focus. Inducing focus on a mirror segment is analogous to actuating a corresponding change in radius of curvature.

Inducing focus on a deformable mirror is typical in practice because of two common optical assembly errors in space telescopes. The first is error in the desired mirror prescription resulting from the manufacturing process. Besides print-through effects (discussed in Section 3.2.1), errors from the manufacturing process are typically smooth, low order shapes across the mirror diameter. Focus error is a common example of one of these manufacturing-related, long spatial wavelength errors. The second example of a common error source is misalignment of the optical elements in the telescope assembly. A perfectly prescribed and manufactured primary mirror still produces a poor image if it is not aligned as designed. The misalignment produces a piston error if it occurs along the optical axis of the telescope.

Both of these error sources produce a pure defocus of the final image. Both, however, are correctable if the primary mirror can accurately change its level of focus. Hence, a deformable mirror control system can mitigate common manufacturing and assembly errors by accurately adjusting the level of focus. When inducing focus, the *induced-focus residual* is the difference between the resulting shape and the desired pure focus shape. The induced focus residual is calculated as follows. The desired focus shape is first defined as the set of surface node z-displacements, $\bar{f}$, such that:

$$f_i = f'(2\rho_i^2 - 1), \qquad \forall i \in 1...N_{nodes} \tag{4.1}$$

where f' is a scale factor, ρ_i is the radial coordinate of the i^{th} surface node, and N_{nodes} is the number of facesheet surface nodes in the finite element model. The required set of actuator commands, $\bar{u}^*$, to produce the desired focus shape is then calculated as:

$$\Sigma\bar{u} = \bar{f} \tag{4.2a}$$

$$\bar{u}^* = (\Sigma^T\Sigma)^{-1}\Sigma^T\bar{f} \tag{4.2b}$$

where Σ represents the influence function matrix. Finally, the residual $\bar{r}$ between the resulting shape and the desired shape command is calculated as:

$$\bar{r} = \Sigma\bar{u}^* - \bar{f} \tag{4.3}$$

This dimpling residual is deemed uncorrectable because of its short spatial wavelength. The spatial frequency of the residual is on the order of one cycle per actuator spacing and is thus uncorrectable since two actuators are required per error cycle for reliable correction [5].

Radius of curvature conversion

Changing the mirror radius of curvature is a standard industry practice and, as a result, it provides a sound approach to compare to industry results. As such, a 1mm ΔRoC is used as the standardized low-order shape control command in order to induce the high spatial frequency dimpling effect. Converting from radius-of-curvature to focus allows Equation 4.2 to be solved in terms of the ΔRoC command. For parabolic surfaces, the conic equation

[5] gives:

$$z_{parabolic,i} = \frac{\rho_i^2}{2\,RoC}, \qquad \forall i \in 1 ... N_{nodes} \tag{4.4}$$

whereas a pure focus shape from the Zernike series ($\zeta_4 = 1,\ \zeta_i = 0\ :\ \forall\, i \neq 4$) is defined as the set $\bar{z}_{focus}$ such that:

$$z_{focus,i} = f_i|_{f'=1} = 2\rho_i^2 - 1, \qquad \forall i \in 1 ... N_{nodes} \tag{4.5}$$

By curve fitting data, the following conversion is obtained between the radius of curvature at a parabolic vertex and the level of focus as defined by the Zernike expression:

$$f_1 = 0.0848\,RoC^{-1.0094} \tag{4.6}$$

The required change in focus is thus readily obtained via Equation 4.6 for any desired radius of curvature change.

4.1.2 Quantifying mirror dimpling

The first step in measuring the amount of dimpling produced by a mirror is to induce the dimpling shape using a standardized shape command (i.e. 1mm ΔRoC). The second step is to quantify the residual shape using a scalar metric, which can be done using either a Zernike filter method or a direct difference method.

Zernike filter method

One option to quantify the amount of dimpling produced by a given mirror design involves examining the Zernike signature of the induced focus shape. Appendix B contains an overview of the Zernike polynomials. In short, the Zernike shapes belong to an infinite series of polynomials in polar coordinates that are orthogonal over the unit circle. They are common in the optics community since many optical components are circular and because many optical aberrations take the form of low-order Zernikes such as focus, coma, and astigmatism.

As orthogonal polynomials, the Zernike series serves as a convenient basis for two-dimensional shape decomposition. For any set of facesheet surface displacements $\bar{z}$ (whose

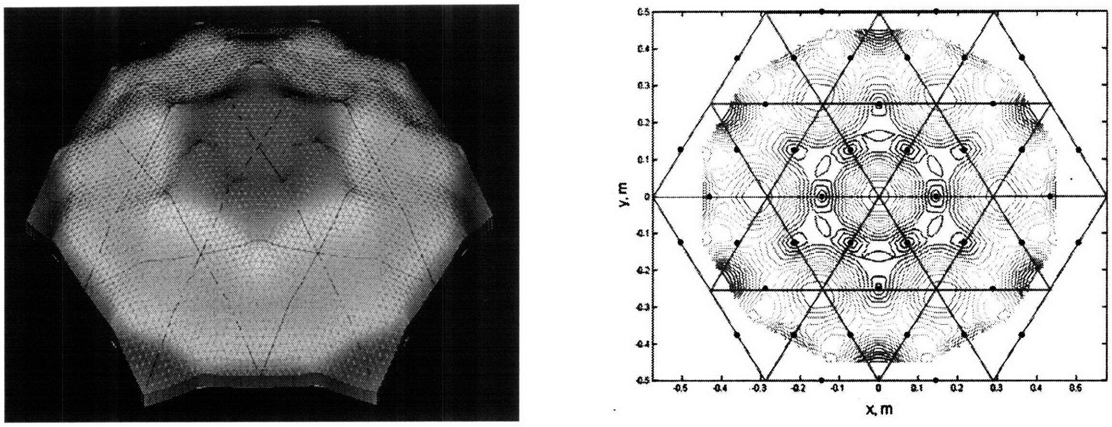

(a) (b)

Figure 4-3: Induced focus deformation, (a) profile view, and (b) associated contour plot (focus removed)

locations are defined in polar coordinates), the set of Zernike coefficients, $\bar{\zeta}$, is calculated via Equation 4.7.

$$\bar{\zeta} = A_{r,\theta}^{-1}\,\bar{z} \tag{4.7}$$

where $A_{r,\theta}$ represents the mapping matrix for Zernike polynomials in polar coordinates (up to the desired number of coefficients). The set of Zernike coefficients (herein displayed in bar graph form) is referred to as the *Zernike decomposition* for any given set of surface displacements, $\bar{z}$.

The purpose of using a Zernike filter to quantify dimpling is to isolate particular high-order shapes within the overall aberration and to filter low-order shapes that may be present. The first step to develop the Zernike filter approach is to identify the polynomials and respective weights that comprise the representative dimpling pattern. Figure 4-3 shows an image of the mirror deformations under an induced-focus command and a contour plot of the same shape (with the focus term removed for clarity) within the 95% clear aperture of the baseline hexagonal segment. A 95% clear aperture refers to the portion of the facesheet surface that lies within a circle 95% the size (by radius) of the largest possible inscribed circle within the hexagonal segment, and is described in Section 3.5. The locations of the ribs (straight lines) and embedded actuators (dots) are included in Figure 4-3(b) for reference.

The radial and circumferential periodicity of the dimpling pattern is evident in Figure

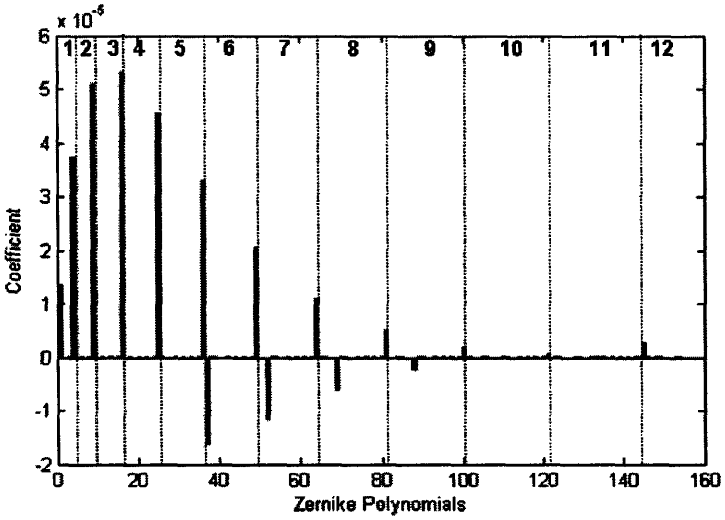

Figure 4-4: Zernike decomposition of dimpling pattern

4-3(b). The dimple peaks predominantly appear at the intersections in the rib backstructure, which are the stiffest locations on the mirror and are the locations farthest from the actuators. Like the backstructure pattern itself, the dimples have both radial and 60° circumferential symmetry. A 156-term Zernike decomposition of this shape reveals these symmetries, and is shown in Figure 4-4. Included for reference are the Zernike polynomial families (see Appendix B for polynomial families n) which are numbered at the top of the figure. The predominant terms in the decomposition are the radial terms (last term in each family) and the 6θ (six-fold circumferential symmetric) terms. The decomposition and the correlation with the symmetries in the mirror show how the dimpling residual is a direct result of the geometry of the rib backstructure.

The second step in the Zernike filter approach is to calculate the scalar dimpling metric by using the inner product of the representative dimpling Zernike coefficients shown in Figure 4-4 (with the commanded focus removed), $\bar{\zeta}^*$, and the Zernike coefficients of a mirror deformation being measured, $\bar{\zeta}$:

$$\text{Zernike filter dimpling metric} = \sqrt{\bar{\zeta}'\,\bar{\zeta}^*} \tag{4.8}$$

This dimpling metric filters the Zernike coefficients in the mirror deformation (in the proper proportions) that produce the representative dimpling pattern. Minimizing this dimpling metric over competing mirror designs equates to selecting a mirror that exhibits the lowest correlation with the dimpling shape shown in Figure 4-3.

This Zernike filter metric has the benefit of isolating the high spatial frequency dimpling pattern, but it also presents a number of drawbacks. First, this metric disregards all low-order aberrations in the deformed mirror shape, regardless of their significance. This is beneficial if only high spatial frequency dimpling is of interest in the optimization routines, however, low-order aberrations may also be prevalent. The design optimizations should also avoid mirrors susceptible to such low-order errors.

The second drawback becomes significant when mirrors with many rib rings are studied. The Zernike spectrum in Figure 4-4 is of the baseline mirror design with two concentric rib rings. Mirror segments with three, four, and possibly five rib rings are also of interest due to their prevalence in industry. Capturing the radial and circumferential periodicity in a dimpling pattern for mirrors with higher density rib backstructure patterns requires an extremely large Zernike bandwidth. Many more than 156 terms would be necessary. A decomposition involving hundreds of terms is computationally taxing, it introduces numerical errors associated with large matrix inversions, and it introduces the likelihood of Nyquist sampling errors.

Direct difference method

A more computationally simple approach to quantifying the high spatial frequency dimpling of an induced-focus shape is a direct difference method which uses the result of Equation 4.3 directly, rather than post-processing the dimpling signature with a Zernike filter. The dimpling metric in this case contains the contributions of not only the predominantly high spatial frequency dimpling errors that appear in the residual shape, but also any low-order aberrations that may also exist. This method does not differentiate between the components of the residual; rather, it quantifies the total residual that appears in the mirror after a ΔRoC shape command.

The metric produced is thus most accurately referred to as the *induced-focus residual*, although the term *dimpling* is herein used interchangeably since the vast majority of the total residual is high spatial frequency dimpling. The induced-focus residual is a scalar metric and is calculated using the following three step process:

1. Induce a change in focus to produce a 1mm ΔRoC.

2. Subtract the desired pure focus shape from the resulting mirror shape.
3. Take the root-mean-square of the resulting shape as the dimpling residual metric.

This direct difference method has the drawback that it includes the small contribution of low-order shapes in the calculation of the dimpling metric and cannot discern between the prevalence of high and low spatial frequency errors. By quantifying the total residual, however, this method provides a more accurate means for reporting the level of error in a deformed mirror in comparison to the Zernike filter metric.

This method presents distinct advantages over the Zernike filter method. First, it is much more computationally simple and does not introduce any numerical difficulties or bandwidth ambiguities when studying mirrors with many hexagonal rib rings. The procedure is more generally applicable since the same three step procedure applies to all mirror designs, regardless of size, shape, or rib geometry.

The second advantage of this direct difference method is that it easily permits a clear aperture calculation so that only mirror surface nodes within a clear aperture of the hexagonal segment are considered in the control algorithm, and hence avoids edge control issues. Moment actuators, those that impart a pure moment to the controlled structure, have difficulty controlling the edge of the mirror facesheet and require force actuators to improve this edge control performance [5]. For simplicity, the same type of embedded actuator is used throughout this thesis, so the clear aperture is often used to avoid such edge control issues. Using the direct difference method, the induced-focus dimpling residual of the baseline mirror shown in Figure 4-3(a) is 91.0nm.

This section provided a summary of the origins of actuation-induced dimpling and the method used to simulate and quantify its effect on a model mirror. The following section defines the second source of high spatial frequency residual: manufacturing-induced print-through.

4.2 Manufacturing-Induced Residual: Print-Through

A second form of high spatial frequency error common to deformable mirrors is print-through, or *quilting*. Print-through originates in the polishing process during manufacturing due to the variable structural rigidity across the polished mirror surface. The stiffest areas

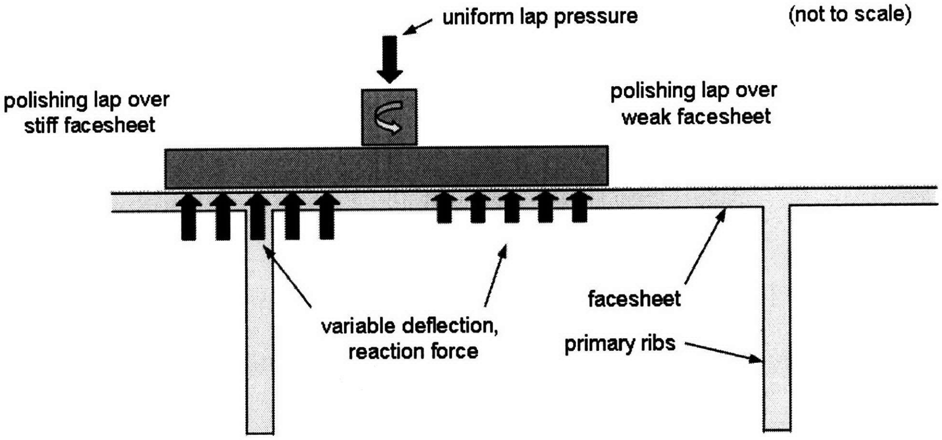

Figure 4-5: Causes of polishing print-through

of the deformable mirror provide the greatest reaction force to the polishing lap, resulting in the greatest wear rate of the surface material by Preston's wear rate equation [28]:

$$\frac{dz}{dt} = -CPv \tag{4.9}$$

where z is the facesheet surface height, P is the polishing lap pressure, v is the polishing rotation rate, and C is a proportional constant.

Conversely, the weakest portions of the mirror (areas of the facesheet not directly supported by ribs) provide the least reaction force to the polishing lap, and result in the lowest wear rate during polishing. The variable polishing wear rates produce a quilting pattern when the polishing process is complete. The print-through effect is difficult to avoid under the assumption that the polishing lap spans at least two ribs since the ribs will supply the bulk of the requisite balancing pressure and, hence, incur the most wear. As a result, variable dwell times, applied pressures, and rotation rates cannot mitigate the residual. Figure 4-5 provides a sketch of how the variable stiffness across the mirror surface produces variable reaction forces and material wear rates, and hence a high spatial frequency residual when the polishing process is complete.

The optimization routines discussed in Chapter 5 are used to optimize the design of the rib backstructure against a high spatial frequency residual metric, which includes the print-through effects. This metric is developed to compare the level of print-through across multiple mirror designs. Calculating this print-through metric involves simulating the pol-

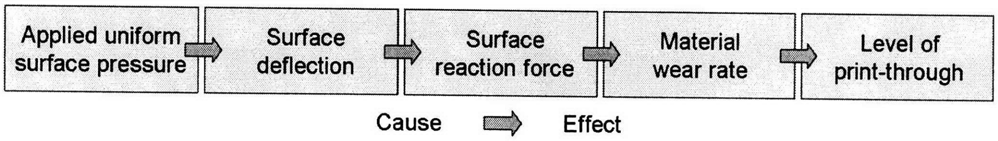

Figure 4-6: Mirror surface polishing relationships

ishing process and quantifying the effect that mirror stiffness has on polishing.

In the case of a mirror polishing process that applies uniform polishing pressure across the mirror surface, the amount of print-through is governed by the material wear rate profile. This profile is a spatially varying function across the mirror surface. The material wear rate is proportional to the mirror reaction force at the mirror surface, which itself is proportional to the local mirror stiffness and inversely proportional to the surface deflection. The local material wear rate, and hence pattern of print-through across the mirror, can therefore be estimated by measuring the local mirror deflection under a constant pressure load. Figure 4-6 summarizes these cause-effect relationships.

The first step to calculate the print-through error metric is to apply a constant pressure load representing a uniform polishing pressure. This is simulated in Nastran using uniform force vectors applied to all mirror surface nodes in the direction parallel to the optical axis. The mirror is constrained at all rib nodes farthest from the facesheet, those that would be adjacent to a rigid support structure while the mirror surface is polished. These nodes are constrained in all three translational degrees of freedom.

The forces just described are applied simultaneously to the mirror surface, even though the polishing lap in an actual process applies pressure to small portions of the mirror at any given point in time. This saves considerable computation time and is possible due to the linearity of the FEM. This superposition assumes that the polishing pressure, dwell time, and lap rotational speed are all constant across the mirror surface.

If the simulation forces are applied in the $+z$-direction (opposite the direction of the actual polishing pressure), the deformation pattern resembles that of the desired simulated print-through deformation that results when the polishing pressure is removed and the most flexible portions of the facesheet spring back. In other words, the deformation pattern exhibits peaks at the weakest mirror locations (where the wear rate is lowest) and valleys at the stiffest mirror locations (where the wear rate is greatest). This directional freedom

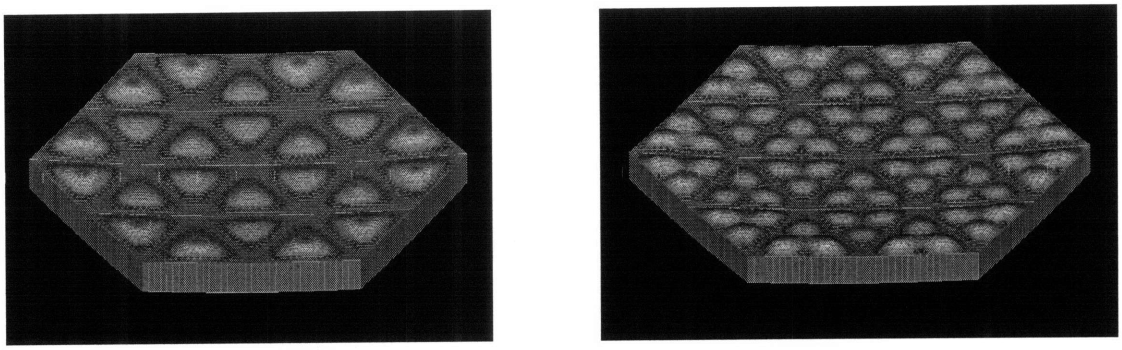

(a) (b)

Figure 4-7: Example simulated print-through deformation pattern (a) without and (b) with cathedral ribs

in the applied force is possible, without loss of accuracy, also because the mirror FEM is linear. An example simulated print-through deformation pattern after the uniform force vectors are applied is shown in Figure 4-7 for mirrors with and without cathedral ribs.

The print-through metric is taken as the RMS of the mirror surface z-displacement vector under the simulated pressure load. This produces a scalar metric useful to compare the relative amounts of print-through between competing mirror architectures. For example, the print-through metric for the baseline mirror under a 225Pa pressure load is 31.4nm. The magnitude of this applied pressure is explained in more detail in Section 5.4.1. A summary of the 3-step process for calculating the print-through metric is as follows:

1. Constrain all rib nodes farthest from the facesheet in all translational DOF.
2. Apply a uniform load to the mirror surface in the reflecting ($+z$) direction.
3. Take the RMS of the resulting surface deformation as the print-through metric.

This section provided a summary of the origins of manufacturing-induced print-through and the method used to simulate and quantify its effect on an appropriately constrained mirror model. The following section defines the third source of high spatial frequency residual: thermally-induced ripple.

4.3 Thermally-Induced Residual: Ripple

The third and final predominant source of high spatial frequency error in lightweight, rib-stiffened mirrors is that due to thermal disturbances, and will be referred to as *thermal* *ripple.* Deformations due to thermal disturbances are common sources of figure error in space telescope mirrors. Any fluctuation in the thermal environment, due to either on-board or spaceborne heat sources, causes the optical assembly to deform according to the geometry and CTE (coefficient of thermal expansion) of each material. The primary mirror is no exception, and is vulnerable to thermal disturbances which translate to figure error and poor image resolution. The active control system is designed to mitigate such disturbances and maintain the desired mirror prescription. However, it is unable to correct for any high spatial frequency disturbances that appear. The following section describes the method of quantifying the level of uncorrectable thermally-induced error.

To calculate a thermal ripple error metric, a 1° bulk temperature change is first applied to the mirror. The high thermal conductivity of many mirror materials ($157 W/m^{\circ}C$ for SiC for instance [2]) allows a thermal disturbance to rapidly spread across the mirror diameter, nearly eliminating thermal gradients and resulting in a uniform, or *bulk*, temperature soak. This bulk soak induces a predominantly focus deformation in the baseline mirror (see Section 3.1) and the resulting (zero mean) deformation, with an RMS of 410nm, is shown in Figure 4-8(a). For this temperature soak, the actuators are removed from the model to avoid issues of CTE mismatch between the actuators and the surrounding silicon carbide and to solely capture the effect of the mirror geometry.

The second step is to isolate the high-order thermal ripple in the deformed shape. This is possible using Matlab's Fast Fourier Transform (*FFT*) commands as a high-pass spatial filter of the mirror surface deformation to remove the low-order, predominantly focus shape. Removing the low-order shapes is necessary because the actuators have the highest control authority over these long spatial wavelength deformations which allows them to be corrected. Also, the ability of the actuators to command a pure focus shape is represented in the dimpling metric discussed in Section 4.1, and the thermal ripple metric is meant to quantify only the high spatial frequency deformations.

The high-order shapes are isolated by filtering all shapes with spatial frequencies below a particular threshold. In this case, "high spatial frequency" refers to all spatial frequencies at or above that of the actuator spacing. The inter-actuator spacing in the baseline mirror design (of actuators on the same rib) is 0.29m. The threshold frequency for the high-pass spatial filter is therefore: $\omega_{th} = 2\pi f_{th} = 2\pi/0.29\text{m} = 21.7$ rad/m. The resulting filtered shape of the mirror surface within a 95% clear aperture is shown in Figure 4-8(b).

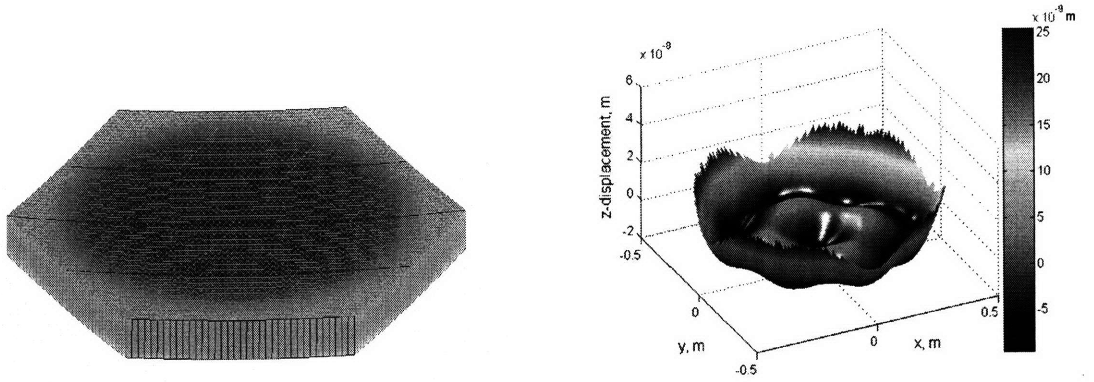

(a) (b)

Figure 4-8: Mirror deformation due to 1°ΔT [C] bulk temperature soak, (a) profile view, and (b) high pass filtered deformation

The final step to generate the thermal ripple error metric is to take the RMS of the spatially filtered shape. For the baseline mirror under a 1°ΔT [C] thermal soak, the RMS of this (zero mean) filtered shape is 7.3nm. In summary, the thermal ripple error metric is calculated as follows:

1. Induce a 1° bulk temperature change in the mirror.
2. Spatially filter all shapes in the resulting deformation with frequencies that lie below the spatial frequency of the actuator spacing.
3. Take the RMS of the filtered shape as the thermal ripple error metric.

In comparison to the dimpling surface RMS described in Section 4.1, however, the 7.3nm residual for a 1° ΔT [C] soak is small relative to the 91.0nm dimpling error of the baseline mirror design. By linearity, a bulk temperature change of 12.5° is required for the thermal ripple error to equal that of a 1mm ΔRoC induced-focus dimpling error. However, as a greater bulk temperature disturbance is introduced, a greater dimpling error is also introduced since the actuators must correct for the low-order aberration. As a result, the thermal ripple error is disregarded in the design optimizations in Chapter 5. The optimizations instead focus on mitigating dimpling and print-through.

4.4 Summary

This chapter discussed the three predominant high spatial frequency error sources for lightweight, deformable mirrors: actuation-induced dimpling, manufacturing-induced print-through, and thermally-induced ripple. The step-by-step methods for simulating these error sources and for quantifying the amount of error due to each source was discussed. Table 4.1 summarizes the three error sources, the perturbations used to simulate each effect, and the amount of surface RMS each produces on the baseline mirror design.

Table 4.1: Summary of high spatial frequency error metrics

Residual	Perturbation	Surface Error (RMS)
Actuation-Induced Dimpling	1mm ΔRoC	91.0nm
Manufacturing-Induced Print-through	225Pa surface pressure	31.4nm
Thermally-Induced Ripple	1° ΔT [C] soak	7.3nm

The resulting surface RMS values show how dimpling and print-through are the major sources of high spatial frequency residual assuming that the chosen perturbations are indicative of an actual manufacturing and operating environment. The objective function discussion in Section 5.3 explains how these two error sources are treated in the mirror optimization routines and how the applied surface pressure for the print-through simulation is used to calibrate the balance between dimpling and print-through in the objective function.

Chapter 5

Mirror Structural Design Optimization and Results

This chapter details the motivation and methods for optimizing the structural design of a deformable mirror. Candidate methods for rapidly exploring a trade space are presented. Preliminary single axis trades are then used to narrow the focus of the overall optimization and to help identify key design parameters. An example trade space (over facesheet mass fraction and rib aspect ratio) and the developed structural design heuristics are presented. This example is representative of the complete set of trade space results (for all combinations of independent design variables) contained in Appendix A.

5.1 Motivation

The embedded actuator shape control systems employed today have been shown to be highly effective at mitigating many quasi-static global shape errors [23]. However, the rib-stiffened design and discrete nature of the control systems introduce the concept of uncontrollable, high spatial frequency surface error. This residual is uncontrollable because its spatial frequencies lie above that of the actuator spacing on the mirror backstructure. As a result, the actuators have no significant control authority over these shapes [5].

Chapter 4 detailed the origins of the two major components of high spatial frequency surface residual: actuation-induced dimpling and manufacturing-induced print-through. A given mirror, due to its structural design and manufacturing process, can be plagued by any combination of these error sources. Improving the correctability of these actively controlled mirrors requires understanding these error sources and designing mirrors to mitigate the uncorrectable error to the greatest extent.

Conventional design heuristics, however, cannot capture the complex coupling of the design parameters of deformable mirrors in terms of the chosen performance metrics. As discussed in Chapter 2, these design techniques often employ basic structural principles for deflection models to create tradeoff charts for a given rib geometry. Additionally, since these techniques employ purely structural principles, they do not consider actuation-induced error which results from the coupling of the actuator and the surrounding structure.

The parametric modeling capability of the MOST modeling tool presents the opportunity to more fully understand the structural behavior of the intricate designs necessary for high performance mirrors. The high spatial frequency, uncorrectable error can be minimized by optimizing the mirror design over selected structural parameters, thereby improving the correction limit of the shape control system. The parametric capability of MOST is utilized to provide insight into the optimal structural design relationships of a deformable mirror that conventional design heuristics cannot capture. This is done by both capturing the effects of all structural parameters (via a high fidelity FEM) and by quantifying the actuation-induced error (via mirror shape control simulations).

5.2 Methods for Trade Space Exploration

The complete trade space in this study involves several structural design variables which are detailed in Section 5.4.3. Full factorial contour plots (showing the value of the objective function discussed in Section 5.3) are included in Appendix A to develop insight into the behavior of the trade space. However, more efficient search methods facilitate supplementary optimizations and make for more rapid sensitivity analyses (discussed in Sections 5.4.1 and 5.4.2).

For demonstrative purposes, suppose a full factorial search of the five-dimensional trade space is conducted using the step size discretizations summarized in Table 5.3. The total number of mirror designs to consider is the product of the number of discretizations used for each variable, or 7,344 unique designs, and each point design requires obtaining all influence functions. For a mirror with 42 actuators, and assuming each influence function requires 45 seconds to compute, the full factorial search requires nearly 4,000 hours of computation.

Efficient trade space exploration techniques are clearly necessary for rapid trade space searches and to study the effect of any additional variables without factorially increasing the computational complexity. Exploring the trade space more efficiently also requires more rapid point design evaluations. The following sections describe methods toward both ends.

5.2.1 Survey of exploration methods

A variety of trade space exploration techniques are available. A brief survey of candidate methods follows for completeness ([22], [34]). In this list, s represents the number of steps for each design variable, and n represents the number of design variables of interest. Also, the objective function refers to that described in Equation 5.1 in Section 5.3 which quantifies the total high spatial frequency mirror surface residual.

Full-factorial search This method evaluates designs at every unique combination of design variables. The search is exhaustive and accurate, but the high computational expense makes this technique impractical for many applications. Complexity grows exponentially with the number of design variables. Computational complexity: high, $O(s^n)$.

Uni-variate search This method varies one design variable across its allowable range while holding all other variables constant. The process is repeated for each variable in succession while all other variables are held to their baseline values. Each search produces an optimum design along the one-dimensional cut. The combination of these one-dimensional optima form the subsequent design vector, and this process is repeated until convergence. This method provides a good feel for the trade space, but is not guaranteed to produce a global optimum and does not capture coupling relationships between variables. Computational complexity: moderate, $O(sn)$.

Taguchi methods (orthogonal arrays) These methods explore a particular subset of the possible full-factorial combinations for a more efficient but less exhaustive approach. Each design vector that is evaluated is orthogonal to every other design vector, so these methods do not fully capture interactions of design variables and are hence not always effective. Computational complexity: moderate, $O(sn)$.

Latin hypercubes Each variable is assigned an identical number of discretization steps,

s, within each allowable range and the design vectors are chosen randomly such that each value of each variable is used only once in all s vectors. This technique has poor coverage of the trade space, limits the discretization of the design variables, is not guaranteed to converge, but is very efficient. Computational complexity: low, $O(s)$.

Simulated annealing This method mimics the cooling process of a material to a minimized state of energy by avoiding converging to a sub-optimal solution too quickly. Simulated annealing conducts a random walk through the trade space from an initial design vector, accepting more optimal neighboring designs more frequently as the simulation "cools." The simulated cooling process avoids local minima by accepting less optimal solutions with a controlled probability, but is not guaranteed to find the global optimum. This method is most applicable for poorly behaved cost functions, but it is guaranteed to converge for convex cost functions. The complexity depends on the shape of the cost function and the proximity of the initial design vector to the global optimum. Computational complexity: moderate, $O(sn)$.

Gradient search Similar to simulated annealing, gradient descent conducts a "downhill" walk through the trade space from an initial design vector by perturbing the vector sequentially for all variables and updating only in the direction of steepest descent. Each iteration decreases the cost function until an optimal solution is found. This technique is guaranteed to converge for convex cost functions, although it can be highly susceptible to local minima with non-convex cost functions. Complexity depends on the shape of the cost function and the proximity of the initial design vector to the global optimum. Computational complexity: moderate, $O(sn)$.

Gradient descent provides a balance between computational complexity and accuracy. As a result, a gradient search technique is used throughout this thesis for all supplementary trade space optimizations. For a given trajectory through a trade space, the number of perturbations (i.e. model simulations and function evaluations) required for gradient descent is proportional to the number of variable design parameters and to the number of discretizations, making the approach $O(sn)$ in complexity. Although the complexity of gradient descent is higher than that of some methods, the guarantee of convergence that it offers (for convex cost functions) makes the technique valuable.

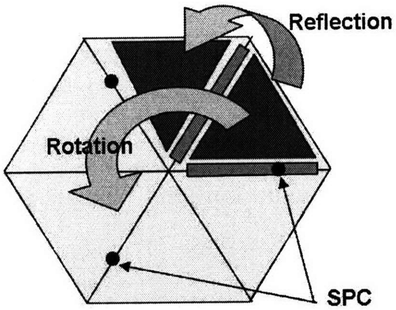

Figure 5-1: Reflective and rotational symmetries exploited through influence function mapping

Unlike some competing techniques, the gradient descent algorithm is very flexible to changes in step size discretization for progressively refining a trade space search. Using smaller step sizes in succession allows the approach to converge to the global optimum with increasingly higher fidelity. There are also no specifications on the number of discretizations for each variable: each dimension may be discretized with as many steps as needed. In addition to using an efficient and reliable exploration technique, the following section describes how it is also possible to accelerate each mirror simulation process.

5.2.2 Influence function mapping

The mirrors used in this thesis are constrained by three points which align with three of the radial spokes in the rib backstructure pattern. As such, there exists a 120° rotational symmetry in the location and orientation of the actuators. This can be exploited for each mirror model by copying and rotating the appropriate influence functions rather than recalculating each from scratch.

There also exists a 120° reflective symmetry with respect to the locations of the point constraints, so appropriate influence functions can also be copied and reflected to save computation time. The symmetries and the influence function mapping procedure are pictured in Figure 5-1 for clarity.

The combination of these symmetries in the mirror geometry allows considerable computational savings during the optimization process. Although all influence functions must be known to evaluate each mirror structural point design, roughly only one sixth are calculated for each architecture.

5.3 Mirror Design Objective Function

The objective function used for the following mirror design optimizations weighs the ability of each mirror to mitigate high spatial frequency surface error. The objective function considers the effects of both surface dimpling and print-through, and treats these as independent variables via a root-sum-square (RSS) [7] since they are believed to have weakly correlated effects on the mirror (in terms of the shapes of the error patterns). The mirror structural design is optimized for one that produces the least RSS high spatial frequency residual by using the following objective function:

$$\text{Objective Function } = \sqrt{\left(RMS^2_{\text{dimpling}} + RMS^2_{\text{print-through}}\right)} \tag{5.1}$$

However, the amplitudes of the dimpling and print-through contributions to the objective function are ambiguous since the magnitudes of the simulation inputs (1mm ΔRoC and a uniform applied pressure, respectively) are arbitrary. The relative amounts of dimpling and print-through are dependent on the demands of the mirror manufacturer because the ΔRoC requirements and the polishing processes vary. For instance, one user may require substantial ΔRoC performance (or may employ a surface finishing technique such as ion-figuring [17]) making print-through negligible in comparison to dimpling, whereas another user may employ an extremely harsh polishing process that makes the dimpling residual negligible to that of print-through.

Due to this ambiguity, the relative amount of dimpling and print-through is treated as a variable parameter through a prescribed *dimpling-to-print-through ratio.* This ratio calibrates the objective function and specifies the approximate balance between its two components. The ratio is used to determine the optimal cathedral mass fraction, which is a design variable with a strong influence on both dimpling and print-through effects. The method for selecting appropriate cathedral mass fractions as a function of the dimpling-to-print-through ratio is discussed in more detail in Section 5.4.1.

5.4 Results

This section presents the optimization results for a variety of cases. First, several single-axis trades are presented. These serve as sensitivity analyses to identify the most sensitive design variables, and the results help narrow the list of variables in the overall trade space. Next, the results for a number of supplementary trades are presented. These trades are conducted over mirror design parameters that are otherwise held fixed. The results of these trades are meant to convey the effects of variability in each parameter should it become available via manufacturing technology. Lastly, the results of an example trade space search are presented. This example is representative of the complete set of results contained in Appendix A, and the associated discussion details how the results of the trade space are interpreted.

5.4.1 Single axis trades

The coupling relationships between many of the mirror design variables are complex, and concisely representing all relationships is a difficult task. The first step in exploring the mirror trade space across these variables, however, is to explore along individual design axes in sequence to shed light on the sensitivity of the optimization results to each variable. These single axis trades also serve to narrow the focus of the overall multi-variable trade space to the most interesting variable regimes, and to avoid those with little parameter cross-coupling. They serve as sensitivity analyses to ascertain which design variables are the most influential on the optimization results.

Areal density

The first single axis trade is that of areal density, a design parameter that is typically specified by the performance requirements of a given project. This trade is conducted for areal densities from 5kg/m^2 to 15kg/m^2 and the resulting optimality trends for optimal facesheet mass fractions, optimal cathedral mass fractions, and resulting total surface residuals (i.e. values of the objective function) are shown in Figure 5-2. In other words, for each value of areal density, the values of facesheet and cathedral mass fractions are found that minimize the total high spatial frequency residual. All other design parameters are held at their baseline values (defined in Section 3.1). Each result corresponds to a solution for a 225Pa applied surface pressure for the print-through simulation (discussed in more detail later in this section). This limitation fixes the relative amounts of dimpling and print-through.

Figure 5-2(a) shows that the optimal design has a high sensitivity to changes in areal density. The optimal mass fractions for 5kg/m^2, for instance, are significantly different

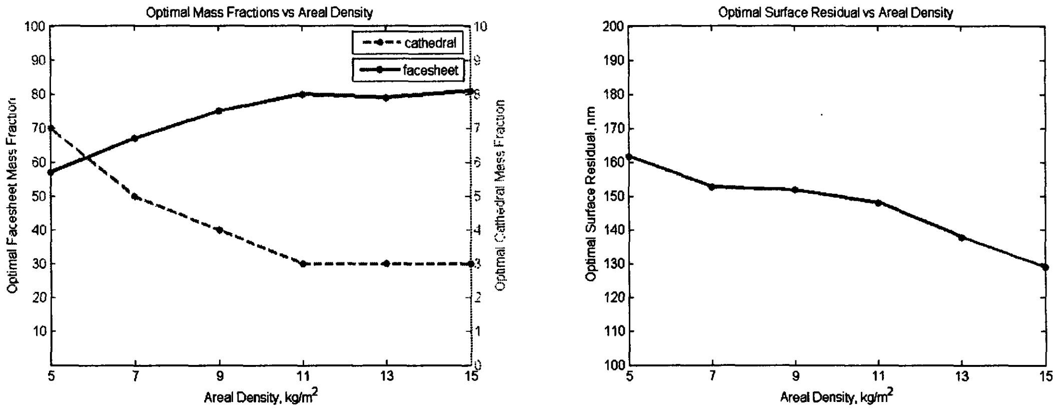

(a) (b)

Figure 5-2: Sensitivity of optimization results to changes in areal density for (a) optimal mass fractions and (b) total surface residual

from the optimal mass fractions for 15kg/m^2. The effect of lightweighting can be seen in Figure 5-2(b) since the heavist mirrors mitigate roughly 20% more high spatial frequency residual in comparison to the lightest mirrors. Because of this high sensitivity, areal density is treated as an independent variable in the optimization trade space.

F-number

A second single axis trade is conducted to measure the sensitivity of the optimal mirror design to changes in f-number. This trade is conducted for f-numbers of 1, 5, and 10 and the results for the optimal mass fractions and optimal total surface residual are shown in Figure 5-3. All other design parameters are held at their baseline values during these optimizations. As in the areal density trade in the previous section, the applied surface pressure for the print-through simulation (discussed in Section 5.4.1) is 225Pa.

Figure 5-3(a) shows that the optimal facesheet and cathedral mass fractions have only a marginal sensitivity to large changes in f-number. The optimal facesheet mass fraction for $f/1$, for instance, is 81% whereas the optimal mass fraction for $f/10$ is 88%. Furthermore, the curve in Figure 5-3(a) indicates that the change in optimal facesheet mass fraction over the range $f/1$ - $f/3$, a common range for primary mirror f-numbers, is roughly only 3%. The low sensitivity to changes in f-number is also observed in the cathedral mass fraction, which varies less than 0.5% over the $f/1$ - $f/10$ range.

Although Figure 5-3(b) shows a large change in optimal total surface residual for changes

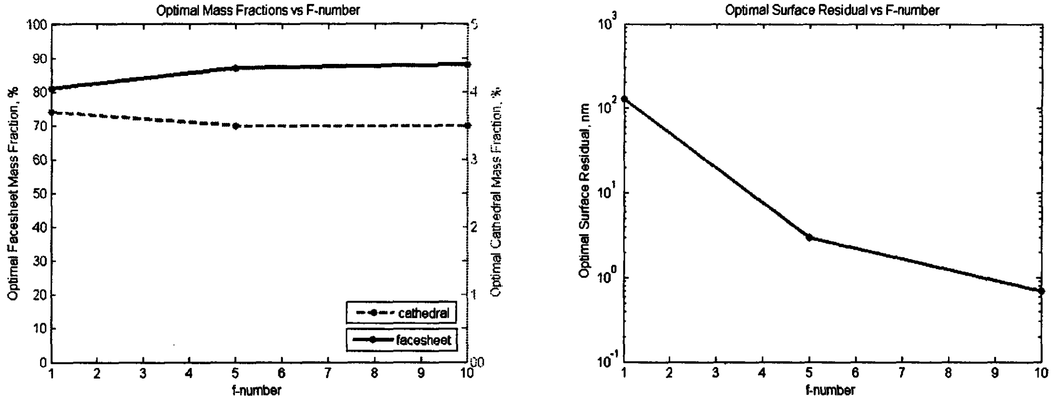

(a) (b)

Figure 5-3: Sensitivity of optimization results to changes in f-number for (a) optimal mass fractions and (b) total surface residual

in f-number, this change is attributable to the standard 1mm ΔRoC maneuver used to induce dimpling (see Section 4.1), and not necessarily directly attributable to the change in f-number. The amount of curvature change necessary to produce 1mm ΔRoC is significantly lower on higher f-number mirrors (per Equation 4.6 for higher RoC), so the amount of dimpling measured is also significantly lower. Using a standard ΔRoC command to induce dimpling makes it difficult to compare total dimpling residual across changes in f-number.

Although low f-number mirrors ($\sim f/1$) are known to pose many manufacturing (i.e. polishing of a highly curved surface) and optical performance difficulties, the optimal mirror design results are shown to exhibit little variability across a large range of primary mirror f-number. As a result, the optimal mirror design relationships for $f/1$ are assumed to be applicable for mirror designs at higher f-numbers. The f-number is thus fixed at $f/1$ for the majority of the mirror optimization routines. Appendix A contains optimization results for selected f-numbers other than $f/1$ to better show the low sensitivity in the results to changes in f-number.

Dimpling-to-print-through ratio

The cathedral mass fraction has a strong influence on both components of the optimization objective function (dimpling and print-through residuals). Figure 5-4 shows the sensitivity of the optimal dimpling and corresponding print-through residual to changes in cathedral mass fraction for the baseline mirror design. The optimal dimpling residuals in Figure

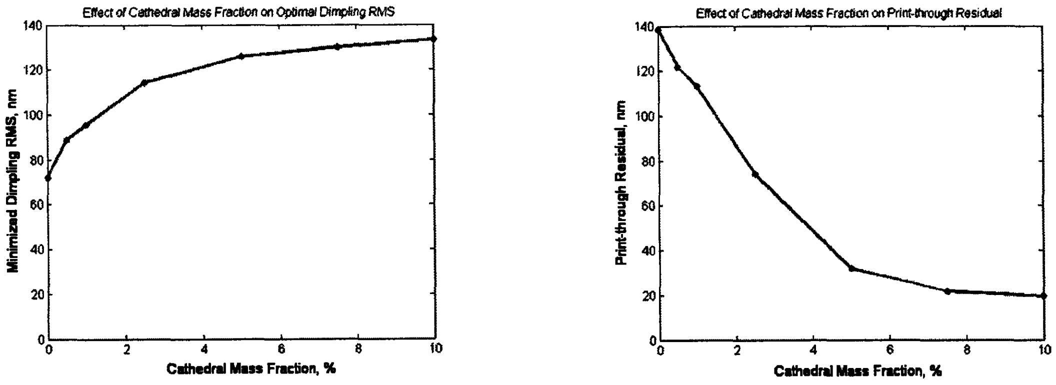

(a)

(b)

Figure 5-4: Sensitivity in optimization results to changes in cathedral mass fraction for (a) minimized dimpling, and (b) corresponding print-through residual

5-4(a) are determined by optimizing over facesheet mass fraction and primary rib aspect ratio for each level of cathedral mass fraction. The corresponding print-through residuals for each of these dimpling-minimized designs are shown in Figure 5-4(b).

Note how both the optimal amount of dimpling and corresponding level of print-through are highly sensitive to the cathedral rib mass allocation. The shapes of the curves indicate that the two components of the objective function are inversely related through the cathedral mass fraction. The dimpling residual is consistently improved by decreasing cathedral mass, whereas the print-through residual is consistently improved by increasing cathedral mass.

These opposing trends indicate that a careful approach is required to consider dimpling and print-through in the same objective function. The optimization routines must balance the effects of dimpling and print-through since both residuals are known to exist in lightweight mirrors. The *dimpling-to-print-through ratio* is used as an independent variable to tie the two residual components together. For a given areal density, the surface pressure used in the print-through simulation (as described in Section 4.2) is scaled such that the dimpling and print-through residuals have relative amplitudes that correspond to a particular *dimpling-to-print-through ratio* (calibrated using the baseline mirror design).

For instance, a surface pressure of approximately 225Pa produces roughly 30nm of print-through residual and 1mm ΔRoC produces roughly 90nm of surface dimpling on the baseline mirror, resulting in a 3:1 dimpling-to-print-through ratio. The mirror design can then be optimized over facesheet and cathedral mass fractions using this 225Pa applied surface

Table 5.1: Applied pressures (Pa) used to simulate print-through for various dimpling-to-print-through ratios and areal densities

Areal density (kg/m^2)		5	10	15
Dimpling to print-through ratio	0.1	339.2	2480.4	6798.6
	1	33.9	248.0	679.9
	3	11.3	82.7	226.6
	10	3.4	24.8	68.0
	100	0.3	2.5	6.8

pressure to simulate print-through. Table 5.1 summarizes the applied pressures used to simulate print-through for various dimpling-to-print-through ratios and areal densities. Alternatively, polishing pressure could be held constant and ΔRoC varied to achieve the same dimpling-to-print-through ratio. The optimization results would be the same due to model linearity. Using a standard 1mm ΔRoC, however, provides a means to compare to industry, whereas the polishing pressure used in the print-through simulation is only an arbitrary simulation quantity.

Figure 5-5 shows both the optimal facesheet and cathedral mass fractions for various dimpling-to-print-through ratios for the baseline mirror. The trend in optimal cathedral mass allocation is intuitive. Ratios near zero (on the horizontal axis) indicate negligible dimpling in comparison to a large amount of print-through, or *print-through dominated* situations. The optimized rib structure is as spatially homogeneous as possible (to minimize deflection due to uniform surface pressure) with roughly equal mass allocations for cathedral and primary ribs (i.e. 10% cathedral, 11% primary ribs). Dimpling-to-print-through ratios between 1 and 4 correspond to a transition region where a cathedral mass fraction between 2% and 6% mitigates a balance of print-through and dimpling.

Lastly, the effect of print-through becomes negligible compared to that of dimpling for ratios at or above five, and the optimal design features no cathedral ribs. In this case, the optimal cathedral mass allocation reaches 0% for the highest dimpling-to-print-through ratios, or the *dimpling dominated* situations. Table 5.2 summarizes the complete set of optimal cathedral mass fractions for all combinations of areal density and dimpling-to-print-through ratio. It is, in other words, the *test matrix* for the complete set of trade space results in Appendix A, showing the cathedral mass fraction for all 15 cases (for $f/1$) that are presented.

This process allows the user to select the most applicable optimization results using

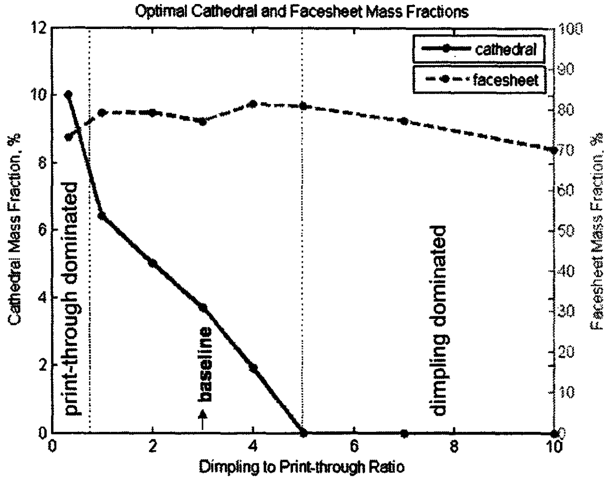

Figure 5-5: Optimal mass fractions for various dimpling-to-print-through ratios

Table 5.2: Optimal cathedral mass fractions (%) for combinations of areal density, and dimpling-to-print-through ratio (test matrix)

Areal density (kg/m^2)		5	10	15
Dimpling to print-through ratio	0.1	9	11	10
	1	6	6	6
	3	3	3	3
	10	0	0	0
	100	0	0	0

either an approximate dimpling-to-print-through ratio or the desired cathedral mass fraction. This range is included due to the wide range of polishing processes (which affect print-through) and ΔRoC requirements (which affect dimpling). Section 5.4.3 presents the trade space for the baseline mirror (15 kg/m^2 areal density, 3:1 dimpling-to-print-through ratio) for varying facesheet mass fraction and rib aspect ratio. The results for all other combinations of independent variables are contained in Appendix A.

5.4.2 Supplementary trades

Several supplementary optimizations concerning the design of the rib-stiffened mirror structure and associated control system are also possible. These optimizations show the effect of changes in the design of the baseline mirror and control system specified throughout this thesis. In some cases, the variability of these additional design parameters is limited by manufacturing or material technology. The results presented are thus meant to reflect the benefit of increased flexibility in certain design parameters should such flexibility become available. The variables studied in this section are treated as fixed elsewhere.

Actuator length

The first supplementary optimization is that of actuator length. Short actuators (relative to the mirror diameter and rib cell size) produce nearly pure moments in the mirror structure and command very localized changes in mirror surface curvature. This argument suggests by contrast that longer actuators have the authority to command smoother, more global shapes. The following analysis dictates the degree to which this is true.

Beam theory is first used to provide insight derived from physics fundamentals. A simply supported beam with stiffness properties EI and length L represents one primary rib section of the mirror backstructure and is shown in Figure 5-6 with the corresponding free body diagram. A surface-parallel embedded actuator centered on the edge of the rib is represented by two applied moments in the free body diagram which are aligned with the endpoints of the actuators. Each moment is applied a distance a from the nearest end of the beam. The two moments form a couple, each with magnitude M and of opposite direction.

The moment-curvature relation for simple beams yields the following deflection pattern for the vertical deflection $u(x)$ of the simply supported beam.

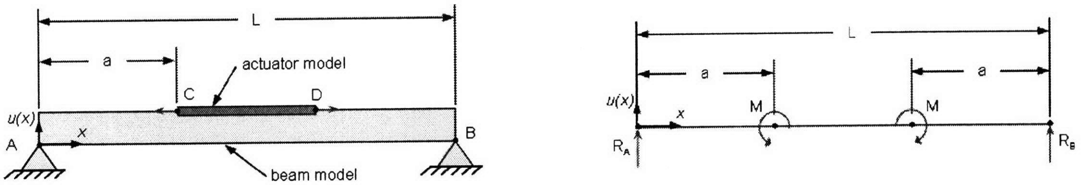

(a) (b)

Figure 5-6: Simple beam analogy for surface-parallel actuator; (a) beam and actuator model, and (b) free body diagram

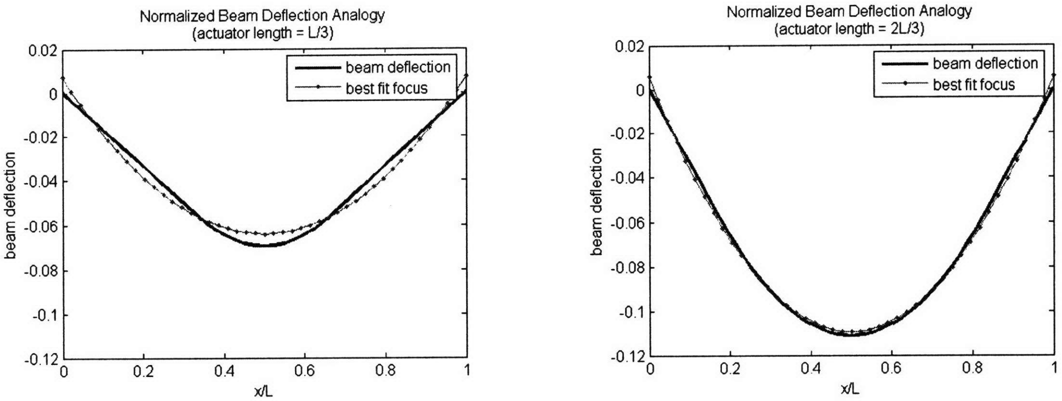

(a) (b)

Figure 5-7: Beam deflection analogy for different actuator lengths, (a) short actuator (L/3), and (b) long actuator (2L/3)

$$EI\,u(x) = \begin{cases} c_1 x, & 0 \le x \le a \\ \frac{M}{2}x^2 + c_2 x + c_4, & a \le x \le L-a \\ c_3 x + c_5, & L-a \le x \le L \end{cases} \tag{5.2}$$

where x is measured from the leftmost end of the beam. The constants of integration are as follows:

$$\begin{array}{llllll} c_1 = & M\left(a - \frac{L}{2}\right) & c_3 = & M\left(\frac{L}{2} - a\right) & c_5 = & -M\left(\frac{L^2}{2} - aL\right) \\ c_2 = & -\frac{ML}{2} & c_4 = & \frac{M}{2}a^2 & & \end{array} \tag{5.3}$$

These results are used to model a rib section deflecting via the influence of actuators of lengths $L/3$ and $2L/3$. Parameters are normalized in this analogy for simplicity: $M = EI = 1$, and the resulting beam deflections are shown in Figure 5-7 for both cases. A best fit parabola (i.e. focus) is shown for reference.

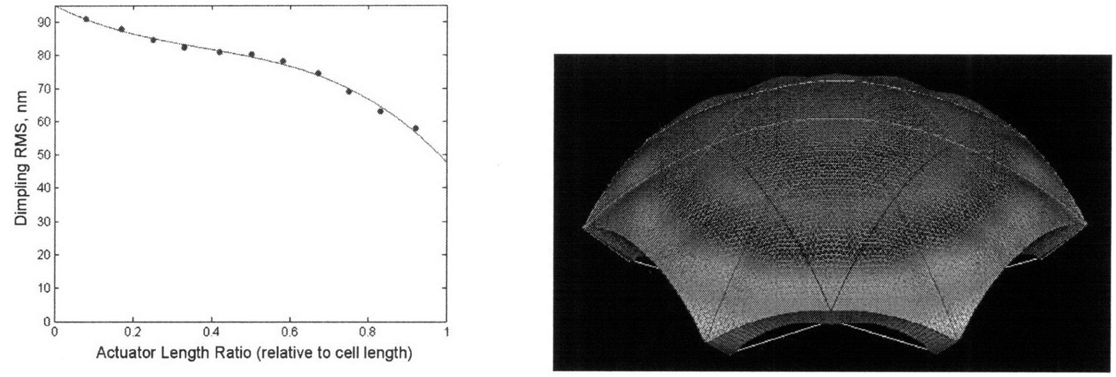

(a) (b)

Figure 5-8: Effect of actuator length; (a) dimpling surface RMS as a function of actuator length ratio, and (b) induced focus shape with long actuators

This simple beam analogy shows how longer actuators are better able to deflect a corresponding rib section into a smooth focus shape, whereas shorter actuators produce a sharper deflection pattern. This analogy neglects the intricacies of complex rib structures and simplifies the effects of the actuators to be pure applied moments, but the conceptual results are applicable to discretely actuated mirrors. The data is also consistent with surface dimpling results obtained from a full mirror model. Figure 5-8(a) shows the results for the amount of dimpling produced for varying actuator length when the actuators command a 1mm ΔRoC. For generality, the actuator lengths are given as a ratio to the length of each rib cell. For reference, the smooth 1mm ΔRoC shape using very long actuators (92% of rib cell length) is shown in Figure 5-8(b). These results show that very long embedded actuators can command a pure focus shape roughly 33% better than very short actuators can. The improved focus performance of longer actuators must be balanced against the decrease in their ability to command short spatial wavelength shapes, which requires further study.

Primary rib taper ratio

The free edges of a mirror do not experience stress due to bending, and therefore do not increase the mirror stiffness. This suggests that a tapered primary rib mass distribution, which concentrates rib mass away from the free edges, may be beneficial for the structural properties of the mirror, such as its rigidity.

This notion motivates a supplementary trade for rib taper ratio against mirror rigidity. The primary rib taper ratio is defined as the ratio of the height of the ribs at the mirror

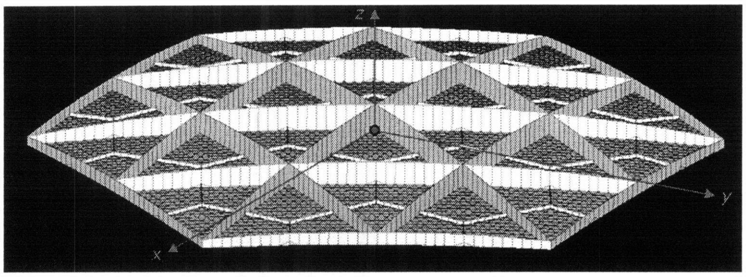

Figure 5-9: Sample MOST mirror realization showing tapered primary ribs

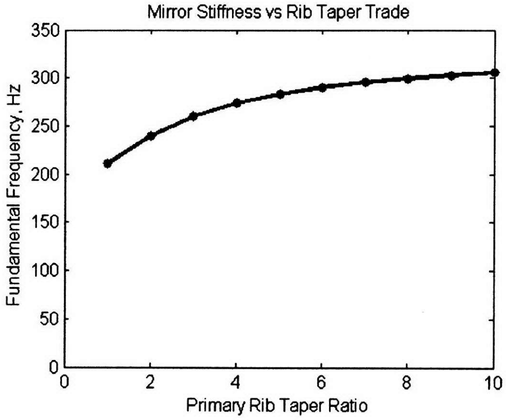

Figure 5-10: Effect of primary rib taper ratio on fundamental mirror bending frequency

center to the rib height at each of the six vertices. The MOST model tapers the primary ribs parabolically along the mirror radius holding the areal density and average rib aspect ratio constant. A sample MOST realization showing the parabolic primary rib taper is shown in Figure 5-9.

A trade is conducted for the rigidity of the baseline mirror segment across varying primary rib taper ratios, and the results for the fundamental bending frequency of the mirror are shown in Figure 5-10. Total mirror mass and mass fractions are held constant across all taper ratios. The mirror used for this study has the baseline design parameters, but with a 70% facesheet mass fraction and 2mm rib thickness. These changes limit the height of the primary ribs to ensure that the first bending mode is that of the entire mirror, and not a “flapping” mode of the tall ribs.

These results show that increases in primary rib taper ratio steadily increase the stiffness of the structure. This suggests that rib taper can be used to provide additional stiffness without changing the total mass of the system. The effects of rib taper on other performance requirements, however, must also be considered.

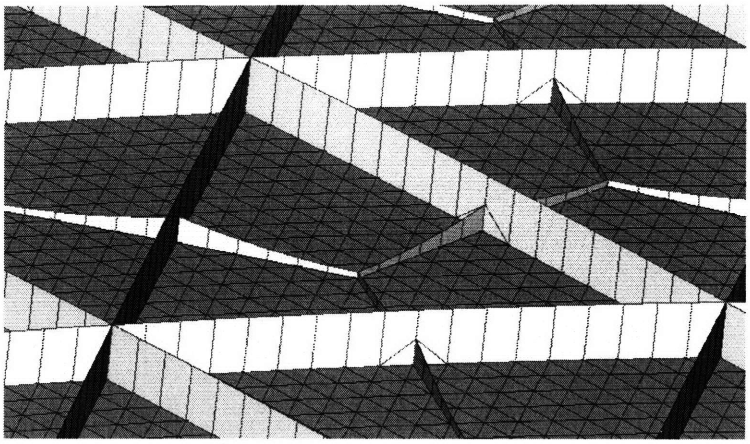

Figure 5-11: Sample MOST realization showing tapered cathedral ribs

Cathedral rib taper ratio

The MOST mirror model has the capability to parametrically generate tapered cathedral ribs in addition to tapered primary ribs. The cathedral ribs are also tapered to a parabolic shape (within each rib cell) since their primary purpose is to prevent deflection due to a distributed load on the mirror surface during the polishing process.

The cathedral rib taper ratio determines the ratio of the cathedral rib height at the outside of the rib cell to the rib height at the cell midpoint. The parabolic taper is added for a constant cathedral mass fraction and constant average cathedral rib aspect ratio. A realization of the parabolic taper is shown in Figure 5-11.

A trade is conducted to study the effect of cathedral rib taper ratio on the RMS mirror deflection due to a uniform mirror surface pressure load. The applied load simulates the pressure applied by a polishing element during manufacturing. The resulting deflection simulates the variable wear rates and print-through error pattern produced by typical polishing processes. The simulation technique is more fully explained in Section 4.2.

The mirror is constrained by all primary rib nodes on the edges farthest from the facesheet, so the cathedral ribs mitigate the deflection only within each primary rib cell. The optimal taper ratio of the cathedral ribs is that which results in the lowest RMS deflection pattern. The results for RMS surface deflection across a range of cathedral rib taper ratios are shown in Figure 5-12, where the deflection results are normalized to the 1:1 taper ratio.

A taper ratio of 2.5 offers a 5.3% improvement in RMS surface deflection over untapered

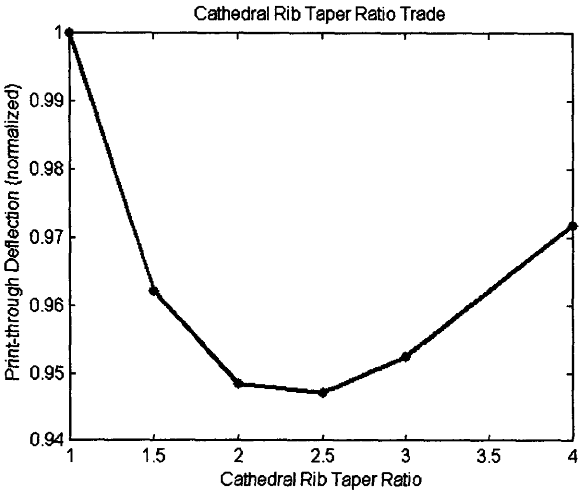

Figure 5-12: Cathedral rib taper ratio trade results (note vertical scale)

ribs, and this taper ratio is optimal over the range studied. Although this improvement is relatively small, the results indicate that print-through can be more effectively mitigated with tapered cathedral ribs. The effect of tapered cathedral ribs on other performance metrics, however, must also be considered.

5.4.3 Optimal design relationships

This section details the methods for developing a series of optimal design heuristics in terms of the objective function defined in Equation 5.1 in Section 5.3. A sample full factorial trade space for facesheet mass fraction and primary rib aspect ratio is presented as a representative example of the results included in Appendix A. This section defines the variable mirror parameters and details how optimal design heuristics are gathered from the trade space results.

Variable parameters

Four independent variables were isolated as the most influential in the mirror optimization process in Section 5.4.1. These variables, the ranges over which they are studied, and the discretization step sizes are summarized in Table 5.3. The dimpling-to-print-through ratio and cathedral mass fraction, although listed as two separate variables, are varied simultaneously according to the schedule in Table 5.2 and effectively function as a single independent variable. The remaining structural parameters are fixed to their baseline values.

Table 5.3: Summary of independent variables for mirror design optimization

Variable	**Range**	**Discretization**
Facesheet mass fraction	40% - 90%	5%
Primary rib aspect ratio	10 - 120	10
Areal density	5kg/m^2 - 15kg/m^2	5kg/m^2
Dimpling-to-print-through ratio	0.1 - 100	varies
Cathedral mass fraction	0% - 11%	~3%

Table 5.4: Summary of fixed parameters for mirror design optimization

Parameter	Fixed Value
Diameter	1m
Shape	hexagonal
F-number	1
Rib cell geometry	triangular
Curvature	parabolic (on axis)
Radius of curvature	6m
No. of actuators	42
Rib taper ratios	1
Cathedral rib thickness	2mm

Table 5.4 summarizes key fixed parameters.

Example trade space results

This section provides a representative example of how the optimal design relationships are developed. Similar results for each combination of the independent variables are included in Appendix A.

For a particular areal density and dimpling-to-print-through ratio, a full factorial search is first conducted over facesheet mass fraction and primary rib aspect ratio at their specified discretization step sizes. A contour plot with solid contours spaced at 5nm increments is used to show the value of the high spatial frequency residual objective function for all points within the trade space. Also shown with dashed contours are values of the fundamental frequency of the mirror. The example trade space in Figure 5-13 shows the combined contour plot for an areal density of 15kg/m^2 and a dimpling-to-print-through ratio of 3:1 (3% cathedral mass fraction).

The solid contours in Figure 5-13 represent the value of the high spatial frequency residual. The behavior of these solid contours shows that the minimum objective function values tend toward very high aspect ratios and facesheet mass fractions. This result is intuitive for

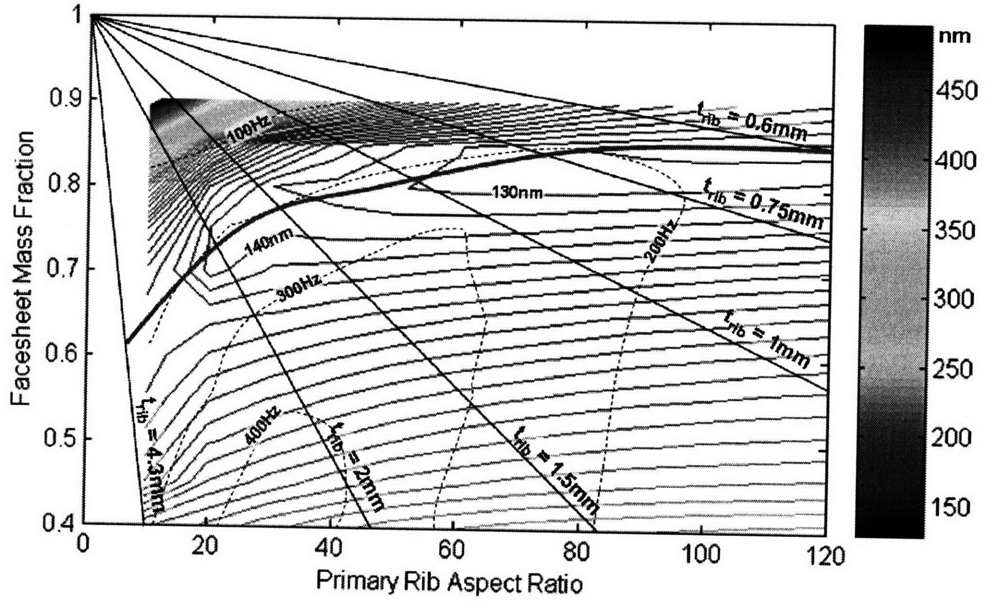

Figure 5-13: Sample full factorial tradespace contour plot, 15kg/m^2 areal density, 3:1 dimpling-to-print-through ratio, 3% cathedral mass fraction. Contours correspond to constant high spatial frequency residual.

dimpling, where stiffer structures produce more global, smooth influence functions and, as a result, less dimpling. The result is problematic in practice, however, because the primary rib aspect ratio is limited by the minimum possible rib thickness. A practical minimum that considers modern machining processes is 1mm [5]; however, other manufacturing methods may produce ribs of other thicknesses. It is therefore convenient to summarize the results as a function of minimum machinable rib thickness (via casting, molding, etc.) since this value may differ greatly by manufacturer. The straight lines in Figure 5-13 indicate the limits imposed by these rib thicknesses. Each limit constrains the feasible trade space to the lower left. In other words, the infeasible region for a given rib thickness limit is above (higher facesheet mass fraction) and to the right (higher rib aspect ratio).

The solid thick line in Figure 5-13 marks the loci of optimal designs for facesheet mass fraction and primary rib aspect ratio for varying minimum machinable rib thickness. Curve fitting these data against the corresponding rib thickness values produces the desired optimal design relationships (i.e. the developed heuristics). Equations 5.4(a)-(c) summarize these relationships for the optimal facesheet mass fraction (FS, %), optimal primary rib aspect ratio (AR), and optimal surface residual (RSS, nm) for varying minimum machinable rib thickness (t_{rib}, mm). The valid range on rib thickness, obtained by the limits of the trade space, is $0.6\text{mm} < t_{rib} < 3.2\text{mm}$. These curve fits are provided to concisely summarize the optimality relationships for convenience, but are supplemented with the full factorial contour plots for completeness.

$$FS = 90.4 \exp(-0.11\, t_{rib}) \tag{5.4a}$$

$$AR = 53.1\, t_{rib}^{-1.3} \tag{5.4b}$$

$$RSS = -2.3\, t_{rib}^{2} + 19.8\, t_{rib} + 113.6 \tag{5.4c}$$

It is clear from the shape of the solid contours in Figure 5-13 and from the RSS result in Equation 5.4(c) that a mirror with progressively thinner ribs monotonically produces less high spatial frequency residual. This result indicates that mirrors can be made more accurately controllable (in terms of high spatial frequency residual) with the advancement of manufacturing technology that allows for the construction of thinner ribs.

The sensitivity of the values of the objective function to changes in t_{rib} is also worthy of note. The trade space in this example indicates that thinner ribs monotonically lead to more accurate mirrors; however, the absolute effect of rib thickness on the high spatial frequency residual must be considered. Note that considerably thick ribs ($t_{rib} = 2.0$mm, thick relative to the 1mm practical minimum) produce roughly 140nm of high spatial frequency residual, whereas much thinner ribs ($t_{rib} = 0.6$mm) decrease the RSS residual to only roughly 125nm, an 11% improvement. A large investment in manufacturing technology to allow for thinner ribs may not be justified for this marginal improvement in mirror performance. The behavior of the trade space for other mirrors differs, so the sensitivity in the results to changes in t_{rib} must be considered for each case.

Also shown in Figure 5-13 are values of the fundamental mirror bending frequency with dashed contours spaced at 100Hz increments. These contours are included in this example and in the complete results in Appendix A. The trend in mirror stiffness behavior, seen in the pattern of the dashed contours, is similar in each trade space. The mirror designs with the highest stiffness generally have a facesheet mass fraction of roughly 40% and a primary rib aspect ratio of roughly 40. The shapes of the dashed contours in Figure 5-13 indicate that the mirror stiffness generally decreases to its lowest values near the highest facesheet mass fractions (85-90%) and the highest rib aspect ratios (110-120).

Note that the mirror stiffness along a large portion of the optimality curve (thick solid line for $0.75 < t_{rib} < 4.3$mm) is roughly constant at approximately 200Hz. Optimal mirror designs for $t_{rib} < 0.75$mm have fundamental frequencies between 100Hz and 200Hz. Should the optimal mirror design not meet the stiffness requirement for a particular mission, the dashed contours must be used to select a sufficiently stiff architecture. Deviations from the thick solid line (for a given rib thickness) correspond to sub-optimal designs in terms of high spatial frequency residual. The stiffness contours allow the user to select a constrained-optimal solution that satisfies both rib thickness and stiffness requirements while minimizing high spatial frequency residual.

Further results

Appendix A contains additional trade space results for the combinations of areal density and dimpling-to-print-through ratio listed in Table 5.2. This section discusses key points regarding the information contained in these trade space results.

Each trade space features solid contours representing increments in the objective function for high spatial frequency residual. The amount of residual in nanometers is reflected in the colorbar in each case. For clarity, however, selected contours are also labeled separately. The contours represent increments of 5nm in all cases except the 1:10 dimpling-to-print-through ratio cases where the contours are spaced at 50nm increments.

Each trade space also features straight lines showing locations of constant rib thickness, as in the example in Figure 5-13. The rib thickness values chosen include those that are critical in the trade space relative to the thick solid optimality curve, such as the minimum and maximum rib thicknesses for optimal designs within the bounds of the trade space. Note that some results in Appendix A have piece-wise optimality curves where the set of optimal designs relative to rib thickness is discontinuous. The curve fits for the optimality relationships for these cases are also reported as piece-wise in the associated tables (Tables A.1 - A.5).

The trade space results also all have dashed contours showing values of constant fundamental bending frequency. These contours are spaced at increments of either 50Hz or 100Hz for the best readability, and are labeled appropriately.

The cathedral ribs are limited to have heights no greater than the adjoining primary ribs. For this reason, certain mirror designs within the trade space are geometrically infeasible and are disregarded altogether. Instances of such designs can be seen in the trade space results where the objective function is undefined and the contour plot ends abruptly. These infeasible regions are more pronounced in mirror designs with higher cathedral mass fractions as the infeasible region to the upper left extends further into the trade space. The upper left region corresponds to high facesheet mass fraction for a given cathedral mass fraction (i.e. low primary rib mass fraction) and low primary rib aspect ratio. These combined effects can lead to cathedral ribs having heights greater than that of the primary ribs, and hence lead to an infeasible region in the trade space. The boundary to this infeasible is denoted by a thick hashed line when it exists.

Selected trade space results for $f/5$ are also included in Appendix A to dictate the low sensitivity in the optimality results to changes in f-number. As discussed in Section 5.4.1, higher f-number mirrors are expected to exhibit similar results for optimal designs and are typified by a slightly higher optimal facesheet mass fraction for a given rib thickness. This notion can be seen when comparing the trade space results in Figures A-9 and A-16 for mirrors with an areal density of 15kg/m^2, 3:1 dimpling-to-print-through ratio, and f-numbers of one and five, respectively. The optimality curves in these two figures behave similarly, with the curve for $f/5$ shifted slightly upwards to higher facesheet mass fractions by 5% to 8% in the 0.5-1mm region, as expected. There is also no noiticeable difference in the stiffness contours when comparing the dashed contour lines in Figures A-9 and A-16.

Also, the magnitudes of the objective function are significantly smaller in higher f-number mirrors. This is because the relative curvature change to simulate 1mm ΔRoC (the standard command to induce dimpling) is smaller for higher f-number mirrors (per Equation 4.6 for high RoC). The key takeaways for the surface residual relationships are therefore the *relative*, or proportional, differences for changes in rib thickness, rather than the *absolute* differences. The residual levels may be scaled in magnitude linearly for greater ΔRoC requirements due to the linearity in the MOST model. Selected contours are also labeled separately in the $f/5$ results for clarity. These contours are spaced at increments of 0.2nm.

Lastly, note that the optimality relationships listed in Tables A.1 - A.5 do not convey *cost sensitivity*, or the sensitivity in the value of the objective function, or *cost*, to deviations away from the optimal curves. The curves, both in graphical and equation form, represent the exact solutions for the minimum high spatial frequency residual, and they do not express information regarding the gradient of the objective function in the region surrounding the optimal curve. High cost gradients in proximity of the optimality curves produce high cost sensitivity.

Mathematically, for an n-dimensional cost function $\bar{F}$ and state vector $\bar{\chi}$, the gradient of the cost function is defined as [19]:

$$\text{cost gradient} = \frac{\partial \bar{F}}{\partial \bar{\chi}} \tag{5.5}$$

By definition, the cost gradient is equal to zero (or zero matrix) at a local extreme point, $\bar{\chi}^*$. However, small deviations from the extreme point in the state space, $\Delta\bar{\chi}$, will increase cost (if the extreme point is a strong minimum) by an amount:

$$\Delta \bar{F} \approx \frac{\partial \bar{F}}{\partial \bar{\chi}} \Delta \bar{\chi} \tag{5.6}$$

A high cost sensitivity at a particular state, $\bar{\chi}$, indicates that $\Delta\bar{F}$ is high for relatively small $\Delta\bar{\chi}$. The level of cost sensitivity is not reflected in the optimality curves in Tables A.1 - A.5. In other words, the equations do not convey the degree to which the RSS residual (i.e. $\bar{F}$) changes when the facesheet mass fraction and aspect ratio (i.e. $\bar{\chi}$) are sub-optimal. As a result, the contour plots are included to supplement the equations and to provide a visual indication of the cost sensitivity at all points in the trade space.

5.5 Summary

This chapter discussed details of the structural design optimization process and its results for a lightweight, hexagonal, rib-stiffened mirror segment. The optimization methods in this chapter, which use the parametric finite-element modeling of MOST, are conducted to improve upon the lightweight mirror design heuristics that are currently applied in industry. These heuristics are typically developed using simplified structural models, and hence do not capture the coupling relationships of the various structural parameters. The optimal design relationships in this chapter create improved guidelines and insight for the mirror structural design process.

This chapter first discussed a number of options for trade space exploration. The gradient descent approach was selected from a number of candidate search algorithms to rapidly explore the mirror structural design trade space, and is discussed in Section 5.2. Although full-factorial searches are also used in this chapter and in Appendix A, a gradient descent algorithm is used for many optimization routines to efficiently search for design optima. Gradient descent was chosen over other candidate algorithms (e.g. simulated annealing, orthogonal arrays) because of the balance it provides between accuracy (in finding global optima) and computational efficiency. It is guaranteed to find a global optima for convex cost functions, and the cost functions for the trade spaces studied herein are well-behaved and convex in most cases. When conducted on a uniformly discretized grid over the trade space variables, the algorithm requires a number of iterations proportional to both the number of variables, n, and the number of discretizations of each variable, s. The computational complexity is thus moderate at $O(sn)$.

The objective function, detailed in Section 5.3, quantifies the total amount of uncorrectable, high spatial frequency residual in the deformable mirror surface. Chapter 4 explained how this uncorrectable residual has two high spatial frequency components: actuation-induced dimpling and manufacturing-induced print-through. The objective function in Equation 5.1 quantifies the effects of these two components and treats them as independent variables via a root-sum-square. Since the magnitudes of the simulations used to model the dimpling and print-through effects are arbitrary, a *dimpling-to-print-through ratio* is used to calibrate the objective function and capture the relative magnitudes of these two effects.

Lastly, Section 5.4 presented the results of the optimization routines. A number of single axis trades first identified that the optimization results have a high sensitivity to the areal density and to the dimpling-to-print-through ratio, whereas the results have a low sensitivity to changes in f-number. These sensitivity analyses help refine the trade space and allow the optimization routines to focus on the most interesting and sensitive mirror design variables. A full factorial trade space search is then conducted over areal density, dimpling-to-print-through ratio, facesheet mass fraction, and primary rib aspect ratio. The optimal cathedral mass fraction is shown to be highly coupled to the dimpling-to-print-through ratio (greater print-through demands more cathedral mass, greater dimpling demands less cathedral mass), so the cathedral mass fraction is varied simultaneously with the dimpling-to-print-through ratio according to the schedule in Table 5.2.

The results for an example full factorial trade space search are included as a representative of the complete set of results in Appendix A. For each combination of areal density and dimpling-to-print-through ratio, and for selected $f/5$ cases, these results include two superimposed contour plots showing the values of both the objective function and the fundamental bending frequency for variations in facesheet mass fraction and primary rib aspect ratio. The optimality relationships for the mirror designs in the trade space that produce the least high spatial frequency error are reported in terms of the minimum machinable rib thickness to allow the results to meet manufacturing requirements. These developed design heuristics are presented in equation form for convenience to supplement the visual information in the contour plots.

Chapter 6

Conclusion

This chapter summarizes the key conclusions of this work. A brief summary of the motivation, process, and results discussed throughout this thesis is included and is followed by a concise presentation of the individual contributions of this work. Lastly, this chapter details recommendations for future work related to lightweight mirror design optimization.

6.1 Thesis Summary

This thesis first presented the motivation and approach for optimizing the structural design of a lightweight, deformable mirror segment in Chapter 1. An introduction to the space telescope modeling capabilities of MOST was also included. Chapter 2 presented a brief review of works related to mirror shape control and design optimization. These reviews provided the context in which this work was conducted.

The goal of the thesis is to develop more accurate mirror structural design heuristics that improve on the simplified design techniques used in industry. This section provides a brief summary of the approach used in this thesis to develop these heuristics.

Mirror design and shape control

Chapter 3 presented details of the design and control of a deformable mirror segment model. The mirror studied is a lightweight and rib-stiffened hexagonal segment. Similar to designs popular in industry, the mirror features a thin facesheet and a backstructure composed of both primary and cathedral ribs for support. The MOST model generates a Nastran finite element model using a number of user-specified structural parameters. These parameters determine the geometry and material properties of the mirror segment, and include parameters such as the areal density, f-number, diameter, and structural mass fractions. A series of baseline parameters define a mirror that is used as a baseline design throughout this thesis for reference.

This thesis takes a conventional approach to mirror shape control, or the process of using embedded actuators to change the shape of the mirror surface to mitigate the effects of disturbances. If uncorrected, these shape disturbances adversely affect the system's imaging capability. The embedded actuators are modeled as rod elements on the outside edge of each rib section, and they push and pull on the primary ribs, parallel to the mirror surface, to create surface displacement patterns (i.e. influence functions). The shape control approach employs nodal influence functions and three fictitious actuators to smoothly and accurately control for a given mirror shape disturbance. The nodal influence function approach controls the z-displacements of mirror surface nodes and was shown to be more effective than alternative control methods, such as Zernike control which controls the modes in the disturbance by means of a Zernike transformation.

High spatial frequency mirror surface residual

Chapter 4 discussed the three predominant sources of high spatial frequency residual for lightweight, deformable mirrors: actuation-induced dimpling, manufacturing-induced print-through, and thermally-induced ripple. Dimpling is a high spatial frequency pattern of repeated circular dimples that appears when a mirror makes a low-order shape command. It is simulated by commanding a 1mm increase in radius of curvature in the mirror segment model. The resulting shape is subtracted from the desired paraboloidal shape, and the RMS of the difference is the dimpling residual. The dimpling residual on the baseline mirror segment, for instance, is roughly 90nm.

Print-through is simulated by applying a uniform pressure to the mirror surface and measuring the RMS of the static deformation. This pressure and resulting deformation pattern simulates the effects of a spatially variable wear rate during the polishing process due to variable mirror stiffness. The outside rib nodes of the FEM (those farthest from the facesheet) are constrained in all translational DOF during this simulation as if the mirror backstructure rested on a rigid support during polishing. The print-through residual on the baseline mirror design for a 225Pa polishing pressure is roughly 30nm.

Thermal ripple is the third predominant source of high spatial frequency residual on rib-stiffened lightweight mirrors. It is defined as the high spatial frequency component of the mirror deformation due to a thermal disturbance. It is simulated by applying a $1°\Delta T$ $[C]$ bulk temperature soak to a mirror segment. It is quantified by measuring the RMS of the components of the deformed mirror with spatial frequencies that lie above that of the actuator spacing. The thermal ripple on the baseline mirror segment has an RMS of roughly 7.3nm, and is disregarded due to its relatively small magnitude. This thesis therefore focuses on the dimpling and print-through effects since they are the major sources of mirror surface residual assuming that the chosen perturbations are indicative of an actual manufacturing and operating environment.

Mirror structural design optimization and results

Chapter 5 discussed details of the structural design optimization process and its results for a lightweight, hexagonal, rib-stiffened mirror segment. The gradient descent approach was selected from a number of candidate search algorithms to rapidly explore the mirror structural design trade space. Gradient descent was chosen over other algorithms because it is guaranteed to find the global optima (for convex cost functions) and has a moderate computational complexity.

The objective function used to gauge the performance of a mirror quantifies the total amount of uncorrectable, high spatial frequency residual in the mirror surface. The objective function is composed of the effects of both actuation-induced dimpling and manufacturing-induced print-through. It treats these effects as independent variables via a root-sum-square since they are believed to be weakly correlated. However, the magnitudes of the simulations used to model the dimpling and print-through effects are arbitrary, so a *dimpling-to-print-through ratio* is used to calibrate the objective function and balance the relative magnitudes of these two effects.

Single axis trades were then used to identify variables to which the optimization results have a high sensitivity (namely, areal density and the dimpling-to-print-through ratio). In contrast, the results were seen to be only marginally sensitive to changes in f-number. A full factorial trade space search is then conducted over areal density, dimpling-to-print-through ratio, facesheet mass fraction, and primary rib aspect ratio to build insight into the behavior of the objective function across changes in these variables. The optimal cathedral mass fraction is varied simultaneously with the dimpling-to-print-through ratio throughout the optimizations since these two variables are highly coupled.

The complete set of trade space results are included in Appendix A as contour plots for values of the objective function. A separate set of contours for the values of the fundamental mirror bending frequency is superimposed on these figures. The plots are supplemented with optimality relationships in equation form. These optimality relationships are gathered in terms of the minimum machinable rib thickness to allow the results to meet manufacturing requirements. Further information regarding the optimization results, such as the *cost sensitivity* relative to the optimal mirror designs, may be gathered from the contour plots for the trade space results.

6.2 Contributions of this Thesis

The following list itemizes the key contributions of this thesis.

- Developed a methodology for optimizing mirror geometry to minimize high spatial frequency surface residual.
  - Developed an objective function to capture the independent effects of the predominant sources of high spatial frequency mirror surface residual.
  - Presented results of a full factorial search over a number of mirror structural design parameters showing the effect of the parameters on values of the objective function and on the fundamental bending frequency of the mirror segment.
  - Developed design heuristics using optimality relationships within the trade space results as a function of the minimum machinable rib thickness.
- Quantified the benefit of employing nodal influence functions for mirror shape control relative to Zernike influence functions.
  - Quantified the efficiency and robustness of numerical methods for solving theoretical mirror shape control problems.
- Developed standardized commands to simulate and quantify high spatial frequency mirror surface residual due to actuation-induced dimpling, manufacturing-induced print-through, and disturbance-induced ripple.

6.3 Future Work

This thesis provided the groundwork for an in-depth mirror design optimization process. Although this thesis answered many questions regarding the optimal design of a rib-stiffened mirror segment, a number of studies regarding mirror control and design optimization remain.

First, edge control issues may be explored. Discussed in Chapter 3, the control commands in this thesis utilized a 95% clear aperture to avoid the difficulties associated with controlling the edge of a deformable mirror. These difficulties arise because of the use of moment actuators, or those that impart nearly a pure moment in the mirror structure. Ideally, the entire aperture would be included in the shape control law. Disregarding any region of the mirror surface degrades the resolution of the system, so using a clear aperture calculation likely leads to sub-optimal control results. When using a clear aperture, the calculated shape control command typically drastically increases the surface residual in the disregarded region (i.e. the outer region of the mirror surface near the edges of the segment). This large amount of residual, although concentrated to a small region, greatly effects the total corrected surface residual and, hence, the imaging capability of the entire system.

Other types of actuators, such as force actuators, may also be included in the mirror model for improved edge control performance. Although using multiple types of actuators adds model complexity, the control performance is likely to be improved. The locations and orientations of these additional actuators must be evaluated in terms of mitigating poor edge control performance.

Additional optimizations of the mirror geometry are also possible. It remains to be seen whether spatially varying structural properties can be beneficial to the performance of the mirror segment. Section 5.4.1 conducted a study on the effect of both primary rib taper and cathedral rib taper, which are examples of spatially varying structural properties. Additional properties, such as facesheet thickness, primary rib thickness, and cathedral mass distribution, can be varied either as a function of the radial distance to the mirror center or as a function of the distance to the nearest point constraint.

Different rib cell patterns can also be evaluated in terms of similar objective functions. The MOST model and many lightweight mirrors seen in industry [15] use triangular rib cell patterns, but hexagonal rib cells are also possible. These alternative rib cell patterns must be evaluated in terms of several performance metrics (e.g. stiffness, dimpling, print-through) for sufficient comparison to the triangular cell pattern.

Additional objective functions are also possible. Optimizing a mirror for self-weight deflection, for instance, would be useful for ground based mirror optimization routines. Ground based mirror segments are not significantly plagued by high spatial frequency residual, as are space based mirror segments, because the segments used for ground based applications are more massive and rely less on rib-stiffening.

A second area of related future work is that of the sensitivity of the optimizations to both model parameters and constraints. Section 5.4.1 discussed the sensitivity of the optimization results to changes in areal density, f-number, and dimpling-to-print-through ratio. The trade space results in Appendix A visually show the sensitivity in the results to changes in facesheet mass fraction and rib aspect ratio. The sensitivity in the results to material properties such as elastic modulus, mass density, and thermal expansion coefficient, however, remains to be seen.

The mirror segments evaluated in this thesis were constrained identically using three point-constraints uniformly spaced at 120° increments (see Section 3.4) along the half-radius of the mirror segment. These point-constraints are used to mimic the effects of bipod constraints, which are also popular in industry. Although dimpling and print-through are seen to be *local* effects in Chapter 4, the *global* behavior of the residual patterns may be sensitive to the methods used to constrain the mirror. Alternative numbers and locations for constraints are therefore also possible to evaluate.

A final area of future work that is directly related to the research in this thesis is work towards developing more universal and generalizable optimal design relationships. Sensitivity analyses were used herein to determine the most sensitive structural parameters over which to optimize the mirror geometry. The resulting design heuristics were then presented as a function of each of these parameters in Appendix A. Drawing conclusions on the underlying relationships between all variable parameters, however, remains to be done. A concise representation of the optimal design relationships would be useful if they can be reduced to a limited number of equations.

Significant steps were taken to focus the optimization results in this thesis on the most applicable mirror design parameters and segment geometries. Capturing the effect of every variable in a large variable trade space, however, is a formidable task. There are therefore many directions to extend these optimization efforts and further apply rapid trade space exploration techniques over additional variables and objective functions.

Appendix A

Mirror Optimization Results

Table A.1: Summary of optimal design relationships for facesheet mass fraction (FS, %), primary rib aspect ratio (AR), and total high spatial frequency residual (RSS, nm) in terms of minimum machinable rib thickness (t_{rib}, mm). 1:10 dimpling-to-print-through ratio.

Areal Density	Optimality Relationships	Rib Thickness Range	
		Min	Max
5 kg/m^2	$FS = 80$	-	0.3
	$FS = 1.6\, t_{rib}^2 - 6.3\, t_{rib} + 82.0$	0.3	1.5
	$AR = 120$	-	0.3
	$AR = 20.1\, t_{rib}^{-1.7}$	0.3	1.5
	$RSS = 650$	-	0.3
	$RSS = -121.7\, t_{rib}^2 + 305.7\, t_{rib} + 555.0$	0.3	1.5
10 kg/m^2	$FS = 84$	-	0.4
	$FS = -0.2\, t_{rib}^2 - 9.1\, t_{rib} + 88.3$	0.4	3.3
	$AR = 67$	-	0.4
	$AR = 10.9\, t_{rib}^2 - 59.9\, t_{rib} + 86.5$	0.4	3.3
	$RSS = 525$	-	0.4
	$RSS = 85\, t_{rib}^2 - 90.6\, t_{rib} + 559.3$	0.4	3.3
15 kg/m^2	$FS = 83$	-	0.7
	$FS = -0.5\, t_{rib}^2 - 7.2\, t_{rib} + 88.1$	0.7	4.1
	$AR = 48$	-	0.7
	$AR = 5.2\, t_{rib}^2 - 35.9\, t_{rib} + 70.3$	0.7	4.1
	$RSS = 500$	-	0.7
	$RSS = 59.7\, t_{rib}^2 - 81.4\, t_{rib} + 530.0$	0.7	4.1

Table A.2: Summary of optimal design relationships for facesheet mass fraction (FS, %), primary rib aspect ratio (AR), and total high spatial frequency residual (RSS, nm) in terms of minimum machinable rib thickness (t_{rib}, mm). 1:1 dimpling-to-print-through ratio.

Areal Density	Optimality Relationships	Rib Thickness Range	
		Min	Max
5 kg/m^2	$FS = 69$	-	0.75
	$FS = 10.8\, t_{rib}^2 - 42.9\, t_{rib} + 94.6$	0.75	2.0
	$AR = 53$	-	0.75
	$AR = 37.6\, t_{rib}^2 - 137.8\, t_{rib} + 135.2$	0.75	2.0
	$RSS = 198$	-	0.75
	$RSS = 20\, t_{rib}^2 - t_{rib} + 187$	0.75	2.0
10 kg/m^2	$FS = 75$	-	1.1
	$FS = 2.7\, t_{rib}^2 - 19.4\, t_{rib} + 93.1$	1.1	3.4
	$AR = 40$	-	1.1
	$AR = 9.4\, t_{rib}^2 - 54.9\, t_{rib} + 88.3$	1.1	3.4
	$RSS = 175$	-	1.1
	$RSS = 15.5\, t_{rib} + 157.6$	1.1	3.4
15 kg/m^2	$FS = 75$	-	1.6
	$FS = -2.1\, t_{rib}^2 - 18.8\, t_{rib} + 99.6$	1.6	4.2
	$AR = 30$	-	1.6
	$AR = 3.9\, t_{rib}^2 - 31.7\, t_{rib} + 70.7$	1.6	4.2
	$RSS = 155$	-	1.6
	$RSS = -2.0\, t_{rib}^2 + 19.4\, t_{rib} + 129.2$	1.6	4.2

Table A.3: Summary of optimal design relationships for facesheet mass fraction (FS, %), primary rib aspect ratio (AR), and total high spatial frequency residual (RSS, nm) in terms of minimum machinable rib thickness (t_{rib}, mm). 3:1 dimpling-to-print-through ratio.

Areal Density	Optimality Relationships	Rib Thickness Range	
		Min	Max
5 kg/m^2	$FS = 65$	-	0.9
	$FS = 6.6\, t_{rib}^2 - 36.1\, t_{rib} + 91.7$	0.9	2.5
	$AR = 44$	-	0.9
	$AR = 15.1\, t_{rib}^2 - 71.7\, t_{rib} + 95.5$	0.9	2.5
	$RSS = 173$	-	0.9
	$RSS = 5\, t_{rib}^2 + 10.9\, t_{tib} + 157.5$	0.9	2.5
10 kg/m^2	$FS = 85$	-	0.5
	$FS = 2.2\, t_{rib}^2 - 18.1\, t_{rib} + 94.3$	0.5	3.5
	$AR = 107$	-	0.5
	$AR = 20.5\, t_{rib}^2 - 105.9\, t_{rib} + 137.7$	0.5	3.5
	$RSS = 150$	-	0.5
	$RSS = -2.5\, t_{rib}^2 + 19.4\, t_{rib} + 142.1$	0.5	3.5
15 kg/m^2	$FS = 90.4\, e^{-0.11\, t_{rib}}$	0.6	4.3
	$AR = 53.1\, t_{rib}^{-1.3}$	0.6	4.3
	$RSS = -2.3\, t_{rib}^2 + 19.8\, t_{rib} + 113.6$	0.6	4.3

Table A.4: Summary of optimal design relationships for facesheet mass fraction (FS, %), primary rib aspect ratio (AR), and total high spatial frequency residual (RSS, nm) in terms of minimum machinable rib thickness (t_{rib}, mm). 10:1 dimpling-to-print-through ratio.

Areal Density	Optimality Relationships	Rib Thickness Range	
		Min	Max
5 kg/m^2	$FS = 62$	-	1.3
	$FS = 3.3\,t_{rib}^2 - 19.3\,t_{rib} + 81.5$	1.3	2.5
	$AR = 25$	-	1.3
	$AR = 18.8\,t_{rib}^2 - 77.5\,t_{rib} + 94.1$	1.3	2.5
	$RSS = 178$	-	1.3
	$RSS = -4.2\,t_{rib}^2 + 24.2\,t_{rib} + 153.1$	1.3	2.5
10 kg/m^2	$FS = 86.7\,t_{rib}^2 - 179.7\,t_{rib} + 156$	0.75	1.0
	$FS = 1.5\,t_{rib}^2 - 13.9\,t_{rib} + 89.6$	1.0	3.6
	$AR = -0.8\,t_{rib}^2 + 1.3\,t_{rib} - 0.4$	0.75	1.0
	$AR = 20.5\,t_{rib}^2 - 105.9\,t_{rib} + 137.7$	1.0	3.6
	$RSS = 133\,t_{rib}^2 - 153.3\,t_{rib} + 140$	0.75	1.0
	$RSS = -7.1\,t_{rib}^2 + 46.4\,t_{rib} + 80.9$	1.0	3.6
15 kg/m^2	$FS = 35.4\,t_{rib}^2 - 98.8\,t_{rib} + 133.8$	0.8	1.4
	$FS = 2.4\,t_{rib}^2 - 19.1\,t_{rib} + 99.5$	1.4	4.4
	$AR = 47.9\,t_{rib}^2 - 201.3\,t_{rib} + 250.3$	0.8	1.4
	$AR = 9.8\,t_{rib}^2 - 68.3\,t_{rib} + 116.4$	1.4	4.4
	$RSS = 16.7\,t_{rib}^2 - 10\,t_{rib} + 76.3$	0.8	1.4
	$RSS = -6.3\,t_{rib}^2 + 49.6\,t_{rib} + 37.8$	1.4	4.4

Table A.5: Summary of optimal design relationships for facesheet mass fraction (FS, %), primary rib aspect ratio (AR), and total high spatial frequency residual (RSS, nm) in terms of minimum machinable rib thickness (t_{rib}, mm). 100:1 dimpling-to-print-through ratio.

Areal Density	Optimality Relationships	Rib Thickness Range	
		Min	Max
5 kg/m^2	$FS = 56$	-	1.5
	$FS = -5.5\,t_{rib} + 64.3$	1.5	2.5
	$AR = 21$	-	1.5
	$AR = -12.5\,t_{rib} + 39.3$	1.5	2.5
	$RSS = 17.4$	-	2.5
10 kg/m^2	$FS = -9\,t_{rib}^2 - 14.3\,t_{rib} + 83.8$	0.8	1.3
	$FS = 1.5\,t_{rib}^2 - 14.9\,t_{rib} + 90.9$	1.3	3.6
	$AR = 211.7\,t_{rib}^2 - 553.5\,t_{rib} + 427.3$	0.8	1.3
	$AR = 6.8\,t_{rib}^2 - 45.3\,t_{rib} + 81.9$	1.3	3.6
	$RSS = 56.7\,t_{rib}^2 - 47\,t_{rib} + 89.3$	0.8	1.3
	$RSS = -6.8\,t_{rib}^2 + 42.4\,t_{rib} + 80.3$	1.3	3.6
15 kg/m^2	$FS = -0.4\,t_{rib}^2 - 19.8\,t_{rib} + 88.2$	0.9	1.9
	$FS = 1.4\,t_{rib}^2 - 13.8\,t_{rib} + 93$	1.9	4.4
	$AR = 51.7\,t_{rib}^2 - 220.7\,t_{rib} + 276.8$	0.9	1.9
	$AR = 2\,t_{rib}^2 - 19.7\,t_{rib} + 54.2$	1.9	4.4
	$RSS = 31.7\,t_{rib}^2 - 57.7\,t_{rib} + 97.3$	0.9	1.9
	$RSS = -4.1\,t_{rib}^2 - 33.1\,t_{rib} + 54$	1.9	4.4

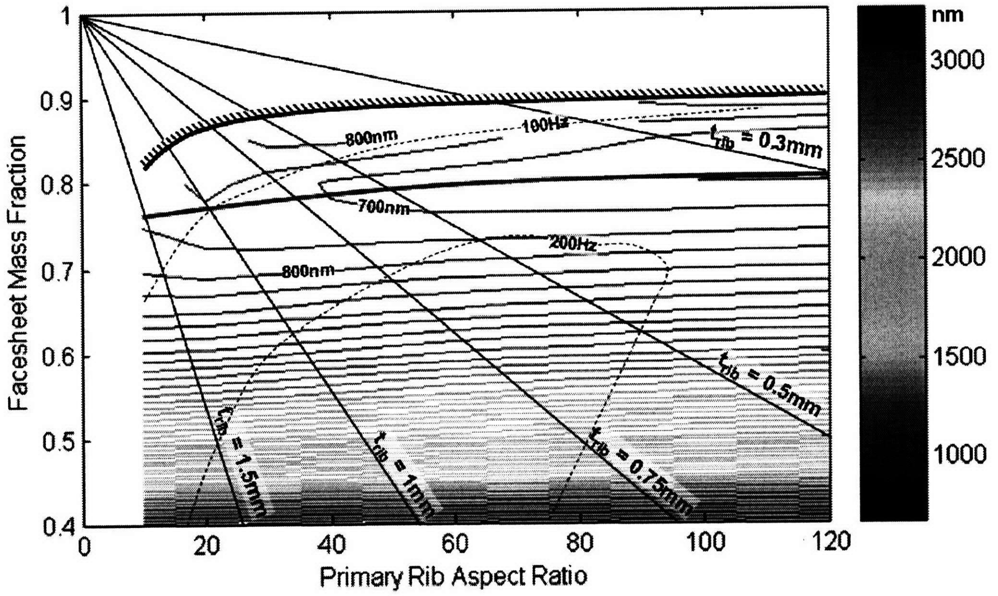

Figure A-1: Trade space results: 1:10 dimpling-to-print-through ratio, 10% cathedral mass fraction, 5 kg/m^2

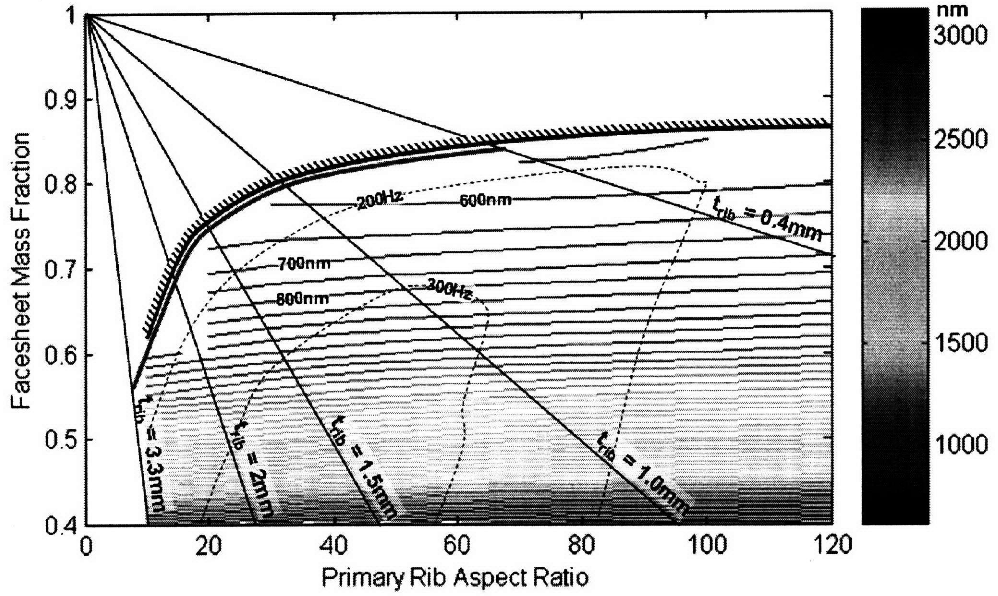

Figure A-2: Trade space results: 1:10 dimpling-to-print-through ratio, 11% cathedral mass fraction, 10 kg/m^2

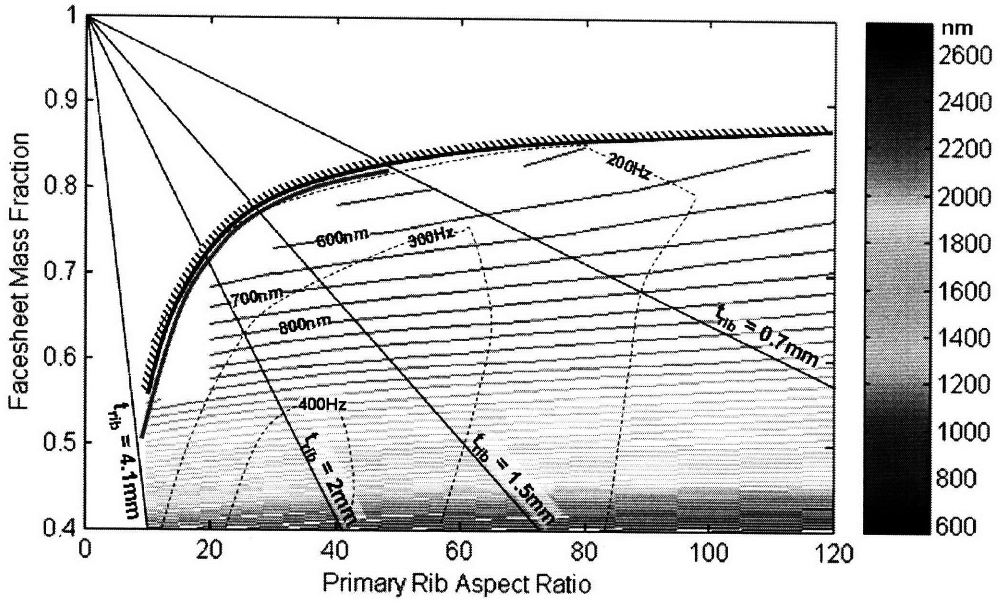

Figure A-3: Trade space results: 1:10 dimpling-to-print-through ratio, 9% cathedral mass fraction, 15 kg/m^2

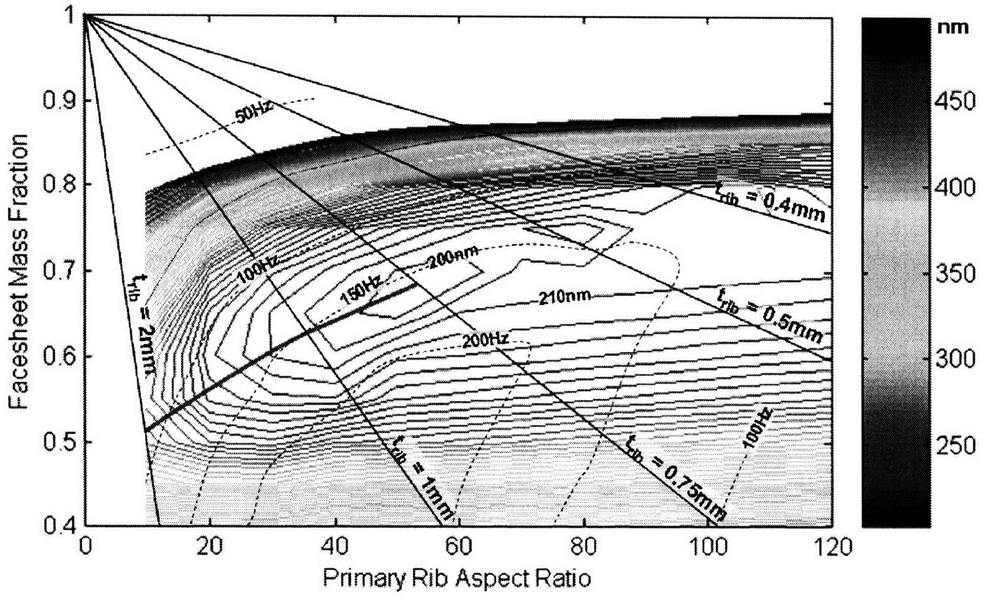

Figure A-4: Trade space results: 1:1 dimpling-to-print-through ratio, 6% cathedral mass fraction, 5 kg/m^2

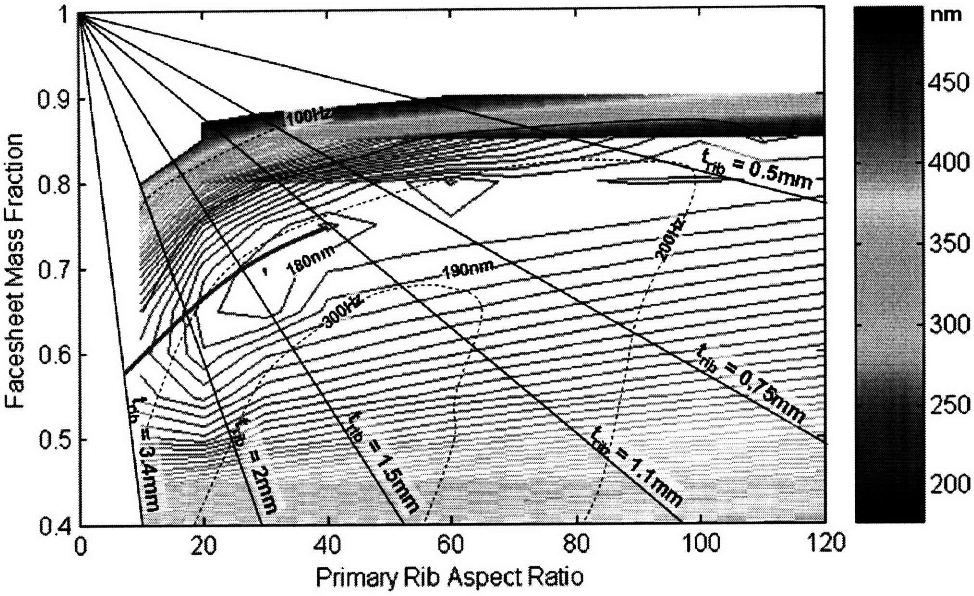

Figure A-5: Trade space results: 1:1 dimpling-to-print-through ratio, 6% cathedral mass fraction, 10 kg/m^2

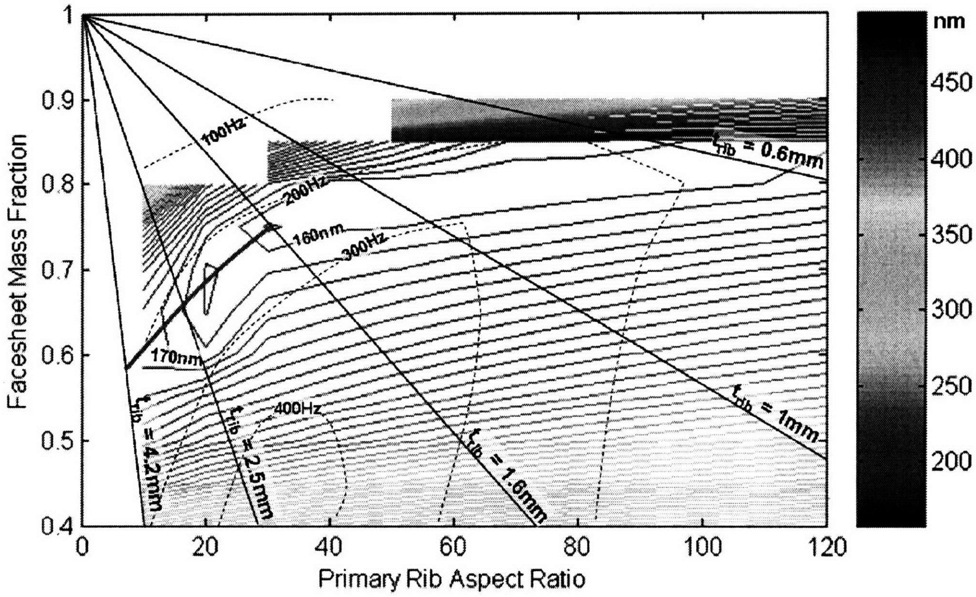

Figure A-6: Trade space results: 1:1 dimpling-to-print-through ratio, 6% cathedral mass fraction, 15 kg/m^2

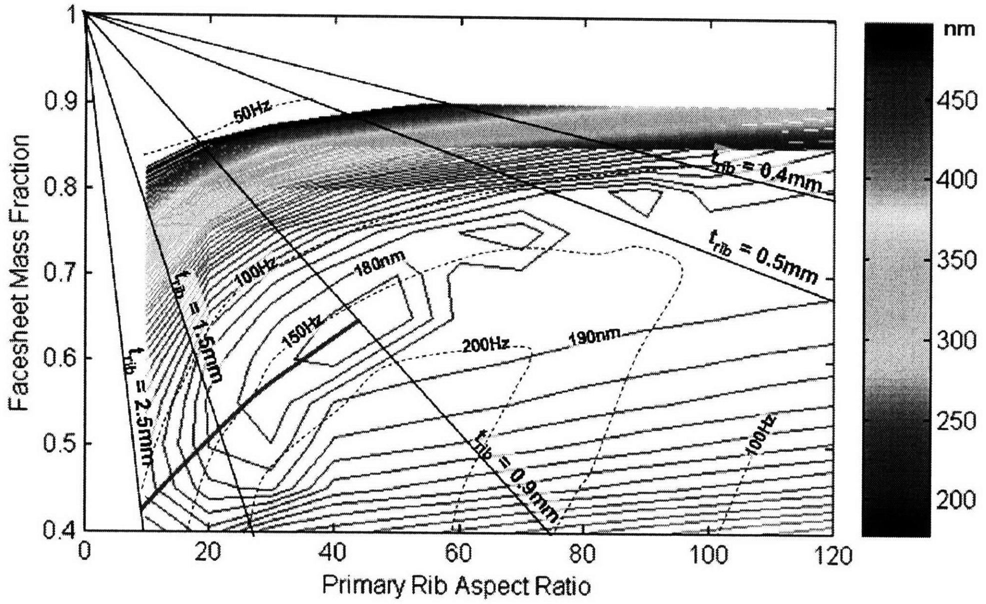

Figure A-7: Trade space results: 3:1 dimpling-to-print-through ratio, 3% cathedral mass fraction, 5 kg/m^2

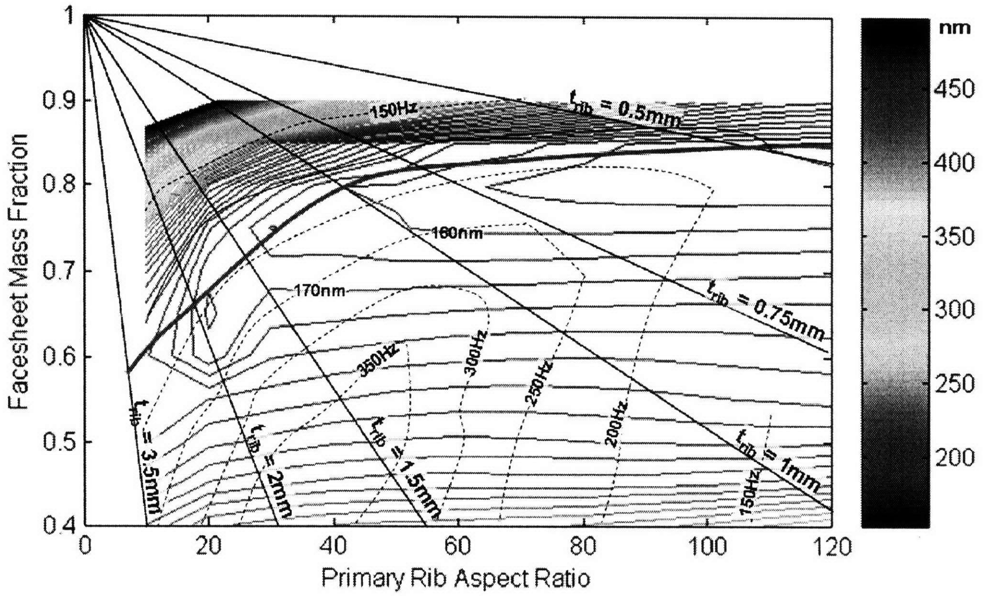

Figure A-8: Trade space results: 3:1 dimpling-to-print-through ratio, 3% cathedral mass fraction, 10 kg/m^2

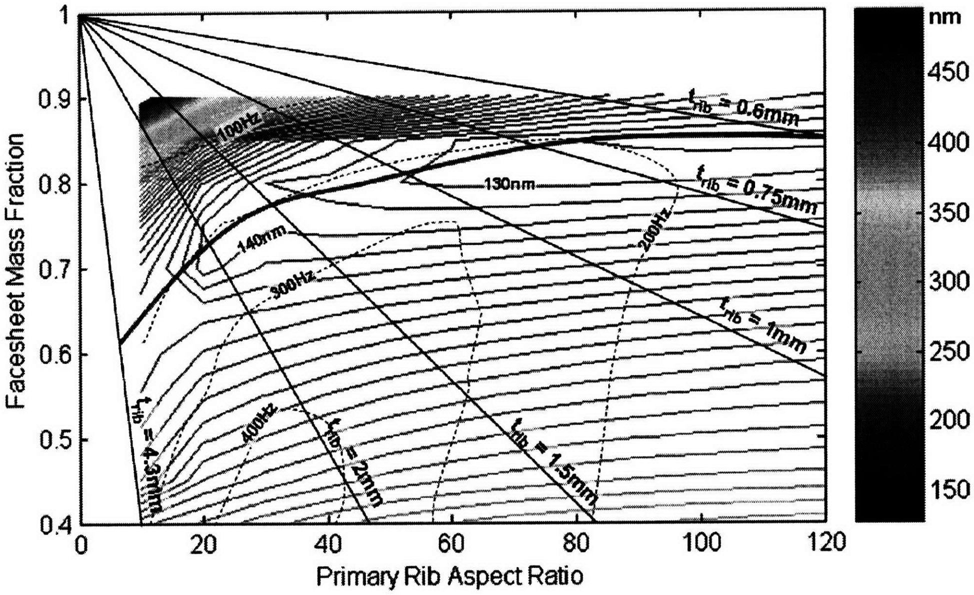

Figure A-9: Trade space results: 3:1 dimpling-to-print-through ratio, 3% cathedral mass fraction, 15 kg/m^2

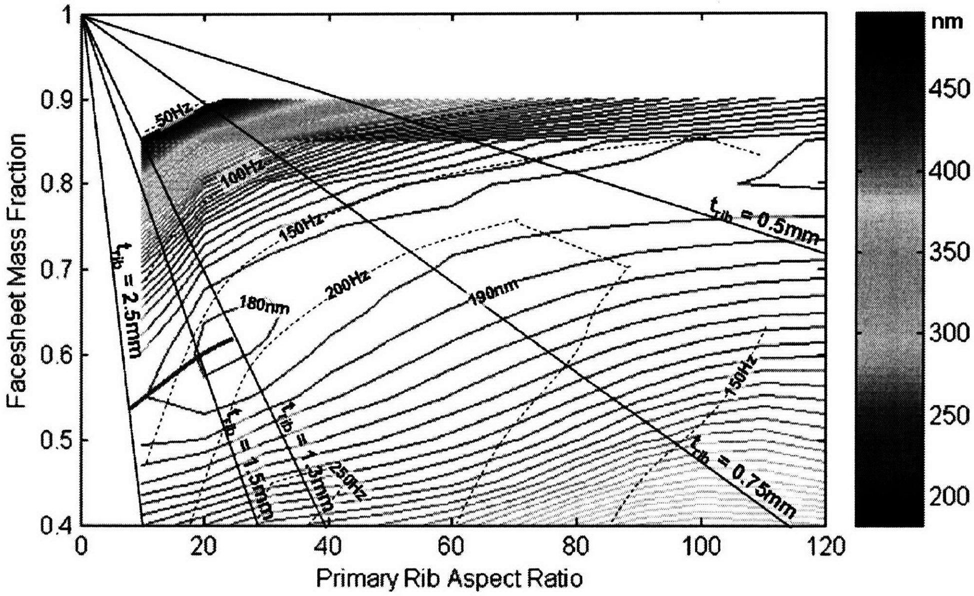

Figure A-10: Trade space results: 10:1 dimpling-to-print-through ratio, 0% cathedral mass fraction, 5 kg/m^2

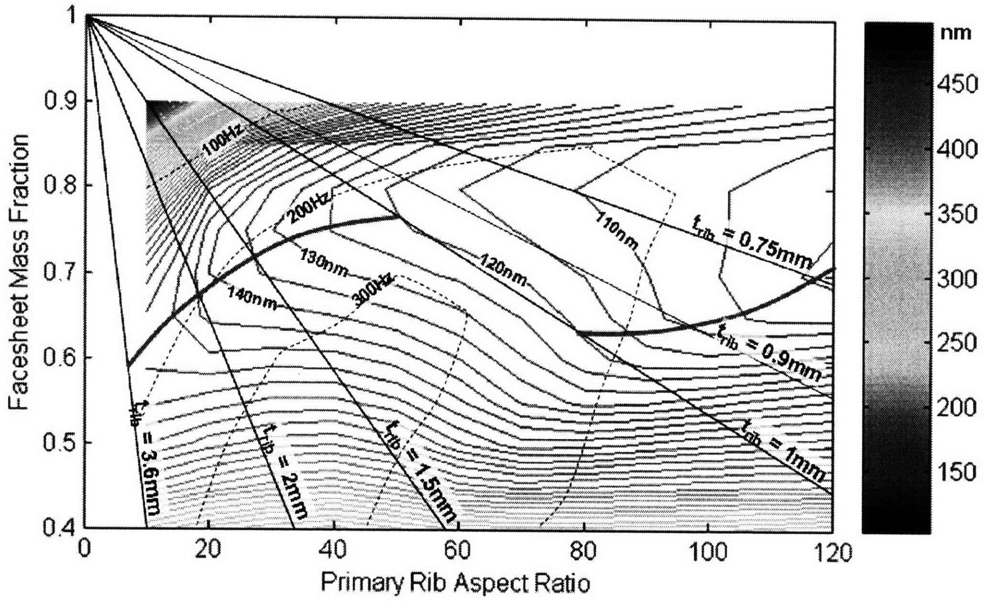

Figure A-11: Trade space results: 10:1 dimpling-to-print-through ratio, 0% cathedral mass fraction, 10 kg/m^2

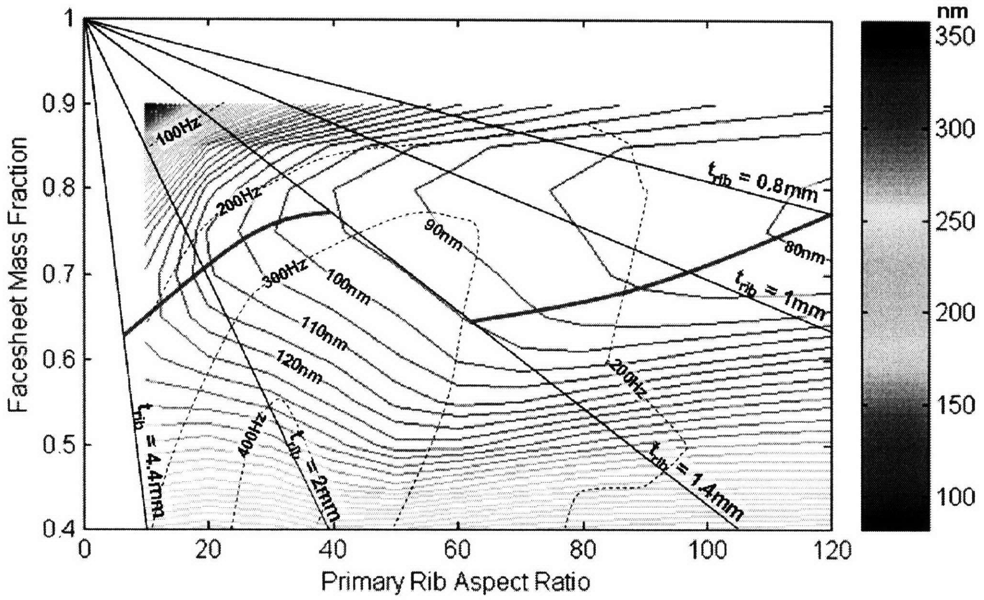

Figure A-12: Trade space results: 10:1 dimpling-to-print-through ratio, 0% cathedral mass fraction, 15 kg/m^2

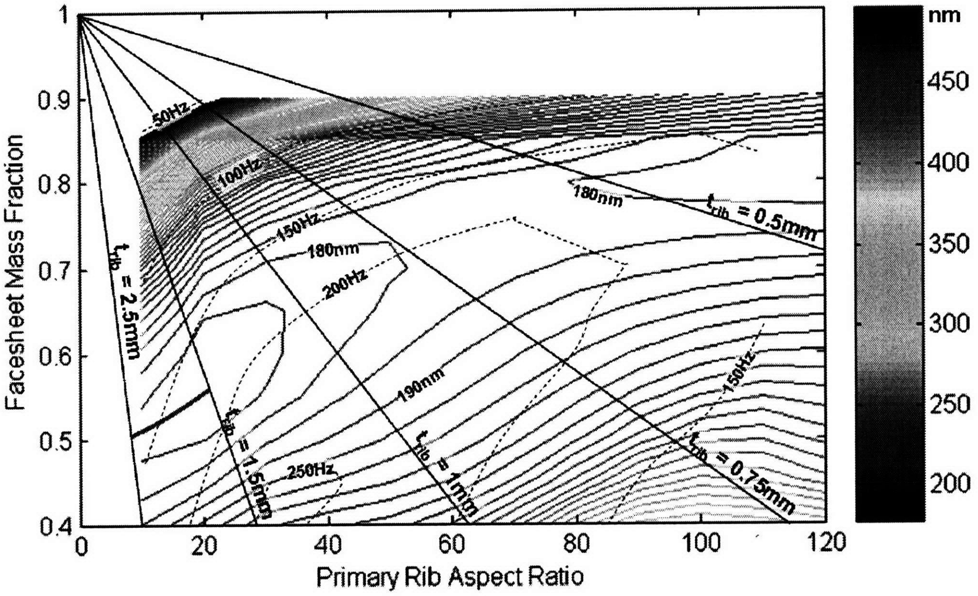

Figure A-13: Trade space results: 100:1 dimpling-to-print-through ratio, 0% cathedral mass fraction, 5 kg/m^2

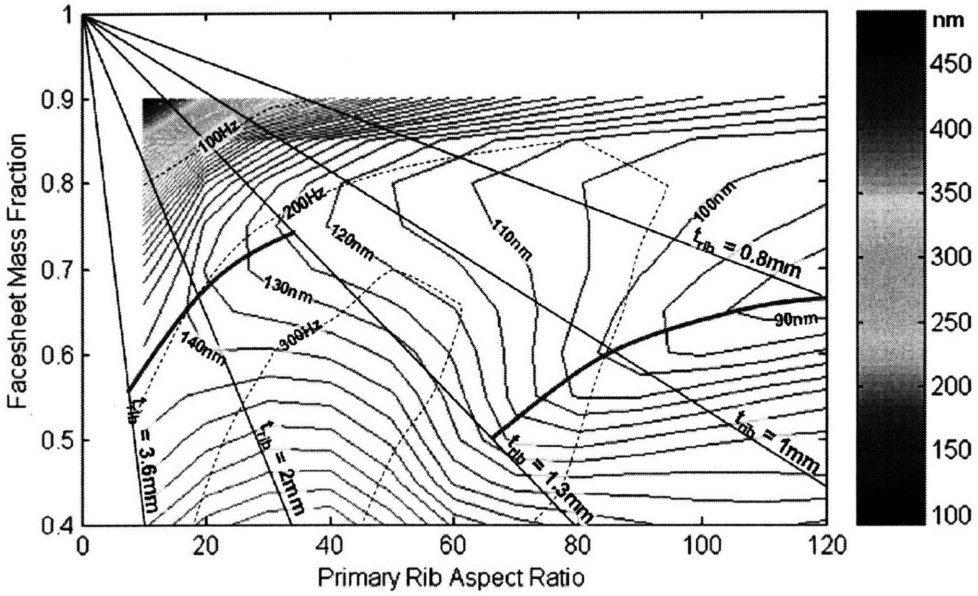

Figure A-14: Trade space results: 100:1 dimpling-to-print-through ratio, 0% cathedral mass fraction, 10 kg/m^2

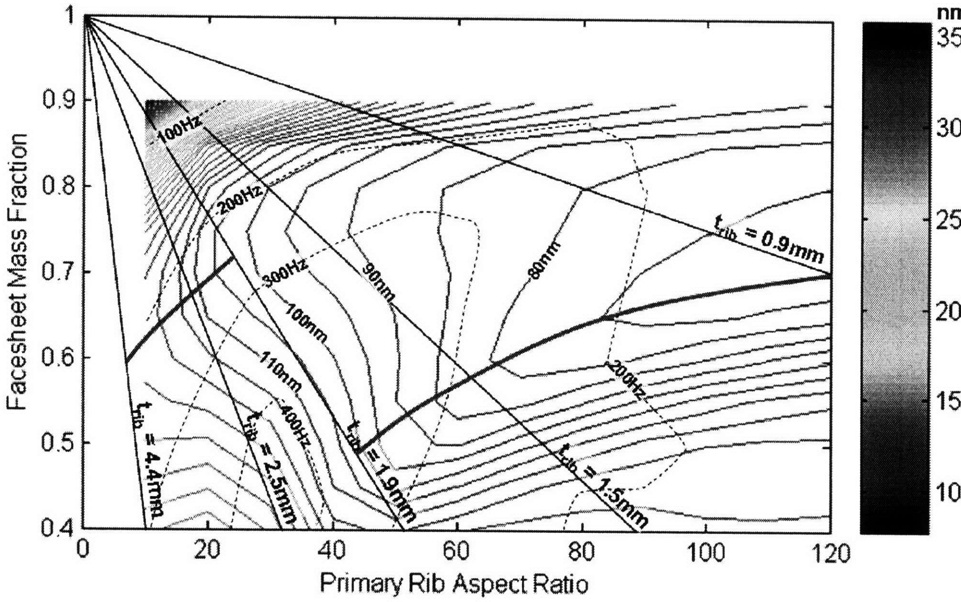

Figure A-15: Trade space results: 100:1 dimpling-to-print-through ratio, 0% cathedral mass fraction, 15 kg/m^2

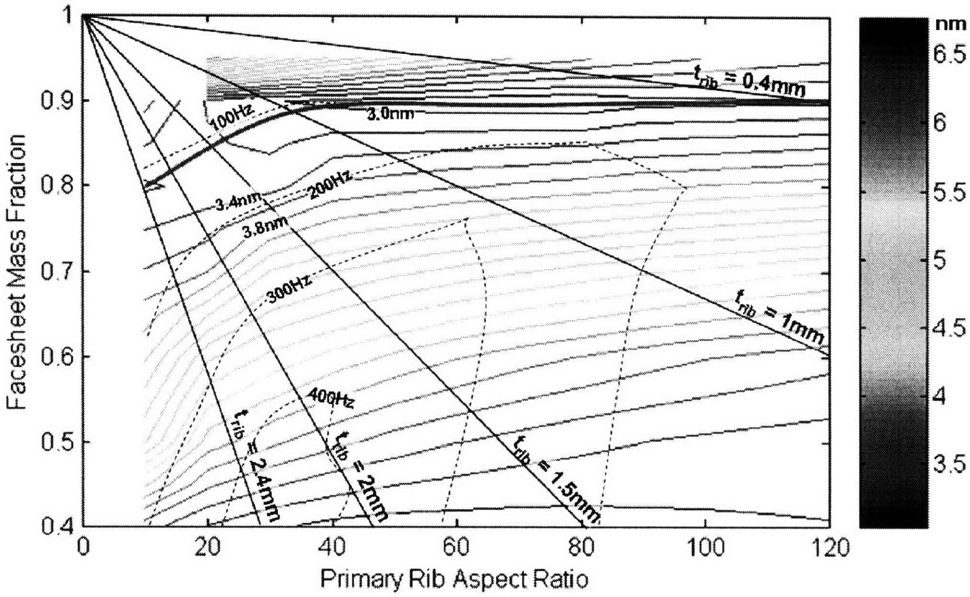

Figure A-16: Trade space results: 3:1 dimpling-to-print-through ratio, 3% cathedral mass fraction, 15 kg/m^2, $f/5$

Appendix B

Zernike Polynomials

The Zernike polynomials belong to an infinite series of odd and even polynomials in polar coordinates (ρ, θ) that are orthogonal over the unit circle. For all $n \geq m \geq 0$, the polynomials are defined by Equation B.1. For each m, n, the polynomials consist of an odd ($\sin(m\theta)$ and even ($\cos(m\theta)$) pair. Each $m = 0$ pair reduces to a single, purely radial polynomial for the $\cos(0)$ case.

$$\zeta_n^m = \sum_{t=0}^{n-m} \frac{(-1)^t (2n-m-t)!}{t!(n-t)!(n-m-t)!} \rho^{2(n-t)-m} \times \begin{cases} \cos(m\theta), & \zeta_n^m \text{ even} \\ \sin(m\theta), & \zeta_n^m \text{ odd} \end{cases} \tag{B.1}$$

When calculating the RMS wavefront error (WFE), it is convenient to use the RMS weight coefficients [4] of the polynomials where:

$$\mathrm{WFE}_{\mathrm{RMS}} = \sqrt{\sum_{j=1}^{N} (\zeta_j)^2 \, w_j^2} \tag{B.2}$$

where N is the number of Zernike coefficients calculated and the weight coefficients, w_j, follow the pattern listed in Table B.1 for the sequential counter j.

Table B.1: Definition of first 49 Zernike polynomials [36]

j	n	m	ω	Polynomial
0	0	0	1	1
1	1	1	4	$\rho\, cos(\theta)$
2	1	1	4	$\rho\, sin(\theta)$
3	1	0	3	$2\rho^2 - 1$
4	2	2	6	$\rho^2 cos(2\theta)$
5	2	2	6	$\rho^2 sin(2\theta)$
6	2	1	8	$(3\rho^3 - 2\rho)cos(\theta)$
7	2	1	8	$(3\rho^3 - 2\rho)sin(\theta)$
8	2	0	5	$6\rho^4 - 6\rho^2 + 1$
9	3	3	8	$\rho^3 cos(3\theta)$
10	3	3	8	$\rho^3 sin(3\theta)$
11	3	2	10	$(4\rho^4 - 3\rho^2)cos(2\theta)$
12	3	2	10	$(4\rho^4 - 3\rho^2)sin(2\theta)$
13	3	1	12	$(10\rho^5 - 12\rho^3 + 3\rho)cos(\theta)$
14	3	1	12	$(10\rho^5 - 12\rho^3 + 3\rho)sin(\theta)$
15	3	0	7	$20\rho^6 - 30\rho^4 + 12\rho^2 - 1$
16	4	4	10	$\rho^4 cos(4\theta)$
17	4	4	10	$\rho^4 sin(4\theta)$
18	4	3	12	$(5\rho^5 - 4\rho^3)cos(3\theta)$
19	4	3	12	$(5\rho^5 - 4\rho^3)sin(3\theta)$
20	4	2	14	$(15\rho^6 - 20\rho^4 + 6\rho^2)cos(2\theta)$
21	4	2	14	$(15\rho^6 - 20\rho^4 + 6\rho^2)sin(2\theta)$
22	4	1	16	$(35\rho^7 - 60\rho^5 + 30\rho^3 - 4\rho)cos(\theta)$
23	4	1	16	$(35\rho^7 - 60\rho^5 + 30\rho^3 - 4\rho)sin(\theta)$
24	4	0	9	$70\rho^8 - 140\rho^6 + 90\rho^4 - 20\rho^2 + 1$
25	5	5	12	$\rho^5 cos(5\theta)$
26	5	5	12	$\rho^5 sin(5\theta)$
27	5	4	14	$(6\rho^6 - 5\rho^4)cos(4\theta)$
28	5	4	14	$(6\rho^6 - 5\rho^4)sin(4\theta)$
29	5	3	16	$(21\rho^7 - 30\rho^5 + 10\rho^3)cos(3\theta)$
30	5	3	16	$(21\rho^7 - 30\rho^5 + 10\rho^3)sin(3\theta)$
31	5	2	18	$(56\rho^8 - 105\rho^6 + 60\rho^4 - 10\rho^2)cos(2\theta)$
32	5	2	18	$(56\rho^8 - 105\rho^6 + 60\rho^4 - 10\rho^2)sin(2\theta)$
33	5	1	20	$(126\rho^9 - 280\rho^7 + 210\rho^5 - 60\rho^3 + 5\rho)cos(\theta)$
34	5	1	20	$(126\rho^9 - 280\rho^7 + 210\rho^5 - 60\rho^3 + 5\rho)sin(\theta)$
35	5	0	11	$252\rho^{10} - 630\rho^8 + 560\rho^6 - 210\rho^4 + 30\rho^2 - 1$
36	6	6	14	$\rho^6 cos(6\theta)$
37	6	6	14	$\rho^6 sin(6\theta)$
38	6	5	16	$(7\rho^7 - 6\rho^5)cos(5\theta)$
39	6	5	16	$(7\rho^7 - 6\rho^5)sin(5\theta)$
40	6	4	18	$(28\rho^8 - 42\rho^6 + 15\rho^4)cos(4\theta)$
41	6	4	18	$(28\rho^8 - 42\rho^6 + 15\rho^4)sin(4\theta)$
42	6	3	20	$(84\rho^9 - 168\rho^7 + 105\rho^5 - 20\rho^3)cos(3\theta)$
43	6	3	20	$(84\rho^9 - 168\rho^7 + 105\rho^5 - 20\rho^3)sin(3\theta)$
44	6	2	22	$(210\rho^{10} - 504\rho^8 + 420\rho^6 - 140\rho^4 + 15\rho^2)cos(2\theta)$
45	6	2	22	$(210\rho^{10} - 504\rho^8 + 420\rho^6 - 140\rho^4 + 15\rho^2)sin(2\theta)$
46	6	1	24	$(462\rho^{11} - 1260\rho^9 + 1260\rho^7 - 560\rho^5 + 105\rho^3 - 6\rho)cos(\theta)$
47	6	1	24	$(462\rho^{11} - 1260\rho^9 + 1260\rho^7 - 560\rho^5 + 105\rho^3 - 6\rho)sin(\theta)$
48	6	0	13	$924\rho^{12} - 2772\rho^{10} + 3150\rho^8 - 1680\rho^6 + 420\rho^4 - 42\rho^2 + 1$

Appendix C

Optimization Script

```
% Thomas Gray
% May 2008
% master_structure.m
% This script implements a constant step-size gradient descent approach to
% optimize the structural design of a mirror (or segment).

% NOTES:
% 1. The 'design_vector' array stores parameters of the optimization for
% various design parameters.  Values for 'initial' override those specified
% in the PARAMETERS file.
% 2. This script saves optimization results within same directory to
% TRADEDATAn.mat and ZDATAn.mat (where 'n' is the number of rib rings).
% The directory must be clear of such files if the optimization routine is
% not a continuation of a previous run.
% 3. The gradient descent algorithm can be called over a larger set of
% design variables by adding such parameters where indicated throughout
% the script.
% 4. The search algorithm is a simplified gradient descent.  Careful
% consideration must be made so that the optimal design is not in a local
% minimum.

% Child scripts - This list briefly descibes, by primary function, the major
% scripts called by master_structure.
% PARAMETERS.m: Defines user-specified mirror parameters.
% PARAMETERSderived.m: Calculates dependent mirror parameters.
% mirror_trade.m: Generates and analyzes mirror FEM.  Computes dimpling
%       error metric and calls apply_static.m.
%    apply_static.m: Computes print-through error metric.

clear all;
%  call PARAMETERS file, loads user-specified mirror parameters
PARAMETERS;

% design parameters:
names = { 'Facesheet mass fraction';...   % range [0,1]
          'N_rings';...                   % no. of conc. rib rings
          'Primary rib AR';...            % aspect ratio (h/t)
          'Cathedral rib AR';...          % aspect ratio (h/t)
```

```
          'Cathedral mass fraction'};     % range [0,1]
          %-------------------------------------------------
          % add names for additional variables here
          %-------------------------------------------------

if strcmp(rib_limit,'thickness')
  names(3) = {'Primary rib thickness'};
end

% initialize 'design_vector' which stores trade space optimization data
% each row stores data for the corresponding parameters above
% each column is labeled as follows
% min: minimum limit of each design variable
% max: maximum limit of each design variable
% step: fixed step size for each variable in gradient descent algorithm
% initial: initial value of each variable for gradient descent search
% indicator: indicates if parameter is varied during optimization
%   value of '1' indicates ith variable is varied by chosen step size
%   value of '0' indicates ith variable held to initial value
if strcmp(rib_limit,'aspect_ratio')
  %                   min     max     step    initial indicator
  design_vector = [ 0.4     0.9     0.2     0.25    1; ...
                    2       5       1       2       0;...
                    10      120     20      25      0; ...
                    0.1     16      1       8       0; ...
                    0.00    0.95    0.02    0.06    1];...
                    %-------------------------------------------------
                    % add rows for additional variables here
                    %-------------------------------------------------
elseif strcmp(rib_limit,'thickness')
  %                   min     max     step    initial indicator
  design_vector = [ 0.05    0.95    0.04    0.8     1; ...
                    2       5       1       2       0; ...
                    0.001   0.003   1e-5    0.001   0; ...
                    0.1     16      1       8       0; ...
                    0       0.2     0.04    0.04    1];
                    %-------------------------------------------------
                    % add rows for additional variables here
                    %-------------------------------------------------
end

nvar = size(design_vector,1);
% 'trade_vector' stores 'indicator' column of design_vector
trade_vector = design_vector(:,5);
design_vector = design_vector(:,1:4);

% initialize design parameters
% facesheet mass fraction
MirrorInputs.percntmassplate = design_vector(1,4);
% N_rings (number of concentric rings in rib structure)
MirrorInputs.n_rings_iso     = design_vector(2,4);
% rib aspect ratio (AR) or thickness (t_ribs)
if strcmp(rib_limit,'aspect_ratio')
  MirrorInputs.AR            = design_vector(3,4);
elseif strcmp(rib_limit,'thickness')
  MirrorInputs.t_ribs        = design_vector(3,4);
end
% cathedral aspect ratio
MirrorInputs.AR_cath         = design_vector(4,4);
```

```
% cathedral mass fraction
MirrorInputs.percntmasscath   = design_vector(5,4);
%--------------------------------------------------------------------------
% initialize additional variables here
%--------------------------------------------------------------------------

% check feasibility of parameters
% check for negative rib mass fraction
rib_mass_frac = 1-design_vector(1,4)-design_vector(5,4);
if rib_mass_frac ≤ 0
  MirrorInputs.percntmasscath = 1 - design_vector(1,4);
end
%--------------------------------------------------------------------------
% check feasibility of additional variables here
%--------------------------------------------------------------------------

% load data from stored arrays or initialize if necessary
% TRADEDATA: stores history of each design and objective function value
% ZDATA: stores history of z-displacement vectors of each design
n_ring = MirrorInputs.n_rings_iso;
if exist(strcat('TRADEDATA',num2str(n_ring),'.mat'))
  load(strcat('TRADEDATA',num2str(n_ring),'.mat'))
  load(strcat('ZDATA',num2str(n_ring),'.mat'))

  % check for existence of design in history
  % x1(j,i) = 1 if ith parameter (initial) matches that of jth design
  % 'ismember_near(x,y,tol)': same as 'ismember' but is
  % satisfied within +/- tol to avoid rounding errors
  x1 = [];
  for ii = 1:nvar
    x1(:,ii) = ismember_near(TRADEDATA(:,ii),design_vector(ii,4),1e-7);
  end

else
  % intialize history arrays if initial design does not exist
  TRADEDATA = [];
  ZDATA = [];
  x1 = 0;
end

if max(sum(x1')) == nvar
  % design has already been considered
  [c,I] = max(sum(x1'));
  % initialize current objective function value
  current_metric = TRADEDATA(I(1),end);
else
  % design has not been considered
  disp('Generating mirror with parameters:')
  for ii = 1:nvar
    disp(strcat(names(ii),'  > ',num2str(design_vector(ii,4))))
  end

  % compute derived mirror parameters
  PARAMETERSderived;
  % 'mirror_trade' generates mirror FEM
  % and calculates total RSS surface residual ('metric')
  run mirror_trade

  % update TRADEDATA array with mirror parameters and surface residual
```

```
  TRADEDATA(end+1,:) = [design_vector(:,4)'  metric];

  % update ZDATA array with surface displacement vector
  if size(ZDATA,1) > 0
    if size(ZDATA,2) < length(z_after)
      % pad ZDATA with zeros
      ZDATA = [ZDATA zeros(size(ZDATA,1), length(z_after)-size(ZDATA,2))];
    elseif size(ZDATA,2) > length(z_after)
      % pad z_after with zeros
      ZDATA(end+1,:) = [z_after' zeros(1, size(ZDATA,2)-length(z_after))];
    else
      ZDATA(end+1,:) = z_after;
    end
  else
    ZDATA(end+1,:) = z_after;
  end

  % record current surface residual
  current_metric = TRADEDATA(end,end);

  % save data arrays
  save( strcat('TRADEDATA',num2str(n_ring)), 'TRADEDATA');
  save( strcat('ZDATA',num2str(n_ring)), 'ZDATA');
end

%==================================================================
% OPTIMIZATION ROUTINE
%==================================================================
% gradient search runs until (possibly constrained) local optimum is found
found_opt = 0;
while found_opt == 0

  %================================================================
  % PERTURB DESIGN VECTOR
  %================================================================

  % 'metric_vec' stores surface residual of all designs in perturbation stage
  metric_vec = zeros(nvar,2);
  % record current design vector for reference
  current = design_vector(:,4);

  % loop through all design parameters
  for var = 1:nvar
    % reset 'initial' design vector
    design_vector(:,4) = current;
    % perturb each design parameter specified by 'trade_vector'
    if trade_vector(var) == 1
      for step = [-1:1]
        % set 'design_vector' to each perturbed +/- value
        design_vector(var,4) = current(var) + step*design_vector(var,3);

        % check for max/min violation
        % set metric to Inf if violated
        if design_vector(var,4) < design_vector(var,1)
          % at minimum boundary
          design_vector(var,4) = design_vector(var,1);
          metric_vec(var,1) = Inf;
        elseif design_vector(var,4) > design_vector(var,2)
          % at maximum boundary
```

```
      design_vector(var,4) = design_vector(var,2);
      metric_vec(var,2) = Inf;
    end

    % reload mirror parameters
    PARAMETERS;
    % update design parameters to current values
    MirrorInputs.percntmassplate = design_vector(1,4);
    MirrorInputs.n_rings_iso     = design_vector(2,4);
    if strcmp(rib_limit,'aspect_ratio')
      MirrorInputs.AR            = design_vector(3,4);
    elseif strcmp(rib_limit,'thickness')
      MirrorInputs.t_ribs        = design_vector(3,4);
    end
    MirrorInputs.AR_cath         = design_vector(4,4);
    MirrorInputs.percntmasscath  = design_vector(5,4);
    %---------------------------------------------------------------
    % update additional variables here
    %---------------------------------------------------------------

    % check feasibility
    % check for negative rib mass fractions
    % reset cathedral rib mass fraction if violated
    rib_mass_frac = 1-design_vector(1,4)-design_vector(5,4);
    if rib_mass_frac ≤ 0
      MirrorInputs.percntmasscath = 1 - design_vector(1,4);
    end
    %---------------------------------------------------------------
    % check feasibility of additional variables here
    %---------------------------------------------------------------

    % check for existence of design in history
    x1 = [];
    for ii = 1:nvar
      x1(:,ii) = ismember_near(TRADEDATA(:,ii),design_vector(ii,4),1e-7);
    end

    if max(sum(x1')) == nvar
      % design has already been considered
      [c,I] = max(sum(x1'));
      if ¬isinf(metric_vec(var,round((step+1)/2+1)))
        metric_vec(var,round((step+1)/2+1)) = TRADEDATA(I,end);
      end
    else
      % generate mirror if design is feasible
      if ¬isinf(metric_vec(var,round((step+1)/2+1)))
        disp('Generating mirror with parameters:')
        for ii = 1:nvar
          disp(strcat(names(ii),' > ',num2str(design_vector(ii,4))))
        end

        % compute derived mirror parameters
        PARAMETERSderived;
        % 'mirror_trade' generates mirror FEM
        % and calculates total RSS surface residual ('metric')
        run mirror_trade

        % update TRADEDATA array
        TRADEDATA(end+1,:) = [design_vector(1:nvar,4)' metric];
```

```
          % update ZDATA array
          if size(ZDATA,1) > 0
            if size(ZDATA,2) < length(z_after)
              % pad ZDATA with zeros if necessary
              ZDATA = [ZDATA ...
                       zeros(size(ZDATA,1),length(z_after)-size(ZDATA,2))];
            elseif size(ZDATA,2) > length(z_after)
              % pad z_after with zeros if necessary
              ZDATA(end+1,:) = [z_after' ...
                                zeros(1, size(ZDATA,2)-length(z_after))];
            else
              ZDATA(end+1,:) = z_after;
            end
          else
            ZDATA(end+1,:) = z_after;
          end

          % update metric_vec
          metric_vec(var,round((step+1)/2+1)) = metric;

          % save data arrays
          save( strcat('TRADEDATA',num2str(n_ring)), 'TRADEDATA');
          save( strcat('ZDATA',num2str(n_ring)), 'ZDATA');
        end
      end
    end
  else
    % design parameter not considered in optimization
    metric_vec(var,:) = [Inf, Inf];
  end
end

%====================================================================
% UPDATE DESIGN VECTOR
%====================================================================

% 'opt' indicates local optimality of ith parameter if opt(i)=1
opt = zeros(nvar,1);
% form 'next' vector of design parameters using downhill perturbations
for ii = 1:nvar
  % find the downhill direction
  [c,I] = min([metric_vec(ii,:) current_metric]);
  if I == 1
    next(ii) = current(ii) - design_vector(ii,3);
  elseif I == 2
    next(ii) = current(ii) + design_vector(ii,3);
  else
    % iith parameter is locally optimal
    next(ii) = current(ii);
    opt(ii) = 1;
  end
  % iith parameter is locally optimal
  if min(metric_vec(ii,:)) == current_metric
    next(ii) = current(ii);
    opt(ii) = 1;
  end
end
```

```
% local optimum found if all opt(ii)=1
if sum(opt) == nvar
  found_opt = 1;
  disp('Local optimum found for parameters:')
  for ii = 1:size(names,1)
    disp(strcat(names(ii),'  > ',num2str(current(ii))))
  end

  disp('Locally optimal surface residual:')
  disp(current_metric)
end

% verify metric improvement of 'next' set of parameters
% reload mirror parameters
PARAMETERS;
MirrorInputs.percntmassplate = next(1);
MirrorInputs.n_rings_iso     = next(2);
if strcmp(rib_limit,'aspect_ratio')
  MirrorInputs.AR              = next(3);
elseif strcmp(rib_limit,'thickness')
  MirrorInputs.t_ribs          = next(3);
end
MirrorInputs.AR_cath           = next(4);
MirrorInputs.percntmasscath  = next(5);
%----------------------------------------------------------------------------
% update additional variables here
%----------------------------------------------------------------------------

% check for non-negative primary rib mass fraction
rib_mass_frac = 1-next(1)-next(5);
if rib_mass_frac ≤ 0
  % reset cathedral mass fraction if violated
  MirrorInputs.percntmasscath = 1 - next(1);
end
%----------------------------------------------------------------------------
% check feasibility of additional variables here
%----------------------------------------------------------------------------

% check for existence of design in history
x1 = [];
for ii = 1:nvar
  x1(:,ii) = ismember_near(TRADEDATA(:,ii),next(ii),1e-7);
end

if max(sum(x1')) == 5
  % design has already been considered
  [c,I] = max(sum(x1'));
  metric = TRADEDATA(I(1), end);
else
  disp('Generating mirror with parameters:')
  for ii = 1:size(names,1)
    disp(strcat(names(ii),'  > ',num2str(next(ii))))
  end

  % compute derived parameters, generate mirror FEM,
  % and compute surface residual
  PARAMETERSderived;
  run mirror_trade

```

```
    % update TRADEDATA array
    TRADEDATA(end+1,:) = [next(1:nvar) metric];

    % update ZDATA array
    if size(ZDATA,1) > 0
      if size(ZDATA,2) < length(z_after)
        % pad ZDATA with zeros
        ZDATA = [ZDATA zeros(size(ZDATA,1), length(z_after)-size(ZDATA,2))];
      elseif size(ZDATA,2) > length(z_after)
        % pad z_after with zeros
        ZDATA(end+1,:) = [z_after' zeros(1, size(ZDATA,2)-length(z_after))];
      else
        ZDATA(end+1,:) = z_after;
      end
    else
      ZDATA(end+1,:) = z_after;
    end

    % save data arrays
    save( strcat('TRADEDATA',num2str(n_ring)), 'TRADEDATA');
    save( strcat('ZDATA',num2str(n_ring)), 'ZDATA');
  end

  % update 'current_metric' if 'next' is suboptimal
  if found_opt == 0
    if metric < current_metric
      % 'next' design is downhill
      % update design_vector with 'next' parameters
      current_metric = metric;
      design_vector(:,4) = next';
    else
      % 'next' design is uphill, update only most downhill parameter
      [c,I] = min(opt);

      % update along I(1) direction
      design_vector(:,4) = current;
      design_vector(I(1),4) = next(I(1));

      % update 'current_metric'
      current_metric = min(metric_vec(I(1),:));
    end
  end
end
```

Bibliography

[1] NASA JWST webpage. URL: http://www.jwst.nasa.gov.

[2] Xinetics, Inc. supplied data. Apr, 2007.

[3] *MD/Nastran Linear Static and Normal Modes Analysis - workbook*, June 1998.

[4] G. Z. Angeli and B. Gregory. Linear optical model for a large ground based telescope. In *Proceedings SPIE Int. Soc. Opt. Eng.*, volume 5178, pages 64–73, Jan 2004.

[5] P. Y. Bely, editor. *The Design and Construction of Large Optical Telescopes.* Springer, New York, 2003.

[6] D. Bertsimas and J. Tsitsiklis. *Introduction to Linear Optimization.* Athena Scientific, Belmont, MA, 1997.

[7] D. Bertsimas and J. Tsitsiklis. *Introduction to Probability.* Athena Scientific, Belmont, MA, 2002.

[8] C. Blaurock. *Disturbance-optics-controls-structures (DOCS) Technical report, Nightsky Systems, Inc., 2006.* URL: http://www.nightsky-systems.com/pdf/DOCS Intro.pdf.

[9] M. Cho, R. Richard, and D. Vukobratovich. Optimum mirror shapes and supports for light weight mirrors subjected to self weight. In *Proceedings SPIE*, volume 1167, 1989.

[10] L. Cohan. Integrated modeling to facilitate control architecture design for lightweight space telescopes. Master's thesis, Massachusetts Institute of Technology, June 2007.

[11] S. Crandall and N. Dahl, editors. *An Introduction to the Mechanics of Solids.* McGraw Hill, New York, 1959.

[12] L. Daniel. Introduction to numerical simulation (16.910) course notes, Sept. 2006.

[13] M. Ealey and J. Wellman. Fundamentals of deformable mirror design and analysis. In *Proceedings SPIE*, volume 1167, 1989.

[14] M. Ealey and J. Wellman. Ultralightweight silicon carbide mirror design. In *Proceedings SPIE*, volume 2857, 1996.

[15] M. Ealey and J. Wellman. Highly adaptive integrated meniscus primary mirrors. In *Proceedings SPIE*, volume 5166, 2004.

[16] R. Foy and F. Foy, editors. *Optics in Astrophysics.* NATO Science Series. Springer, 2005.

[17] V. Genberg and N. Cormany. Optimum design of lightweight mirrors. In *Proceedings SPIE*, volume 1998, pages 60–71, 1998.

[18] J. Hardy. *Adaptive Optics for Astronomical Telescopes.* Oxford University Press, New York, 1998.

[19] J. How. Principles of optimal control (16.323) course notes, Apr 2007.

[20] J. How, E. Anderson, D. Miller, and S. Hall. High bandwidth control for low area density deformable mirrors. In *Proceedings SPIE Aerospace Sensing Conference*, volume 1489, pages 148–162, Oct. 1991.

[21] B. H. I. Zarudi. Deformation and material removal rate in polishing silicon wafers. *Journal of Materials Processing Technology*, 140, 2003.

[22] C. Jilla. *A Multiobjective, Multidisciplinary Design Optimization Methodology for the Conceptual Design of Distributed Satellite Systems.* Phd thesis, Massachusetts Institute of Technology, June 2002.

[23] E. Jordan. Design and shape control of lightweight mirrors for dynamic performance and athermalization. Master's thesis, Massachusetts Institute of Technology, June 2007.

[24] R. Kapania, P. Mohan, and A. Jakubowski. Control of thermal deformations of spherical mirror segment. *Journal of Spacecraft and Rockets*, 35(2), March 1998.

[25] K. Kilroy. *Nastran Quick Reference Guide*, June 1997.

[26] W. Larson and J. Wertz, editors. *Space Mission Analysis and Design.* Microcosm Press, El Segundo, CA, 3rd edition, 2005.

[27] R. Masterson. Development and validation of empirical and analytical reaction wheel disturbance models. Master's thesis, Massachusetts Institute of Technology, June 1999.

[28] P. Mehta and P. Reid. A mathematical model for optical smoothing prediction of high-spatial frequency surface errors. In *Proceedings SPIE*, volume 3786, 1999.

[29] A. Oppenheim and R. Schafer. *Digital Signal Processing.* Prentice Hall, New Jersey, 1975.

[30] K.-S. Parka, J. H. Lee, and S.-K. Youn. Lightweight mirror design method using topology optimization. *Optical Engineering*, 44, May 2005.

[31] M. Shepherd, G. Peterson, R. Cobb, and A. Palazotto. Quasi-static optical control of in-plane actuated, deformable mirror: Experimental comparison with finite element analysis. *AIAA Structures, Structural Dynamics, and Materials Conference*, May 2006.

[32] J. Veran and D. Durand. Reduction of adaptive optics images. ASP Conference Series, 2000.

[33] Z. Wei and Y. Yi. Design of lightweight mirror based on genetic algorithm. In *Proceedings SPIE*, volume 6148, 2006.

[34] K. Willcox and O. de Weck. Design space exploration. Multidisciplinary system design optimization (MSDO) course notes, Feb 2004.

[35] S. Winters, J. Chung, and S. Velinsky. Modeling and control of a deformable mirror. *Journal of Dynamic Systems, Measurement, and Control*, 124, June 2002.

[36] J. C. Wyant. Zernike polynomials. Technical report. URL: http://www.optics.arizona.edu/jcwyant/Zernikes/ZernikePolynomials.htm.

[37] Y. Yong, J. Guang, and Y. Hong-bo. Design and analysis of large spaceborne light-weighted primary mirror and its support system. In *Proceedings SPIE*, volume 6721, 2007.